Technical University of Munich
TUM School of Engineering and Design

TUM

New high-order low-dissipation schemes for convection-dominated problems with shockwaves

Yue Li

Complete reprint of the dissertation approved by the TUM School of Engineering and Design

of the Technical University of Munich for the award of the

Doktorin der Ingenieurwissenschaften (Dr.-Ing.)

Chair: Prof. Dr. Dongsheng Wen

Examiners:

1.   Prof. Dr.-Ing. Nikolaus A. Adams
2.   Prof. Dr.-Ing. Bing Wang

The dissertation was submitted to the Technical University of Munich on 12 September 2023

and accepted by the TUM School of Engineering and Design on 12 February 2024.

Declaration of Authorship

I hereby declare that except where specific reference is made to the work of others, the contents of this dissertation are original and have not been submitted in whole or in part for consideration for any other degree or qualification in this, or any other university. This dissertation is my own work and contains nothing which is the outcome of work done in collaboration with others, except as specified in the text and Acknowledgements.

<div align="right">

Yue Li
July 5, 2023

</div>

谨以此文献给我的大家庭。

This work is dedicated to my big family.

Ueber allen Gipfeln
Ist Ruh',
In allen Wipfeln
Spürest Du
Kaum einen Hauch;
Die Vögelein schweigen im Walde.
Warte nur! Balde
Ruhest du auch.

—— Johann Wolfgang von Goethe

Abstract

This cumulative thesis presents several novel high-order low-dissipation numerical schemes with improved robustness and performance. More specifically, a new high-order framework which can flexibly adjust dissipation, a fast multi-resolution essentially non-oscillatory (FMENO) scheme and a neuron-based method for construct high-order schemes are proposed. These newly proposed methods provide the new insight and new technique to develop a high-order low-dissipation numerical schemes from three aspects, i.e. flexible framework to adjust dissipation, high efficiency and classical methods integrated with machine learning. The newly proposed methods in this thesis are demonstrated to improve the performance and robustness of high-order low-dissipation schemes and to deepen the understanding of numerical scheme reconstruction.

First, a framework to construct arbitrarily high-order low-dissipation shock-capturing schemes with flexible and controllable nonlinear dissipation for convection-dominated problems is proposed. Based on the construction of TENO-like candidate stencils with incremental width, each stencil is evaluated and indicated as smooth or nonsmooth by the ENO-like stencil selection procedure proposed in the targeted essentially non-oscillatory (TENO) scheme [Fu et al., Journal of Computational Physics 305 (2016): 333-359]. Rather than being discarded directly as with TENO schemes, the nonsmooth candidates are filtered by an extra nonlinear limiter, such as a monotonicity-preserving (MP) limiter or total variation diminishing (TVD) limiter. Compared with the standard TENO schemes, discarding completely the nonsmooth candidate stencils is avoid and their contributions are filtered by a nonlinear limiter. The filtered candidate stencil contributions are assembled to form the final reconstruction with their respective optimal linear weights. In addition, through deploying a wide range of limiters, such as TVD and MP, the new scheme achieves adaptive nonlinear dissipation property without deteriorating the ground resolution and properties of TENO.

Second, a new class of high-order fast multi-resolution essentially non-oscillatory schemes is proposed with an emphasis on both the performance and the computational efficiency. To capture the local flow with multi-resolution scales, a set of candidate stencils ranging from high- to low-order (from large to small stencil) is constructed in a hierarchical manner. The candidate stencils are evaluated by the regularity criterion introduced with MP limiter. If the reconstructed cell interface flux of a candidate stencil locates within the MP lower and upper bounds, it is regarded to be smooth. The multi-resolution stencil selection strategy will choose these smooth stencils with better spectral property or higher-order accuracy. If all the candidate stencils are judged to be nonsmooth, the targeted stencil which violates the MP criterion the least is deployed as the final reconstruction instead. With this new framework, the desirable high-order accuracy is restored in the smooth regions while the sharp shock-capturing capability is achieved by selecting the targeted stencil satisfying the MP criterion most. Compared to the standard weighted/targeted essentially non-oscillatory (W/TENO) schemes, the computational efficiency is dramatically enhanced by avoiding the expensive evaluations of the classical smoothness

indicators.

Last, the potential of integrating machine learning to design high-order low-dissipation ENO schemes is investigated. Inspired by the work that weights of candidate stencils containing discontinuities can be fully removed and this binary selection can be predicted by a well-trained neural network, we introduce a deep artificial neural network (ANN) that can detect locations of discontinuity and build a six-point ENO-type scheme (NENO6) based on this detection. Compared with classical TENO6-opt scheme, neural based indicator rather than classical smoothness indicator is deployed to suggest an ENO-like sub-stencil selection. This new framework makes use of the complex underlying input-output mapping in neural network rather than empiricism smoothness indicators. We demonstrate that our model can generate highly accurate predictions of several one dimensional benchmark examples in different hyperbolic equations. Compared with other neural based schemes, NENO6 shows an improved universality, assured boundedness and accuracy.

Acknowledgements

First of all, I would like to thank Prof. Nikolaus A. Adams for providing me the opportunity to pursue my Ph.D study in TUM, Germany. I am very grateful to Prof. Adams who has advised this work thoroughly, inspired me with new ideas, and encouraged me when I was frustrated. Through weekly group meeting, I fully benefit from his great visions of research, passions in science, and kindness to help young researcher to build a big picture for their future.

Special thanks to Dr. Lin Fu, who helps me not only in providing feedback, revising papers, and inspiring suggestions for academic study, but also encouraging me to have a firm and optimistic attitude towards life. I have been fortunate to have the opportunity to work with you and this work will not be accomplished without your help. I sincerely hope your academic career will develop as you expected.

My gratitude extends to Dr. Christian Stemmer for his guidance in improving writing skills and help in scientific work. It is a pleasure to work with friendly and talented people in the Chair of Aerodynamics and Fluid Mechanics, thanks for interesting discussions during my PhD study: Dr. Stefan Adami, Dr. Song Chen, Ludger Pähler, Hoppe Nils, Winter Josef, Vladimir Bogdanov, Antonio Di Giovanni, Kaller Thomas, Kaiser Jakob, Xiuxiu Lyv, Yujie Zhu, Zhe Ji and Dr. Jong-Seob Han. Particularly, I would like to thank staff members in our chair, Angela Grygier, Hua Liu, and Li Su, for their kind services.

I would like to thank China Scholarship Council for the support during the four-year program. It gives me a great opportunity to see, to learn and to become innovative.

Finally, and most importantly, my deepest gratitude goes to my parents and my whole family. This dissertation would not be possible without your love and support.

Contents

Nomenclature

ANN	Artifical Neural Network
CFD	Computational Fluid Dynamics
CFL	Courant-Friedrich-Lewy
CNN	Convolutional Neural Network
ENO	Essentially Non-Oscillatory
EOS	Equation Of State
FVM	Finite Volume Method
LES	Large-Eddy Simulation
LSTM	Long Short-Term Memory
ML	Machine Learning
MLP	Multi-Layer Perception
MUSCL	Monotonic Upwind Scheme for Conservation Laws
NN	Neural Network
ODEs	Ordinary Differential Equations
PDEs	Partial Differential Equations
PINN	Physical-Informed Neural Network
RANS	Reynolds-averaged Navier–Stokes
RHS	Right Hand Side
RK	Runge-Kutta
RKDG	Runge-Kutta Discontinuous Galerkin
RNN	Recurrent Neural Network
SSP	Strong Stability-Preserving
TENO	Targeted Essentially Non-Oscillatory
TVD	Total Variation Diminishing
WENO	Weighted Essentially Non-Oscillatory
WENO-CU6	sixth-order Weighted Essentially Non-Oscillatory scheme

Chapter 1

Introduction

In this thesis, my research in the Chair of Aerodynamics and Fluid Mechanics (AER) at the Technical University of Munich (TUM) is presented. During this period, I have been working on numerical schemes for hyperbolic problems and machine learning for fluid mechanics.

The thesis is arranged as following: In Chapter 1, the motivation and the scientific background of the thesis is first introduced. In addition, the objectives of the entire thesis are summarized. In Chapter 2, several numerical methods are introduced: The governing equation and its discretization methodology are first reviewed. Popular high-order schemes and their key ideas are discussed. In Chapter 3, the training strategy of a classical neural network and recent progress in machine learning for fluid mechanics are discussed. Chapter 4 summarizes the main accomplishments achieved in the current thesis. Concluding remarks and future work are presented in Chapter 5. A discussion with respect to the state of the art is concluded in Chapter6. The e-prints of the publication accomplished in the current thesis are attached in Appendix A.

1.1   Motivation

Compressible fluid dynamics problems which are relevant to high-speed aircraft, jet engines, rocket motors, high-speed entry into a planetary atmosphere are often encountered in the areas of science and engineering. A typical shock-wave boundary layer interaction is shown in Fig. 1.1. These fluid dynamics problems include a wide range of spatial and temporal scales and shock waves. However, low numerical dissipation is expected to resolve small-scale vortex accurately while adequate numerical dissipation is expected to capture the shock stably. To analyze these complex multi-scale and non-linear fluid phenomena, advanced numerical schemes which can solve the contradictory requests are proposed.

1.2   An overview of numerical schemes in solving multiscale flows

From a mathematical point of view, the governing equations behind many engineering problems are time-dependent, nonlinear hyperbolic PDEs. Two challenges in solving the hyperbolic equations are low numerical dissipation with small error and non-physical oscillations in the presence of shocks. In this section, we will briefly review some of most important techniques in solving the hyperbolic problems.

Low-order schemes, i.e. first- or second-order schemes, are traditionally used to keep monotonicity in capturing shock waves. First-order upwind Godunov scheme [2] and first-order central Lax method [3] are two typical examples. However, the
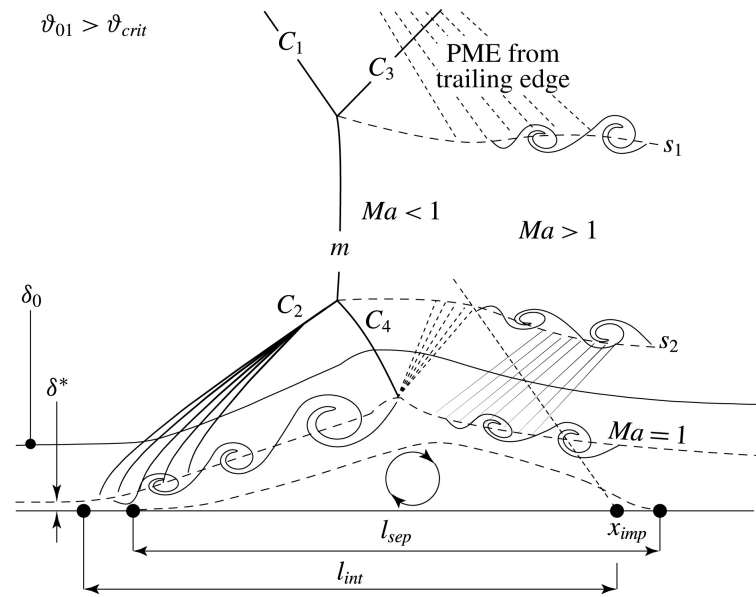
FIGURE 1.1: Sketch of an irregular shock-wave / boundary-layer interaction (SWBLI) [1].

upwind scheme causes strong dispersion and dissipation problems. To cope with the intrinsic inaccuracy in low-order schemes, high-order schemes are developed. Even these linear high-order schemes are capable to gain solutions with high accuracy in smooth regions, they fail to suppress the spurious oscillations in the vicinity of the discontinuities. In order to resolve the vast range of spatial and temporal length-scales in complex fluid, the reconstruction of high-order and low-dissipation schemes gains more and more attentions.

One proposed method to keep the high accuracy of higher-order as well as to guarantee the monotone feature is the use of nonlinear limiters. According to the variations of the limiters, total variation diminishing (TVD) scheme [4], superbee limiter [5], van Leer limiter [6], Woodward limiter, Minmod limiter [7] and the monotone upstream-centered scheme for conservation laws (MUSCL) schemes[8] are the popular choices. Another popular methods [9] is the high-order low-dissipation schemes based on the essentially non-oscillatory (ENO) scheme [9][10][11][12][13][14][15]. Harten et al. [12] first propose the high-order ENO scheme, which selects the smoothest stencil from a set of predefined candidate stencils to avoid the Gibbs phenomenon near discontinuities. Following the idea of identifying stencils with different smoothness, WENO scheme and its variants [9][14][15]are proposed based on the smoothness indicators such that the desired accuracy order is restored in smooth regions and the ENO property is preserved near discontinuities. Although the performance of the high-order low-dissipation schemes is enhanced by the aforementioned schemes, limitations in terms of following aspects, e.g. control dissipation with the flexible framework, high time efficiency especially in a very high-order scheme construction and the robustness of the schemes are still unsolved.

1.3   Machine learning in fluid mechanics

In the past few years, we have experienced a renewed blossoming of ML applications in fluid mechanics. Much of this interest is attributed to the remarkable performance of deep learning architectures, which hierarchically extract informative features from data. As ML methods can provide an input-output mapping with a high degree of complexity, it is potential to be combined into classical fluid mechanics to assist the reduced-order modeling [16][17][18], shape optimization [19], turbulence closure modeling [20][21][22], numerical schemes construction [23][24][25] [26][27]and flow control [28][29].

Artificial neural networks (ANNs) are the most common structures, and they are composed of layers of neurons, where input layer neurons receive an input data, processes it through an activation function, and produces an output. Nonlinear optimization methods, such as backpropagation [30], are used to identify the network weights to minimize the error between the prediction and labeled training data. In particular, we consider a specific feed-forward network architecture known as multilayer perceptions (MLPs).

When the activation functions are expressed in terms of convolutional kernels, convolutional neural networks (CNN) whose processing elements only have directly interactions within a finite local neighborhood [31] are developed. The CNNs achieve a great success in image and pattern recognition. Another type of neural network worth to be mentioned is recurrent neural networks (RNNs). The architecture of RNN takes into account the inherent order of the data. However, their effectiveness has been hindered by diminishing or exploding gradients that emerge during their training. The renewed interest in RNNs is largely attributed to the development of the long short-term memory (LSTM) [32] algorithms that deploy cell states and gating mechanisms to store and forget information about past inputs, thus alleviating the problems with gradients and the transmission of long-term information from which standard RNNs suffer. An extended architecture called the multidimensional LSTM network [33] was proposed to efficiently handle high dimensional spatiotemporal data.

1.4   Outline

The introduction highlights the progress of the high-order numerical schemes capable of capturing shock-wave and resolve small-scale fluid structures and the application of machine learning in investigating numerical toolbox in fluid mechanics. The objectives of the present work is to develop a high-order low-dissipation numerical schemes from new insight and new technique.

First, a framework to construct arbitrarily high-order low-dissipation shock-capturing schemes with flexible and controllable nonlinear dissipation for convection-dominated problems is proposed. Through the adaptation of nonlinear limiters, nonlinear dissipation in the newly proposed framework can be controlled separately without affecting the performance in smooth regions. The work is presented in paper I which is available in Appendix A.1.

Second, a new class of high-order fast multi-resolution essentially non-oscillatory (FMRENO) schemes is proposed with an emphasis on both the performance and

the computational efficiency. Compared to the standard weighted/targeted essentially non-oscillatory (W/TENO) schemes, the computational efficiency is dramatically enhanced by avoiding the expensive evaluations of the classical smoothness indicators. The work is presented in paper II which is available in Appendix A.2.

Third, we investigate the potential of integrating machine learning to design high-order low-dissipation ENO schemes. We introduce an ANN that can detect locations of discontinuity and build a six-point ENO-type scheme based on a set of smooth and discontinuous training data. The work is presented in paper III which is available in Appendix A.3.

Chapter 2

Numerical methods

In this chapter, the concepts of numerical methods relevant to governing equation and high order schemes are reviewed.

2.1 Hyperbolic Conservation Laws

In this section, the classical high-order low-dissipation finite-difference schemes and Runge-Kutta method for solving hyperbolic conservation laws, i.e. Navier-Stokes equations, are introduced.

2.1.1 Navier-Stokes equation

For compressible fluid dynamics, the conservative forms governing equations, i.e. Navier-Stokes equations, can be written as

$$\frac{\partial \rho}{\partial t} + \nabla \cdot (\rho \mathbf{u}) = 0, \tag{2.1}$$

$$\frac{\partial (\rho \mathbf{u})}{\partial t} + \nabla \cdot (\rho \mathbf{u}\mathbf{u} + p\delta) = \nabla \cdot \tau, \tag{2.2}$$

$$\frac{\partial E}{\partial t} + \nabla \cdot (\mathbf{u}(E + p)) = \nabla \cdot (\mathbf{u} \cdot \tau - \dot{q}), \tag{2.3}$$

where ρ, $\mathbf{u}$ and E are density, velocity and total energy respectively.

In the energy equation, $\dot{q}$ is the heat flux, which can be calculated by Fourier's law. τ is the viscous stress tensor, which can be defined as a function of dynamic viscosity μ and the strain rate sensor $\mathbf{S}$ in the Stokes' hypothesis for a Newtonian fluid

$$\tau = 2\mu \mathbf{S} - \frac{2}{3}\mu(\nabla \cdot \mathbf{u})\delta, \tag{2.4}$$

$$\mathbf{S} = \frac{1}{2}(\nabla \mathbf{u} + (\nabla \mathbf{u})^T). \tag{2.5}$$

2.1.2 Numerical discretization

Normally, the heat transfer term and viscous term are treated as source terms separately. In this manner, the governing equations reduce to the Euler equations, which can be further written as a system of hyperbolic conservation laws

$$\frac{\partial \mathbf{Q}}{\partial t} + \nabla \cdot \mathbf{F}(\mathbf{Q}) = \mathbf{0}, \tag{2.6}$$

where $\mathbf{Q} = [\rho, \rho\mathbf{u}, E]^T$ denotes the conservative variables and $\mathbf{F} = [\rho\mathbf{u}, \rho\mathbf{u}\mathbf{u} + p\delta, \mathbf{u}(E + p)]^T$ denotes the flux tensor.

As the conservative variables are coupled through the ideal-gas equations-of-state (EOS) $p = (\gamma - 1)\rho e$, the discretizations of the convective terms in Eq. (2.6) are typically applied in the characteristic space to avoid numerical oscillations induced by the interaction between different characteristic waves [14].

Following the equation

$$\mathbf{q}_m = \mathbf{R}_{i+1/2}^{-1}\mathbf{Q}_m, \ \mathbf{f}_m = \mathbf{R}_{i+1/2}^{-1}\mathbf{F}_m, \tag{2.7}$$

all conservative variables and fluxes are projected to the characteristic space, where m denotes for each characteristic field and the left eigenvector matrix $\mathbf{R}_{i+1/2}^{-1}$ can be computed by the Roe average [34] at the cell interface.

In finite difference algorithm, the projected fluxes $\mathbf{f}_m$ are split by flux splitting methods as

$$f^{(l)\pm} = \frac{1}{2}(f^{(l)} \pm \lambda_{\max}^{(l)} q^{(l)}), \tag{2.8}$$

where $f^{(l)}$ and $q^{(l)}$ denote the lth element of the vector $\mathbf{f}$ and $\mathbf{q}$, the sign "+" and "−" denote the positive and negative flux parts, such that $\frac{df^{(l)+}}{dq} \geq 0$ and $\frac{df^{(l)-}}{dq} \leq 0$.

Normally, the eigenvalue of $\lambda_{\max}^{(l)}$ denotes the lth eigenvalue of $\partial\mathbf{F}/\partial\mathbf{Q}$ at cell i and can be defined according to the splitting methods, such as the Rusanov splitting method [35] and the Roe splitting method [34].

For instance, the mostly employed flux-splitting method, i.e. Rusanov splitting method [35] is defined as

$$\lambda_{\max}^{(l)} = \max\left|\lambda_m^{(l)}\right|, \ m = 1, \ldots, n, \tag{2.9}$$

over the entire computational flowfield.

The numerical flux at the cell interface $i + 1/2$ for each characteristic field is reconstructed following

$$\hat{f}_{i+1/2} = \hat{f}_{i+1/2}^+ + \hat{f}_{i+1/2}^-. \tag{2.10}$$

At last, through a reverse projection of the flux in characteristic field, the flux in the physical space can be obtained as

$$\hat{\mathbf{F}}_{i+1/2} = \mathbf{R}_{i+1/2}\hat{\mathbf{f}}_{i+1/2}. \tag{2.11}$$

2.1.3 Runge-Kutta method

After discretizing the spatial derivatives of hyperbolic conservation laws Eq. (2.6), a set of ODEs is formed as

$$\frac{d\mathbf{Q}}{dt} = L(\mathbf{Q}). \tag{2.12}$$

To advance the conservative variables in time, explicit high-order Runge-Kutta method [36] are popular for resolving the transient flows. To ensure the strong stability property for spatial discretization, Gottlieb et al. [36] proposed a class of strong stability-preserving high-order time discretizations for semi-discrete method-of-lines approximations of partial differential equations.

An optimal third-order SSP Runge-kutta method [36] is given as

$$
\begin{aligned}
\mathbf{Q}^{(1)} &= \mathbf{Q}^n + \Delta t L(\mathbf{Q}^n) \\
\mathbf{Q}^{(2)} &= \tfrac{3}{4}\mathbf{Q}^n + \tfrac{1}{4}\mathbf{Q}^{(1)} + \tfrac{1}{4}\Delta t L(\mathbf{Q}^{(1)}) \quad , \\
\mathbf{Q}^{n+1} &= \tfrac{1}{3}\mathbf{Q}^n + \tfrac{2}{3}\mathbf{Q}^{(2)} + \tfrac{2}{3}\Delta t L(\mathbf{Q}^{(2)})
\end{aligned}
\tag{2.13}
$$

for a sufficiently small timestep constrained by a CFL condition [37].

2.2 High-order schemes

In this section, the high-order low-dissipation shock-capturing schemes which are essential numerical methods to reconstruct the flux **F** at the cell interface $i + 1/2$ in compressible fluid problems are elaborated. Firstly, the general method to construct high-order linear scheme is introduced. To solve the flow field which may involve discontinuities and broadband flow scales with high-order schemes, many concepts are introduced.

Several classical schemes, such as ENO, WENO and its variants and TENO schemes are reviewed here [10][11][12][13][14][15]. The aims of these methods are to concentrate on restoring high-order accuracy in smooth regions with low numerical dissipation while preserving monotonicity near discontinuities[38][9][39].

2.2.1 General method to construct the high-order scheme

To facilitate the presentation of (W/T)ENO schemes, we first consider the general method to construct a polynominal-based high-order scheme for the one-dimensional scalar hyperbolic conservation law

$$
\frac{\partial q}{\partial t} + \frac{\partial}{\partial x} f(q) = 0,
\tag{2.14}
$$

where q and f denote the conservative variable and the flux function respectively. The characteristic signal speed is assumed to be positive $\frac{\partial f(q)}{\partial u} > 0$. The developed schemes can be extended to systems of conservation laws and multi-dimensional problems in a straightforward manner.

For a uniform Cartesian mesh with cell centers $x_i = i\Delta x$ and cell interfaces $x_{i+1/2} = x_i + \frac{\Delta x}{2}$, the spatial discretization results in a set of ordinary differential equations

$$
\frac{dq_i(t)}{dt} = -\frac{\partial f}{\partial x}\Big|_{x=x_i}, \ i = 0, \cdots, n,
\tag{2.15}
$$

where q_i is a numerical approximation to the point value $q(x_i, t)$. The semi-discretization with Eq. (2.15) can be further discretized by a conservative finite-difference scheme as

$$
\frac{dq_i}{dt} = -\frac{1}{\Delta x}(h_{i+1/2} - h_{i-1/2}),
\tag{2.16}
$$

where the primitive function $h(x)$ is implicitly defined by

$$
f(x) = \frac{1}{\Delta x} \int_{x-\Delta x/2}^{x+\Delta x/2} h(\xi)d\xi,
\tag{2.17}
$$

and $h_{i\pm1/2} = h(x_i \pm \frac{\Delta x}{2})$.

A high-order approximation of $h(x)$ at the cell interface has to be reconstructed from the cell-averaged values of $f(x)$ at the cell centers. Eq. (2.16) can be written as

$$\frac{dq_i}{dt} \approx -\frac{1}{\Delta x}(\widehat{f}_{i+1/2} - \widehat{f}_{i-1/2}), \tag{2.18}$$

where $\hat{f}_{i\pm1/2}$ denotes the approximate numerical fluxes and can be computed from predefined stencils.

For a K-point stencil, a K-th order polynomial interpolation of function $h(x)$ can be assumed as

$$h(x) \approx \hat{f}(x) = \sum_{l=0}^{K-1} a_l x^l. \tag{2.19}$$

After substituting Eq. (2.21) into Eq. (2.17) and evaluating the integral functions at the stencil nodes, the coefficients a_l are determined by solving the resulting system of linear algebraic equations.

It is worth to notice that a K-th order linear scheme is achieved following this interpolation. However, the linear high-order scheme can not avoid the Gibbs phenomenon near discontinuities. Different computational strategies are applied to construct nonlinear high-order schemes with the predefined candidate stencils, the typical numerical schemes and their advantages are elaborated in the following.

2.2.2 WENO schemes

Among all the schemes, the idea of ENO is first proposed by Harten et al. [12], which selects the smoothest stencil from a set of predefined candidate stencils to avoid the Gibbs phenomenon near discontinuities. Based on the development of the high-order ENO-family schemes, Liu et al. [13] propose the WENO scheme and find that based on the same set of candidate sub-stencils in [12], the optimal global high-order accuracy can be achieved if a convex combination of all candidate sub-stencils is applied.

For the classical WENO schemes, the global Kth-order scheme is constructed based on a set of low order candidate stencils ranging from S_0 to $S_{\frac{K+1}{2}-1}$. All candidate stencils feature the same width as r. To obtain $K = (2r-1)$th-order approximation for $\widehat{f}_{i+1/2}$, $(r-1)$-degree polynomial distribution is supposed on each candidate stencil as where $\hat{f}_{i+1/2}$ is assembled by a convex combination of r candidate stencil fluxes

$$\widehat{f}_{i+1/2} = \sum_{k=0}^{r-1} \omega_k \widehat{f}_{k,i+1/2}, \tag{2.20}$$

where ω_k denotes the nonlinear weight for each candidate flux, and $\widehat{f}_{k,i+1/2}$ denotes the r-th order approximate numerical flux similar to the definition in Eq. (2.21). And each $(r-1)$-degree candidate stencil can be assumed as

$$h(x) \approx \hat{f}_k(x) = \sum_{l=0}^{r-1} a_{l,k} x^l. \tag{2.21}$$

After substituting Eq. (2.21) into Eq. (2.17) and evaluating the integral functions at the stencil nodes, the coefficients $a_{l,k}$ are determined like a_l in the general construction of high-order scheme.

For the five-point WENO schemes, the sketch of three candidate stencils S_0, S_1, S_2 is shown in Fig. 2.1.
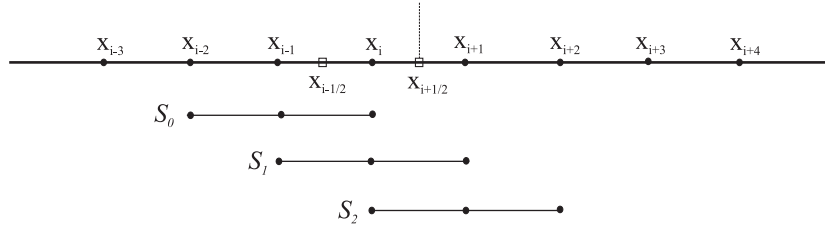
FIGURE 2.1: Sketch of the candidate stencils for the five-point reconstruction WENO scheme.

And based on the pre-defined candidate stencils, the expressions for the three candidate fluxes are

$$
\begin{aligned}
\hat{f}_{0,i+1/2} &= \tfrac{1}{6}(2f_{i-2} - 7f_{i-1} + 11f_i), \\
\hat{f}_{1,i+1/2} &= \tfrac{1}{6}(-f_{i-1} + 5f_i + 2f_{i+1}), \\
\hat{f}_{2,i+1/2} &= \tfrac{1}{6}(2f_i + 5f_{i+1} - f_{i+2}).
\end{aligned}
\tag{2.22}
$$

For suppressing Gibbs oscillations in the presence of discontinuities, the weight of candidate stencils which are crossed by discontinuities will be reduced. And the weight of each candidate stencil can be decided by the smoothness indicator

$$
\alpha_k = \frac{d_k}{(\beta_{k,r} + \varepsilon)^2}, \quad k = 0, \cdots, r - 1,
\tag{2.23}
$$

where d_k denotes the optimal weight that generates a $(2r - 1)$-th order scheme on the full stencil with $(2r - 1)$ points and $\varepsilon = 10^{-6}$ is introduced to prevent the zero denominator. For the five-point WENO schemes, the overall fifth-order accuracy is achieved with $d_0 = 0.1, d_1 = 0.6, d_2 = 0.3$.

Following Jiang and Shu [14], $\beta_{k,r}$ can be given as

$$
\beta_{k,r} = \sum_{j=1}^{r-1} \Delta x^{2j-1} \int_{x_{i-1/2}}^{x_{i+1/2}} \left(\frac{d^j}{dx^j} \hat{f}_k(x) \right)^2 dx
\tag{2.24}
$$

based on the L_2 norm of the derivatives of the reconstructed candidate polynomials.

In smooth regions, the convex combination of r stencils produces $(2r - 1)$-th order approximate numerical flux evaluated at the cell face. If one certain stencil contains discontinuity, the weight of the corresponding stencil deteriorates to be nearly zero and the scheme degenerates to r-th order reconstruction. For the five-point WENO schemes, explicit expressions for the smoothness indicators are

$$
\begin{aligned}
\beta_0 &= \tfrac{1}{4}(f_{i-2} - 4f_{i-1} + 3f_i)^2 + \tfrac{13}{12}(f_{i-2} - 2f_{i-1} + f_i)^2, \\
\beta_1 &= \tfrac{1}{4}(f_{i-1} - f_{i+1})^2 + \tfrac{13}{12}(f_{i-1} - 2f_i + f_{i+1})^2, \\
\beta_2 &= \tfrac{1}{4}(3f_i - 4f_{i+1} + f_{i+2})^2 + \tfrac{13}{12}(f_i - 2f_{i+1} + f_{i+2})^2.
\end{aligned}
\tag{2.25}
$$

Subsequently, based on the smoothness indicators of candidate stencils, the nonlinear weights w_k are given as

$$
\omega_k = \frac{\alpha_k}{\sum_{l=0}^{r-1} \alpha_k}, \quad k = 0, \cdots, r - 1,
\tag{2.26}
$$

such that the contributions from the candidate stencils crossed by discontinuities reduce and the high-order accuracy is restored asymptotically in smooth regions.

2.2.3   Variants of WENO schemes

Practical implementations reveal that the classical WENO scheme [14] is rather dissipative to solve turbulence flows. Based on this observations, several variants of WENO schemes are proposed to further improve the performance.

The performance of the WENO schemes can be further enhanced by improving the nonlinear weighting strategy, e.g., the WENO-M [40] and WENO-Z [41][42] schemes avoid the order degeneration near critical points through correcting the nonlinear weights to be closer to the optimal linear ones. Henrick et al. [43] suggest that restoring the optimal accuracy order near critical points can resolve the over-dissipation issue. Necessary and sufficient conditions have been derived and a mapping strategy based on classical WENO, referred as WENO-M, has been developed accordingly. However, as investigated by Borges et al. [44], the improvements demonstrated by WENO-M [43] over classical WENO result from larger weights of nonsmooth candidate stencils and less nonlinear adaptive dissipation, rather than from higher accuracy near critical points. To further decrease the nonlinear adaptive dissipation, a new smoothness indicator has been proposed by Borges et al. [44], which introduces a global high-order undivided difference into the weighting strategy of the classical WENO scheme. As an alternative approach [45], the nonlinear dissipation adaptation can be controlled by comparing the ratio between the largest and the smallest calculated smoothness indicator. By introducing a problem-dependent threshold, adaptation is eliminated when the ratio is below the threshold. The aforementioned WENO-like schemes reduce the dissipation of the classical WENO significantly. In [46], a new smoothness indicator that can decrease the measured smoothness variances on different candidate stencils in smooth regions is proposed. The resulting new schemes based on the same candidate stencils of classical WENO schemes are called WENO-S. However, they are still too dissipative for resolving turbulence-like high-wavenumber fluctuations.

Besides decreasing the nonlinear adaptive dissipation, optimizing the background counterpart linear scheme of WENO can improve the overall dissipation property too. The WENO-SYMOO [47] and WENO-CU6 [48] schemes optimize the background scheme as a central scheme by introducing the contribution of the downwind stencil. However, anti-dissipation is inherently built in for a certain wavenumber range, which may be problematic for critical applications. Therefore, in terms of designing low-dissipation shock capturing schemes, the strategy of choosing a stable linear scheme with upwind-biased candidate stencils as a background scheme and then optimizing the nonlinear dissipation adaptation to its limit is preferable. Other recent work following this direction includes the development of WENO-Z+ scheme [49].

To show the enhencement of the WENO variants following different methods, WENO-CU6 [48] scheme, WENO-Z [41][42] scheme and WENO-S [46] are reviewed as following.

1) The WENO-CU6 scheme

To reduce the numerical dissipation in classical WENO schemes, a WENO-CU6 [48] which adapts between central and upwind schemes is proposed. The WENO-CU6 is designed based on four candidate stencils shown in Fig. 2.2. A pure downwind stencil is considered to reduce the dissipation.

Like WENO-family schemes [14][41], a global sixth order approximate numerical flux can be computed from a convex combination of four candidate stencils with the
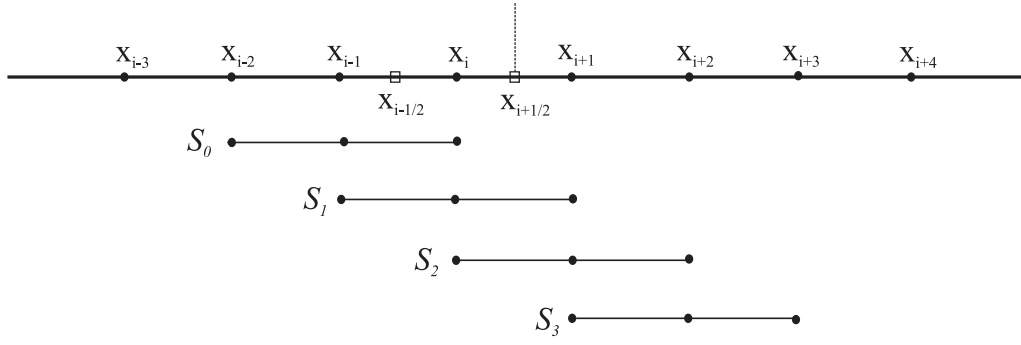
FIGURE 2.2: Sketch of the candidate stencils for the six-point reconstruction WENO scheme.

same width $r = 3$ as

$$\widehat{f}_{i+1/2} = \sum_{k=0}^{3} \omega_k^{CU6} \widehat{f}_{k,i+1/2}. \tag{2.27}$$

In order to obtain a less dissipative scheme, and following Borges et al. [41], the nonlinear weights are computed by

$$\omega_k^{CU6} = \frac{\alpha_k^{CU6}}{\sum_{k=0}^{3} \alpha_k^{CU6}}, \tag{2.28}$$

$$\alpha_k^{CU6} = d_k \left(C + \frac{\tau_6}{\beta_k + \varepsilon} \right)^q , \ k = 0, 1, 2, 3 \tag{2.29}$$

where the constant $q = 1$, $C = 20$ and $\varepsilon = 10^{-40}$ is introduced to prevent the zero denominator. The large value of C can reduce the nonlinear adaptation in smooth regions and consequently the numerical dissipation is decreased. Here, the optimal weights are $d_0 = \frac{1}{20}$, $d_1 = \frac{9}{20}$, $d_2 = \frac{9}{20}$, $d_3 = \frac{1}{20}$ such that the combined scheme recovers to the standard sixth-order central scheme in smooth regions.

To avoid a pure downwind reconstruction, which is numerically unstable, the smoothness indicator β_3 is derived from the full six-point stencil as

$$
\begin{aligned}
\beta_3 = \beta_6 \ = \ & \frac{1}{120960} \big[271779 f_{i-2}^2 + f_{i-2}(-2380800 f_{i-1} + 4086352 f_i - 3462252 f_{i+1} \\
& + \ 1458762 f_{i+2} - 245620 f_{i+3}) + f_{i-1}(5653317 f_{i-1} - 20427884 f_i \\
& + \ 17905032 f_{i+1} - 7727988 f_{i+2} + 1325006 f_{i+3}) \\
& + \ f_i(19510972 f_i - 35817664 f_{i+1} + 15929912 f_{i+2} - 2792660 f_{i+3}) \\
& + \ f_{i+1}(17195652 f_{i+1} - 15880404 f_{i+2} + 2863984 f_{i+3}) \\
& + \ f_{i+2}(3824847 f_{i+2} - 1429976 f_{i+3}) + 139633 f_{i+3}^2 \big] .
\end{aligned}
\tag{2.30}
$$

The new global reference smoothness indicator τ_6 is defined as

$$\tau_6 = |\beta_6 - \frac{1}{6}(\beta_0 + \beta_2 + 4\beta_1)|. \tag{2.31}$$

2) The WENO-Z scheme

With the WENO-family schemes [14][41], a global $(K = 2r - 1)$-th order approximate numerical flux can be computed from a convex combination of r candidate

stencils with the same width r as

$$\widehat{f}_{i+1/2} = \sum_{k=0}^{r-1} \omega_k^Z \widehat{f}_{k,i+1/2}, \tag{2.32}$$

where ω_k^Z denotes the nonlinear weight for each candidate flux, and $\hat{f}_{k,i+1/2}$ denotes the r-th order approximate numerical flux similar to the definition in Eq. (2.21).

For WENO-Z schemes [41], the nonlinear weight ω_k^Z of each stencil is renormalized from the optimal linear weight d_k as

$$\omega_k^Z = \frac{\alpha_k^Z}{\sum_{k=0}^{r-1} \alpha_k^Z}, \tag{2.33}$$

$$\text{and } \alpha_k^Z = \frac{d_k}{\beta_k^Z}. \tag{2.34}$$

In the WENO-Z scheme, the optimal linear weight d_k is the corresponding coefficient for each candidate stencil to achieve maximum accuracy order of the background linear scheme.

Following [50], the calculation of the β_k^Z function is obtained by

$$\frac{1}{\beta_k^Z} = \left(1 + (\frac{\tau_{2r-1}}{\beta_{k,r} + \epsilon})^p\right), \text{ and } p = 1 \text{ or } 2, \tag{2.35}$$

and $\epsilon = 10^{-40}$ is introduced to prevent the zero denominator.

Following Jiang and Shu [14], the smoothness indicator $\beta_{k,r}$ for the k-th candidate stencil can be given as

$$\beta_{k,r} = \sum_{j=1}^{r-1} \Delta x^{2j-1} \int_{x_{i-1/2}}^{x_{i+1/2}} \left(\frac{d^j}{dx^j} \hat{f}_k(x)\right)^2 dx \tag{2.36}$$

based on the L_2 norm of the derivatives of the reconstructed candidate polynomials.

The global high-order smoothness indicator τ_{2r-1} is defined with a linear combination of existing low-order smoothness indicators $\beta_{0,r}, ..., \beta_{r-1,r}$ as:

$$\tau_{2r-1} = \begin{cases} |\beta_{0,r} - \beta_{r-1,r}|, & \text{if } \mod(r,2) = 1, \\ |\beta_{0,r} - \beta_{1,r} - \beta_{r-2,r} + \beta_{r-1,r}|, & \text{if } \mod(r,2) = 0. \end{cases} \tag{2.37}$$

3) The WENO-S scheme

In [46], a new smoothness indicator that can decrease the measured smoothness variances on different candidate stencils in smooth regions is proposed. The resulting new schemes based on the same candidate stencils of classical WENO schemes are called WENO-S. For WENO-S schemes [46], the nonlinear weight ω_k^S of each stencil is renormalized from the optimal linear weight d_k as

$$\omega_k^S = \frac{\alpha_k^S}{\sum_{k=0}^{r-1} \alpha_k^S}, \text{ and } \alpha_k^S = d_k \left(1 + (\frac{\tau^S}{\beta_k^S + \epsilon})\right), \tag{2.38}$$

$$\text{and } \alpha_k^S = d_k \left(1 + (\frac{\tau^S}{\beta_k^S + \epsilon})\right), \tag{2.39}$$

where $\varepsilon = 10^{-40}$ is introduced to prevent the zero denominator and the formula of the β_k^S function is given by

$$
\begin{aligned}
\beta_k^S = {} & (f_{i+k-3} - f_{i+k-2} - f_{i+k-1} + f_{i+k})^2 + \\
& |(-f_{i+k-3} - f_{i+k-2} + f_{i+k-1} + f_{i+k})(-f_{i+k-3} + 3f_{i+k-2} - 3f_{i+k-1} + f_{i+k})|.
\end{aligned} \tag{2.40}
$$

For the seven-point WENO-S scheme, the global smoothness indicator τ^S can be written as

$$
\begin{aligned}
\tau^S = {} & (-f_{i-3} + 4f_{i-2} - 5f_{i-1} + 5f_{i+1} - 4f_{i+2} + f_{i+3})^2 + \\
& + |(f_{i-3} - 2f_{i-2} - f_{i-1} + 4f_i - f_{i+1} - 2f_{i+2} + f_{i+3}) \\
& (f_{i-3} - 6f_{i-2} + 15f_{i-1} - 20f_i + 15f_{i+1} - 6f_{i+2} + f_{i+3})|.
\end{aligned} \tag{2.41}
$$

2.2.4 TENO schemes

To further reduce the dissipation by suppressing nonlinear adaptation and achieve stable shock-capturing capability, a family of high-order TENO schemes has been proposed by Fu et al. [15][51][52][53]. Unlike the WENO-like smooth convex combination, TENO either adopts a candidate stencil with its optimal weight for the final reconstruction or discards it completely when crossed by a genuine discontinuity. This procedure is ensured by a cut-off parameter C_T, which identifies the smooth and nonsmooth regions. In smooth regions, nonlinear adaptation is unnecessary and the numerical dissipation is reduced to that of the linear background scheme. In nonsmooth regions, nonlinear dissipation is introduced to suppress oscillations and to achieve the robust shock-capturing capability. This strategy successfully reduces the numerical dissipation so that turbulence-like high-wavenumber fluctuations can be sustained [51]. The construction of TENO schemes is reviewed as following.
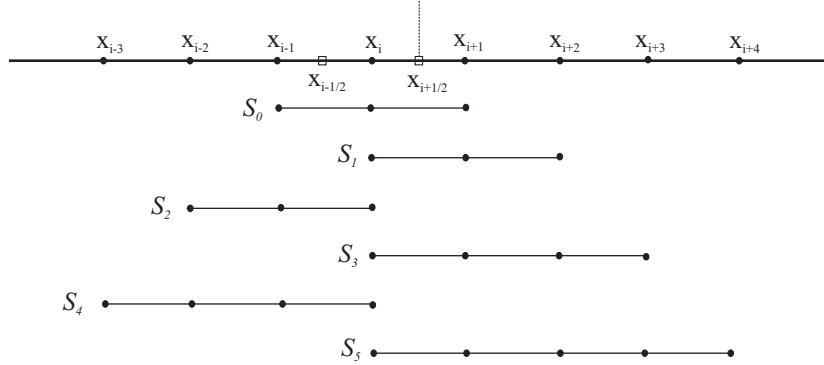

FIGURE 2.3: Candidate stencils with incremental width towards high-order TENO reconstructions. All candidate stencils possess at least one upwind point.

1) Candidate stencils

Different from WENO schemes, arbitrarily high-order TENO schemes are constructed from a set of candidate stencils with incremental width [15], as shown in Fig. 2.3.

The sequence of stencil width *r* varying versus the global accuracy order *K* is as

$$\{r_k\} = \begin{cases} \underbrace{\{3,3,3,4,\cdots,\dfrac{K+2}{2}\}}_{0,\cdots,K-3}, & \text{if } \mod(K,2) = 0, \\ \underbrace{\{3,3,3,4,\cdots,\dfrac{K+1}{2}\}}_{0,\cdots,K-3}, & \text{if } \mod(K,2) = 1. \end{cases} \tag{2.42}$$

2) Scale-separation procedure

To effectively isolate discontinuities from smooth regions, smoothness indicators with strong scale-separation capability are given as [15]

$$\gamma_k = \left(C + \frac{\tau_K}{\beta_{k,r} + \varepsilon} \right)^q, k = 0, \cdots, K - 3, \tag{2.43}$$

where $\varepsilon = 10^{-40}$ is introduced to prevent the zero denominator and τ_K is relevent to β_K, which measures the global smoothness on the *K*-point full stencil, .

In a six-point TENO scheme, the parameters $C = 1$ and $q = 6$ are adopted for strong scale separation. Similarly to WENO schemes, $\beta_{k,r}$ can be defined as Eq. (2.36) [14].

A sixth-order τ_6, which allows for good numerical stability with a reasonably large CFL number, can be constructed as [51]

$$\tau_6 = \left| \beta_6 - \frac{1}{6}(\beta_{1,3} + \beta_{2,3} + 4\beta_{0,3}) \right| = O(\Delta x^6). \tag{2.44}$$

3) ENO-like stencil selection

For TENO schemes [15], the measured smoothness indicators are first normalized as

$$\chi_k = \frac{\gamma_k}{\sum_{k=0}^{K-3} \gamma_k}, \tag{2.45}$$

and subsequently filtered by a sharp cut-off function

$$\delta_k = \begin{cases} 0, & \text{if } \chi_k < C_T, \\ 1, & \text{otherwise.} \end{cases} \tag{2.46}$$

In sixth-order TENO scheme, the parameter $C_T = 10^{-6}$ can be determined by spectral analysis [15]. In such a way, all candidate stencils are then identified to be either sufficiently smooth or nonsmooth with a discontinuity crossing the stencil.

4) Nonlinear adaptation strategy for C_T

Although the above weighting strategy is sufficient to separate smooth regions from discontinuities, overestimated numerical dissipation is generated for turbulence-like high-wavenumber fluctuations since they are treated in a similar manner as discontinuities. Previous research reveals that the low-order undivided difference is more sensitive to distinguish high-wavenumber fluctuations from genuine discontinuities than high-order undivided differences [52][54][55].

Motivated by Ren et al.[56], the local smoothness of flow field can be indicated by

$$
\begin{cases}
m = 1 - \min(1, \frac{\eta_{i+1/2}}{C_r}), \\
\eta_{i+1/2} = \min(\eta_{i-1}, \eta_i, \eta_{i+1}, \eta_{i+2}),
\end{cases}
\tag{2.47}
$$

where

$$
\eta_i = \frac{|2\Delta f_{i+1/2}\Delta f_{i-1/2}| + \epsilon}{(\Delta f_{i+1/2})^2 + (\Delta f_{i-1/2})^2 + \epsilon},
\tag{2.48}
$$

$$
\Delta f_{i+1/2} = f_{i+1} - f_i, \epsilon = \frac{0.9C_r}{1 - 0.9C_r}\xi^2,
\tag{2.49}
$$

and the parameters $\xi = 10^{-3}$, $C_r = 0.23$ are used for the eight-point TENO schemes [54]. Low numerical dissipation for turbulence-like high-wavenumber fluctuations is achieved by adjusting the cut-off parameter C_T as

$$
\begin{cases}
g(m) = (1 - m)^4(1 + 4m), \\
\beta = \alpha_1 - \alpha_2(1 - g(m)), \\
C_T = 10^{-[\beta]},
\end{cases}
\tag{2.50}
$$

where $[\beta]$ denotes the maximum integer which is not larger than β. $g(m)$ is a smoothing kernel based mapping function, and $\alpha_1 = 10.5$, $\alpha_2 = 3.5$ are set for the eight-point TENO schemes [54].

5) The final high-order reconstruction

In order to remove contributions from candidate stencils containing discontinuities, optimal weights d_k subjected to the cut-off δ_k are re-normalized as

$$
\omega_k = \frac{d_k \delta_k}{\sum_{k=0}^{K-3} d_k \delta_k}.
\tag{2.51}
$$

The Kth-order reconstructed numerical flux evaluated at cell face $i + \frac{1}{2}$ is assembled as

$$
\hat{f}_{i+1/2}^K = \sum_{k=0}^{K-3} w_k \hat{f}_{k,i+1/2}.
\tag{2.52}
$$

In such a way, candidate stencils are identified to be either sufficiently smooth or nonsmooth sharply, and the contributions from candidate stencils containing discontinuities are fully removed. For smooth regions, all candidate stencils are judged to be smooth with $\delta_k = 1$ and thus the high-order accuracy of the background optimal linear scheme is restored exactly without degeneration.

Note that, in order to get better resolution for small-scale flow structures, the optimal weights d_k can be further optimized such that better spectral properties are obtained on the full stencil [51].

2.3 Classical limiters

Extensive numerical experiments demonstrate that nonlinear limiters are able to eliminate the numerical oscillations by limiting the flux's gradient variation. These limiters are utilized to improve the stability of the high-order scheme and will influence the performance of the resulting high-order schemes. For instance, TVD

nonlinear limiters [57] enforce the TVD property by introducing the slope function $\phi(r)$ to limit the gradient variation. Several second- and third-order TVD schemes with different slope functions have been developed, e.g. with the Minmod limiter, the Superbee limiter and the Van Leer limiter [7][5][4]. Classical nonlinear limiters, such as Van Albada limiter [58] and MP limiter [59] are reviewed in the following.

1) Van Albada limiter

Here, we take the Van Albada limiter as an example to exemplify the construction of nonlinear limiter. Following [58], the slope function of a Van Albada limiter $\phi(r)_{\text{VA}}$ is defined as

$$\phi_{\text{VA}}(r) = \frac{2r}{r^2 + 1}, \tag{2.53}$$

and the slope ratio r based on a three-cell stencil centered at i is

$$r = \delta^+ / \delta^-, \tag{2.54}$$

where $\delta^- = f_i - f_{i-1}, \delta^+ = f_{i+1} - f_i$.

2) MP limiter

Suresh and Huynh [59] propose a monotonicity-preserving method to bound the high-order reconstructed data at cell interface by distinguishing smooth local extrema from genuine discontinuity. The resulting monotonicity-preserving schemes allow for the local extremum to develop in the evaluation of cell interface data and is robust for shock-dominated flows.

The minmod function with two arguments is

$$\text{minmod}(x, y) = \frac{1}{2}[\text{sgn}(x) + \text{sgn}(y)] \min(|x|, |y|), \tag{2.55}$$

and the minmod function with four arguments is

$$\begin{aligned}
\text{minmod}(a, b, c, d) = \frac{1}{8}&[\text{sgn}(a) + \text{sgn}(b)] \\
&|[\text{sgn}(a) + \text{sgn}(c)][\text{sgn}(a) + \text{sgn}(d)]| \min(|a|, |b|, |c|, |d|).
\end{aligned} \tag{2.56}$$

The median function is

$$\text{median}(x, y, z) = x + \text{minmod}(y - x, z - x). \tag{2.57}$$

While the curvature at the cell center i can be approximated by

$$d_i = f_{i+1} - 2f_i + f_{i-1}, \tag{2.58}$$

the curvature measurement at the cell interface $i + 1/2$ can be defined as

$$d_{i+1/2}^{\text{M4}} = \text{minmod}(4d_i - d_{i+1}, 4d_{i+1} - d_i, d_i, d_{i+1}). \tag{2.59}$$

This definition is more restrictive since the room for local extrema to develop is reduced when the ratio d_{i+1}/d_i is smaller than $1/4$ or larger than 4.

In order to define the minimum and maximum bounds of data at the interface $x_{i+1/2}$, the left-side upper limiter is given as

$$f^{\mathrm{UL}}_{i+1/2} = f_i + \alpha(f_i - f_{i-1}), \tag{2.60}$$

where the choice of α in principle should satisfy the condition that $\mathrm{CFL} \leq 1/(1+\alpha)$ for stability.

The median value of the solution at $x_{i+1/2}$ is given by

$$f^{\mathrm{MD}}_{i+1/2} = \frac{1}{2}(f_i + f_{i+1}) - \frac{1}{2}d^{\mathrm{MD}}_{i+1/2}. \tag{2.61}$$

The left-side value allowing for a large curvature in the solution at $x_{i+1/2}$ can be given by

$$f^{\mathrm{LC}}_{i+1/2} = f_i + \frac{1}{2}(f_i - f_{i-1}) + \frac{\beta}{3}d^{\mathrm{LC}}_{i-1/2}, \tag{2.62}$$

where it is recommended to set $\beta = 4$.

Following [59] and [60], $d^{\mathrm{MD}}_{i+1/2} = d^{\mathrm{LC}}_{i+1/2} = d^{\mathrm{M4}}_{i+1/2}$ is adopted.

In numerical validations, the parameters in MP limiters will influence the inherent dissipation of the MP limiter.

The bounds are given by

$$\begin{aligned} f^{\mathrm{L,min}}_{i+1/2} &= \max[\min(f_i, f_{i+1}, f^{\mathrm{MD}}_{i+1/2}), \min(f_i, f^{\mathrm{UL}}_{i+1/2}, f^{\mathrm{LC}}_{i+1/2})], \\ f^{\mathrm{L,max}}_{i+1/2} &= \min[\max(f_i, f_{i+1}, f^{\mathrm{MD}}_{i+1/2}), \max(f_i, f^{\mathrm{UL}}_{i+1/2}, f^{\mathrm{LC}}_{i+1/2})], \end{aligned} \tag{2.63}$$

and the monotonicity preserving value for data at the interface $x_{i+1/2}$ is obtained by limiting the predicted value from other reconstructions as

$$f^{\mathrm{MP}}_{i+1/2} = \mathrm{median}(\widehat{f}_{i+1/2}, f^{\mathrm{L,min}}_{i+1/2}, f^{\mathrm{L,max}}_{i+1/2}). \tag{2.64}$$

Chapter 3

Machine learning in fluid mechanics

In this chapter, technical details and challenges regarding the machine learning methods are presented. The fundamental concepts of machine learning and its applications, i.e. neural network algorithm and the applications in fluid mechanics are discussed.

3.1 Machine learning

Fluid mechanics can be analyzed by experiments and numerical simulations. The numerical simulations are conducted by governing equations, which describes the complex nonlinear dynamics of multi-scale fluid structures. Machine learning which serves as an input-output mapping with a high degree of complexity, provides a new technique to analyze the underlying fluid mechanics behind the fluid field [61][62].

Indeed, with the enhanced capability of machine learning to elaborate the non-linear mapping between input and output information, machine learning is now rapidly introduced into different fields of fluid mechanics. As proposed in references, machine learning is applied as a powerful tool to solve the challenges such as reduced-order modeling [16][17][18], shape optimization [19], turbulence closure modeling [20][21][22], numerical scheme construction [23] [24][25][26][27]and flow control [28] [29]. In the following, we will discuss the classical machine learning algorithm and the application of machine learning combined with classical fluid mechanics.

3.1.1 Classical neural network algorithm

Neural networks are the most well-known supervised machine learning algorithms. The basic architectures of neural networks are layers of neurons, where signals are processed from input to output through intermediate layers and activation functions [18]. According to the statements of Hornik et al. [63], any function may be approximated by a sufficiently large and deep network. Moreover, the theory of backpropagation proposed by Rumelhart et al. enables the development of neural networks with increasing depths [30]. With the development of different activation function, various advanced deep neural networks are developed.

Multi-layer perceptions

The simplest ANN are based on a large collection of connected simple units. Typically, neurons are connected in layers, and signals travel from the first (input), to the

last (output) layer. We are interested in approximating a function of the form

$$F = \mathbb{R}^{d_{in}} \rightarrow \mathbb{R}^{d_{out}}, \tag{3.1}$$

using artificial neural networks. In particular, we consider a specific feed-forward network architecture known as MLP.

This multivariate compound function is comprised of successive linear and non-linear operations, which maps the input vector X through a number of intermediate steps to the output vector Y. The first layer is called the input layer, and has the purpose of providing an input signal to the network. The last layer is the output layer, while all the intermediate layers are known as the hidden layers. In machine learning terminology, an MLP of depth K corresponds to a network with an input layer, $K - 1$ hidden layers and an output layer. Each layer of the network receives the output from the previous layer and performs an affine linear transformation of the form

$$x^{l-1} \rightarrow y^l = w^l x^{l-1} + b^l, \tag{3.2}$$

where w^l and b^l are respectively the weights and biases with the layer l.

The output y^l is then acted component-wise by a nonlinear activation function to form the input for the next layer. The activation function prevents the neural network from collapsing into a single affine linear transformation. Several choices for activation functions have been proposed. Here, we take the ELU activation function as an example [64],

$$f_{act}^{\mathrm{ELU}}(y^l) = \begin{cases} \exp(y^l - 1), & \text{if } y < 0, \\ y^l, & \text{if } y \geq 0, \end{cases} \tag{3.3}$$

as it can avoid the vanishing gradient problem and yields smooth output. In order to train a network with the aforementioned architecture, i.e. to refine the weights and biases, the output Y for a given input is computed in a forward pass by applying Eq. (3.2) and Eq. (3.3) along the network graph. The error between the prediction Y and the true output $\hat{Y}$ is measured by a cost function $C(Y, \hat{Y})$. Through a backpropagation, which computes the partial derivatives of the cost function, an optimization of ANN is conducted to reduce the cost function.

3.2 Applications of machine learning in computational fluid mechanics

In fluid flows, solving the governing equations is the dominant method to precisely quantify the underlying physical mechanisms. However, due to the multiple spatiotemporal scales property of fluid structures, scale-resolving simulations, especially for high Reynolds number problems, are beyond our current computational resources. Considerable effort has been taken to cope with the contradiction between obtaining accuracy and efficiency.

In the scope of traditional numerical tools, high-order scheme, empirical turbulence model and super-resolution are proposed. The recent blossoming machine learning algorithms provide a new insight to estimate the nonlinear associations between inputs and outputs. In the following, applications of machine learning in terms of solving ordinary and partial differential equations, turbulence closures and numerical schemes are elaborated.

3.2.1 Solving ordinary and partial differential equations

One typical method in solving differential equations using neural network is mapping the solution of a linear system of equations to the architecture of a Hopfield neural network. For instance, Dissanayake and Phanthien [65] proposed that partial different equations can be solved by neural-network based method. They transformed the PDE problems to an unconstrained minimization problem by a "universal approximator" constructed by a neural network and point collocation. Other similar applications can be found in [66] [67][68].

Unlike the approaches mentioned above, Lagaris et al. [69] proposed a general method which can be applied to both ODEs and PDEs. A trial solution of the differential equation is written as a sum of representatives of the initial/boundary conditions and a feed-forward neural network part. Through satisfying the construction of the initial/boundary conditions, the network is trained to satisfy the differential equation.

Inspired by that the physical conservation laws and prior physical knowledge can be encoded into the networks [69], Raissi et al. [70] introduce PINN that enables the synergistic combination of mathematical models and data. Unlike any classical numerical method for solving partial differential equations, PINN predicted spatio-temporal solution along with the locations of the initial and boundary training data without any sort of discretization of the spatio-temporal domain. In [71], the applications of PINN in different types of PDEs, including integro-differential equations [72], fractional PDEs [73][74], and stochastic PDEs[75] [76][77] are presented.

However, in order to model problems with long-time integration of PDEs, PINN has to train model with large size of data. The traditional parallel approaches used in fluid mechanics [78][79], which decomposes the long-time domain and solves the subdomains in parallel, may have difficulties in treating PDE problems when only partial observations on the boundary/initial conditions are available. To solve this problem, Meng et al. [80] propose an improved physics-informed neural network to split one long-time problem into many independent short-time problems supervised by an inexpensive coarse-grained solver.

3.2.2 Turbulence closures

The use of ML to develop turbulence closures is an active area of research as the scales in turbulent flows is exceedingly costly to resolve all scales in simulation even now. To avoid the unacceptable computational cost in a full scale turbulent flow modeling, common approaches, such as RANS and LES, are attempt to truncate small scales and model their effects on the large scales with a closure model. However, these models may require careful tuning to match data from fully resolved simulations or experiments.

Compared with classical models restricted to limited flow variables, the neural-based model provides an improved prediction accuracy with higher-dimensional information extracted [81][82]. In [83], a deep neural networks are proposed to learn a model for the Reynolds stress anisotropy tensor with high-fidelity simulation data. Sarghini et al. [84] propose to a NN-hybrid LES modeling, where all relevant variables involved in the calculation of the original SGS model are introduced as input vector. NNs are performed as a self organize black-box to give out a more computationally efficient NN representation. In addition, to advance the time efficiency, Beck et al. [85] employs artificial NNs to predict the turbulence source term from coarsely resolved quantities.

3.2.3   Numerical schemes

Recently, data-driven methods have been incorporated into the development of shock-capturing schemes, e.g. to function as a discontinuity indicator [25][26][27], and to enhance the performance of specific discretization schemes [23][24]. An example of shock detection based on neural network is presented in [27], where the network is trained to serve as a troubled-cell indicator for constructing the hybrid shock-capturing scheme in the framework of RKDG method, and an extension to two-dimensional problems is given in [86]. Morgan et al. [87] propose a MLP based shock detector for a high-order finite-element method. However, as these efforts are taken to train a data-driven indicator to control the switch between different schemes, the performance of the resultant shock-capturing schemes is more dominated by the component linear and nonlinear schemes rather than the indicator itself.

As an alternative approach, Stevens and Colonius [24] and Bar-Sinai et al. [23] deploy neural networks to modify the coefficients of the baseline polynomial-based high-order schemes directly. It is shown in [24] that the resulting WENO-NN scheme fails to preserve the optimal accuracy order and generates strong overshoots for under-resolved simulations. Moreover, the data-driven scheme coefficients for the spatial derivatives may be equation-specific and thus lack the generality and robustness [23]. More recently, Jung and Kwon [88] show that the neural network can function as a numerical model, as long as the training database is well normalized and constructed.

Chapter 4

Summaries of publications

In this chapter, the selected publications and main accomplishments during my PhD stage are briefly summarized. The current state-of-the-arts regarding each topic are presented too in each section. For more details, I refer to Appendix A.1, A.2 and A.3 respectively.

4.1 A low-dissipation shock-capturing framework with flexible nonlinear dissipation control

Y. Li, L. Fu and N.A. Adams (2021)

4.1.1 State of the art

Low-dissipation shock-capturing schemes are necessary in order to solve compressible fluid problems involving discontinuities. Harten et al. [12] first propose the high-order ENO scheme, which selects the smoothest stencil from a set of predefined candidate stencils to avoid the Gibbs phenomenon near discontinuities. To achieve the optimal global high-order accuracy on the same set of candidate stencils, Liu et al. [13] propose the WENO scheme which applies a nonlinear convex combination of all candidate stencils. The optimal linear weights are modulated based on the smoothness indicators such that the desired accuracy order is restored in smooth regions and the ENO property is preserved near discontinuities. However, the excessive numerical dissipation of WENO (as main typical flaw of WENO-family schemes) need to be further enhanced to solve turbulence shockwave interaction flow. In state of the art, a family of high-order TENO schemes has been proposed by Fu et al. [15][51][52][53] to further reduce the dissipation by suppressing nonlinear adaptation and achieve stable shock-capturing capability. Unlike the WENO-like smooth convex combination, TENO either adopts a candidate stencil with its optimal weight for the final reconstruction or discards it completely when crossed by a genuine discontinuity. This procedure is ensured by a cut-off parameter C_T, which identifies the smooth and nonsmooth regions. In smooth regions, nonlinear adaptation is unnecessary and the numerical dissipation is reduced to that of the linear background scheme. In nonsmooth regions, nonlinear dissipation is introduced to suppress oscillations and to achieve the robust shock-capturing capability. This strategy successfully reduces the numerical dissipation so that turbulence-like high-wavenumber fluctuations can be sustained [51].

However, based on many observations [51][53], tailored nonlinear dissipation instead of constant low dissipation is needed in nonsmooth regions to mitigate numerical artifacts caused by the low-dissipation linear background schemes. Therefore, a framework to construct arbitrarily high-order low-dissipation

shock-capturing schemes with flexible and controllable nonlinear dissipation for convection-dominated problems is essential.

4.1.2   Summary of the publication

In this paper a flexible framework for constructing new shock-capturing TENO schemes is proposed. Six- and eight-point new schemes are developed, and their performance is demonstrated by conducting a set of critical benchmark cases. The conclusions are as follows.

The new framework establishes a unified concept of TENO schemes with classical nonlinear limiters for shock-capturing. Three stages are involved, (a) evaluating of candidate numerical fluxes and labelling each candidate stencil as smooth or nonsmooth by a ENO-like stencil selection procedure; (b) filtering the nonsmooth candidate stencils by an extra nonlinear limiter; (c) formulating the high-order reconstruction by combing the candidate stencils with optimal linear weights.

In smooth regions, all candidate stencils are identified as smooth by the TENO stencil selection procedure and consequently new scheme recovers to TENO. In nonsmooth regions, stable shock-capturing capability is achieved since the nonsmooth candidates contributed to the final reconstructions are filtered to be oscillation-free by extra limiters.

The present framework can be applied to a wide range of limiters, such as TVD and MP. Such different nonlinear limiters are deployed straightforwardly to construct a flexible framework with shock-capturing low-dissipation TENO schemes. These new schemes enable flexible control of dissipation in nonsmooth regions. A wide range of adjustable nonlinear dissipation can be considered in the current framework without affecting global dissipation and detriment to accuracy in low-wavenumber regions.

4.1.3   Individual contributions of the candidate

This article Appendix A.1 was published in the international peer-reviewed journal *Journal of Computational Physics*. My contribution to this work was the development of the method and the code. I have performed numerical validations, analyzed the results, and wrote the manuscript.

4.2 A family of fast multi-resolution ENO schemes for compressible flows

Y. Li, L. Fu and N.A. Adams (2023)

4.2.1 State of the art

To improve the numerical robustness of the very-high-order schemes, schemes with recursive-order-reduction [89] are proposed. For instance, Zhu and Shu [90] develop the finite-difference and finite-volume multi-resolution WENO schemes based on a hierarchy of nested unequal-sized central spatial stencils. Following the nonlinear weighting concept of central WENO schemes [91][92], arbitrary positive linear weights can be employed and the resulting schemes have a gradual degrading of accuracy near discontinuities. As the most recent innovation, the high-order TENO schemes improve the numerical robustness and reduce the unnecessary numerical dissipation by a new candidate stencil arrangement and a novel ENO-like stencil selection strategy [15][51][93]. In contrast to the WENO-like smooth convex combination of candidate stencils, the TENO scheme either deploys a candidate stencil with its optimal linear weight or discards it completely when crossed by a discontinuity. The TENO scheme has been extended to unstructured meshes [94] and multi-resolution methods.

However, the aforementioned WENO and TENO schemes are rather expensive especially for the very-high-order reconstructions. In addition, the construction of odd and even-point scheme reconstruction is not in a unified framework. In this paper, we aims to propose an efficient very-high-order scheme with improved robustness and gradual degrading of accuracy order near discontinuities.

4.2.2 Summary of the publication

In this work, a new family of high-order shock-capturing FMRENO schemes has been proposed. The major contributions are summarized as follows: Based on the MP concept, the construction of the new FMRENO schemes consists of three main phases, i.e., (1) preparing polynomial-based candidate stencils from high- to low-orders in a hierarchical manner; (2) providing a local regularity criterion by calculating the MP upper and lower bounds. A candidate stencil is judged to be smooth only when the reconstructed cell interface flux locates within the MP bounds; (3) formulating the final cell interface reconstruction scheme by selecting the higher-order (or better spectra) candidate stencil, which is judged to be smooth. If all candidate stencils are judged to be nonsmooth by the MP criterion, the smoothest stencil, with which the reconstructed cell interface flux departs from the MP bounds the least, will be adopted as the final reconstruction scheme.

The new framework achieves the multi-resolution property by adaptively selecting the targeted reconstruction scheme from the candidate stencils of different orders according to the local flow regularities. Specifically, in smooth regions, the candidate stencil with the largest stencil width will be adopted for restoring the desired high-order accuracy. In the vicinity of discontinuities, the good non-oscillatory property will be achieved by selecting the candidate reconstruction satisfying the MP criterion. For the wave-like structures, the low-dissipation property can be approached by choosing the smooth candidate stencils with higher accuracy order or better spectral properties.

The present framework can be straightforwardly extended to arbitrarily very-high-order reconstructions with a tiny complexity increase. Compared to the standard W/TENO schemes, the computational efficiency of FMRENO schemes is substantially higher by avoiding the expensive evaluations of the smoothness indicators. Moreover, the efficiency improvement is more impressive with higher-order reconstructions.

4.2.3 Individual contributions of the candidate

This article Appendix A.2 was published in the international peer-reviewed journal *Journal of Scientific Computing*. My contribution to this work was the development of the method and the code. I have performed numerical validations, analyzed the results, and wrote the manuscript.

4.3 A six-point shock-capturing scheme with neural network

Y. Li, L. Fu and N.A. Adams (2021)

4.3.1 State of the art

Inspired by the observation that different measurement methods of non-smooth sub-stencils can affect the schemes' performance significantly, several smoothness indicators are proposed to get a larger variation as the sub-stencil moves from a smooth profile to a discontinuous profile. In WENO schemes, smoothness of sub-stencils are measured depending on functions of low-order or high-order derivatives. TENO [15] and WENO-CU6 [95] schemes introduce scale separation to guarantee a distinguish identification of non-smooth sub-stencil. Additional, Wu et al. [46] proposed a four stencil smoothness indicator which is constant for sine functions and has good stability near discontinuities. These newly proposed smoothness indicators try to introduce more variants, i.e sine map function or total variations, to detect occurrence and location of a shock before applying any of weighting strategies more accurately.

However, these smoothness indicators are designed at some level of empiricism. Given the rise of the interest in data-driven methods in fluid mechanics, it is not surprising that these methods have also been investigated for the construction of smoothness indicator. As the data-driven methods can provide high degree of complexity of the underlying input-output mapping, it is helpful to expand the possibility to design powerful smoothness indicators rather than being restricted to common used feature variables.

Regarding to numerical reconstruction schemes, two main approaches have been found in recent researches: (i) data-driven shock indicator [25][26], and (ii) data-driven enhancement of specific discretization scheme [23][24]. An example of shock detection based on neural network architectures is presented in [27], where the network is trained to serve as a troubled-cell indicator and an extension to two dimensional is present in [86]. Morgan et al. also propose an MLP based shock detector for a high order finite element scheme [87]. However, as the efforts are taken to train a data-driven indicator to control the switch between different schemes, the design of high-order scheme is decoupled from the network training. As an alternative approach, [23][24] train different types of neural networks to modify the coefficients of a baseline polynomial high-order schemes directly. The drawbacks of these designs are that solutions are suffering numerical oscillations, particularly in the vicinity of the shock. Moreover, as the coefficients predicted by the models are trained by the solution manifold, the trained coefficients are indeed equation-specific approximations for the spatial derivatives schemes.

4.3.2 Summary of the publication

In this work, we propose an alternative technique based on ANNs, which can be interpreted as parameter-free, universal black-box to suggest the smoothness of the sub-stencil. We introduce a neural network architecture, i.e MLP to provide a high degree of complexity of the underlying input-output mapping. This mapping are conducted through grouped neuron layers, which process data from an input of flow field information to an output of the choice of sub-stencils which serve as binary labels. After training the neural network with a properly constructed dataset, it is able to predict the output labels for scaled samples not in the training set. As the neural based model is only used to suggest the selection sub-stencils, this operator may

additionally ensure the boundedness of the solution by appropriate limiting. Besides, as the labels are binary options which indicate the smoothness of sub-stencils, implicit neural based ENO is obtained.

The new framework establishes a novel concept of the neural based ENO scheme for shock-capturing. As the ENO-like stencil selection can be decoupled from the design of high-order numerical schemes, results may ensure the boundedness of the solution by appropriate global smooth function.

The present framework can be applied to different types of hyperbolic functions, such as linear advection function and Euler functions. In practical applications, the NENO scheme can be deployed straightforwardly as a classical high-order schemes, which shows an improved universality compared to other neural based high-order schemes.

For now, while the network is capable of essentially mimicking or even improving the state-of-the-art high order schemes, the number of neurons and the associated cost of the network are substantial which is a common problem in [96]. However, it is a pre-concept study to demonstrate the potential of using neural network to design applicable high-order schemes.

4.3.3   Individual contributions of the candidate

This article was published in the international peer-reviewed conference paper *Proceedings of International Conference of Numerical Analysis and Applied Mathematics ICNAAM 2021*. My contribution to this work was the development of the method and the code. I have performed numerical validations, analyzed the results, the performance tests, and wrote the manuscript.

Chapter 5

Conclusions and outlooks

5.1   Conclusions

In this work, several numerical methods are developed from new insight and new technique to construct high-order low-dissipation schemes. First, a framework to construct arbitrarily high-order low-dissipation shock-capturing schemes with flexible and controllable nonlinear dissipation for convection-dominated problems is proposed. Through the adaptation of nonlinear limiters, nonlinear dissipation in the newly proposed framework can be controlled separately without affecting the performance in smooth regions. Second, a new class of high-order fast multi-resolution essentially non-oscillatory schemes is proposed with an emphasis on both the performance and the computational efficiency. Third, we investigate the potential of integrating machine learning to design low-dissipation ENO schemes. We introduce a deep artificial ANN that can detect locations of discontinuity and build a six-point ENO-type scheme based on a set of smooth and discontinuous training data.

Paper I is inspired by the observations [51][53] that tailored nonlinear dissipation instead of constant low dissipation is needed in nonsmooth regions to mitigate numerical artifacts caused by the low-dissipation linear background schemes. The new framework establishes a unified concept of TENO schemes with classical nonlinear limiters for shock-capturing. With an extra nonlinear limiter, nonsmooth candidate stencils are filtered to be smooth, and the high-order reconstruction are formulated by combing all candidate stencils with optimal linear weights. The main contribution of paper I is that different nonlinear limiters are incorporated to construct a low-dissipation high order scheme in a non-classical way. The key idea is that each nonsmooth candidate stencil contains necessary flow field information, therefore their contributions need to be considered rathar than discarding completely. Following this idea, non-smooth candidate stencils are filtered and their contributions are assembled to form the final reconstruction with their respective optimal linear weights. On smooth candidate stencils, the nonlinear limiter will not be activated and consequently the properties of TENO schemes in smooth regions are maintained. Different choices of the nonlinear limiter are possible, such that a new family of schemes with adjustable nonlinear dissipation in nonsmooth regions is obtained. The new scheme achieves adaptive nonlinear dissipation property without deteriorating the spectral resolution properties of TENO in low-wavenumber regions.

Part II is inspired by the observation that the robustness of very-high-order WENO scheme is limited and the computational efficiency of W/TENO scheme is expensive since the evaluations of the smoothness indicators. To improve the performance, a family of FMRENO schemes for both the odd- and even-order reconstructions in a unified framework is proposed. With a set of predefined candidate

stencils as the multi-resolution representation of local flow scales, a novel stencil se-
lection strategy is proposed to form the final reconstruction. The selection criterion
is provided by the MP limiter [59], with which a candidate stencil is regarded to be
smooth if the reconstructed cell interface flux locates within the upper and lower
bounds of the MP limiter. Then, the optimal smooth stencil with higher-order accu-
racy or better spectral property will be adopted as the final reconstruction scheme.
As a result, the FMRENO scheme achieves the multi-resolution property by adap-
tively selecting the targeted candidate stencil according to the local flow regularity
and degenerates from high- to low-order reconstruction when approaching the dis-
continuities. Moreover, the computational efficiency is improved when compared to
W/TENO since the evaluations of the smoothness indicators are unnecessary.

Part III is an experiment to show the potential of exploiting neural network to
design more advanced high-order numerical method for hyperbolic conservation
laws. we introduce a deep ANN that can detect locations of discontinuity and build
a six-order ENO scheme based on a set of continuous and discontinuous training
data. The new framework establishes a novel concept of the neural based ENO
scheme for shock-capturing. Two stages are involved, (a) use a neural network as
a black box to assist the ENO-like stencil selection procedure; (b) formulating of
the high-order reconstruction by combing the candidate stencils with optimal linear
weights. Compared with other neural based schemes, NENO shows an improved
universality, assured boundedness and accuracy.

5.2   Outlooks

Although several high-order low-dissipation schemes are developed in this work,
the strategy of designing arbitrarily high-order low-dissipation shock-capturing
schemes is still worth being analyzed.

In terms of the adaptive-dissipation schemes, methods to adjust parameters to
control the dispersion and dissipation according to the local flow-field properties
that are quantified by the scale sensor can be considered.

Regarding to the neural-based scheme developed in this work, the current form
is still considerably more expensive than the classical numerical schemes from in
terms of the performance. Compared with other neural based schemes, the NENO
scheme shows an improved universality, assured boundedness and accuracy, espe-
cially the resolution independence. To enhence the performance, future develop-
ment can be considered through the following aspects: (1) using the neural network
to train the coefficient of classical smoothness indicator; (2) train a resolution depen-
dence scheme so a low-resolution solving can be used to replace the high-resolution
results.

Chapter 6

Concluding discussion with respect to the state of the art

Despite substantial progress in the development of numerical schemes in the last decades, the simulation of compressible flows with low-dissipation high-order schemes remains to be a challenge worldwide. Compressible fluid dynamics problems which are relevant to high-speed aircraft, jet engines, rocket motors, high-speed entry into a planetary atmosphere are often encountered in the areas of science and engineering. Nowadays, scientific research is increasingly focused on the precise prediction of fluid dynamics problems including a wide range of spatial and temporal scales and shock waves. To analyze these complex multi-scale and non-linear fluid problems, advanced numerical schemes which can solve the contradictory requests that capture shock-wave stably and resolve multi-scale vortex precisely are proposed.

Popular high-order low-dissipation schemes [9][10][11][15][13][14] based on the classical ENO scheme [12] are well-documented in literature. Among all the high-order low-dissipation schemes, WENO schemes [13][14] are seen as a major milestone because of the great benefits to suppress the spurious oscillations in the vicinity of the discontinuities. However, the excessive numerical dissipation of WENO schemes and the robustness of very-high-order WENO schemes remains to be two unsolved flaws.

In order to reduce dissipation while maintaining high-order accuracy in smooth regions and shock-capturing capability, two main methods have been introduced: (i) decreasing the nonlinear adaptive dissipation [43][44][45], and (ii) optimizing the background counterpart linear scheme [47][48]. Among all the schemes, TENO schemes [15] show great improvement in reducing dissipations. However, based on many observations [51][53], tailored nonlinear dissipation instead of constant low dissipation is needed in nonsmooth regions to mitigate numerical artifacts caused by the low-dissipation linear background schemes. Up to now, the flexible framework to adjust dissipation or computational order between smooth or discontinuity regions has not been proposed in literature so far. In this thesis, a framework which can adjust numerical dissipation flexibly has been proposed and analyzed. The key idea is that rather than discarding completely the nonsmooth candidate stencils, their contributions are filtered by a nonlinear limiter. The filtered candidate stencil contributions are assembled to form the final reconstruction with their respective optimal linear weights. On smooth candidate stencils, the nonlinear limiter will not be activated and consequently the properties of TENO schemes in smooth regions are maintained. Different choices of the nonlinear limiter are possible, such that a new family of schemes with adjustable nonlinear dissipation in nonsmooth regions is obtained.

Another widespread challenge in the high-order low-dissipation scheme is the robustness. To improve the numerical robustness of the very-high-order WENO reconstructions, monotonicity-preserving WENO schemes [59], positivity-preserving WENO schemes [97], WENO schemes with recursive-order-reduction [89] and central WENO schemes [91][92] are proposed. Zhu and Shu [90] develop the finite-difference and finite-volume multi-resolution WENO schemes based on a hierarchy of nested unequal-sized central spatial stencils. However, the aforementioned schemes are rather expensive especially for the very-high-order reconstructions since the calculations of smoothness indicators are inevitable. In this thesis, novel schemes for both the odd- and even-order reconstructions without smoothness calculation in a unified framework is proposed. With a set of predefined candidate stencils as the multi-resolution representation of local flow scales, a novel stencil selection strategy is proposed to form the final reconstruction. The selection criterion aims to select the targeted candidate stencil according to the local flow regularity and the resulting FMRENO scheme achieves the multi-resolution property through degenerating from high- to low-order reconstruction when approaching the discontinuities adaptively. Moreover, the computational efficiency is improved when compared to W/TENO since the evaluations of the smoothness indicators are unnecessary.

Inspired by the observation that different measurement methods of non-smooth sub-stencils can affect the schemes' performance significantly, several smoothness indicators are proposed to get a larger variation as the sub-stencil moves from a smooth profile to a discontinuous profile [46][95]. However, these smoothness indicators are designed at some level of empiricism. Given the rise of the interest in data-driven methods in fluid mechanics, it is not surprising that these methods have also been investigated for the problem at hand. As the data-driven methods can provide high degree of complexity of the underlying input-output mapping, it is helpful to expand the possibility to design powerful smoothness indicators rather than being restricted to common used feature variables. In this thesis, an alternative technique based on ANNs, which can be interpreted as parameter-free, universal model are proposed to suggest the choice of the sub-stencil. Inspired by the design of TENO that the weight of candidate stencils containing discontinuities can be fully removed, we focus on a neural network architecture, i.e MLP to provide a high degree of complexity of the underlying input-output mapping. This mapping are conducted through grouped neuron layers, which process data from an input of flow field information to an output of the choice of sub-stencils which serve as binary labels. After training the neural network with a properly constructed dataset, it is able to predict the output labels for scaled samples not in the training set. As the neural based model is only used to suggest the selection sub-stencils, this operator may additionally ensure the boundedness of the solution by appropriate limiting. Besides, as the labels are binary options which indicate the smoothness of sub-stencils, implicit neural based ENO is obtained.

The findings presented in this thesis improve the performance and robustness of high-order low-dissipation schemes and the proposed modifications are easy to apply to many commonly applied methods.

Bibliography

[1]   Jan Matheis and Stefan Hickel. "On the transition between regular and irregular shock patterns of shock-wave/boundary-layer interactions". In: *Journal of Fluid Mechanics* 776 (2015), pp. 200–234.

[2]   Robert J Fennema and M Hanif Chaudhry. "Simulation of one-dimensional dam-break flows". In: *Journal of Hydraulic Research* 25.1 (1987), pp. 41–51.

[3]   Peter D Lax. "Weak solutions of nonlinear hyperbolic equations and their numerical computation". In: *Communications on pure and applied mathematics* 7.1 (1954), pp. 159–193.

[4]   Mohit Arora and Philip L Roe. "A well-behaved TVD limiter for high-resolution calculations of unsteady flow". In: *Journal of Computational Physics* 132.1 (1997), pp. 3–11.

[5]   Friedemann Kemm. "A comparative study of TVD-limiters – well-known limiters and an introduction of new ones". In: *International Journal for Numerical Methods in Fluids* 67.4 (2011), pp. 404–440.

[6]   Bram Van Leer. "Towards the ultimate conservative difference scheme". In: *Journal of computational physics* 135.2 (1997), pp. 229–248.

[7]   Di Zhang et al. "A refined r-factor algorithm for TVD schemes on arbitrary unstructured meshes". In: *International Journal for Numerical Methods in Fluids* 80.2 (2016), pp. 105–139.

[8]   Phillip Colella. "A direct Eulerian MUSCL scheme for gas dynamics". In: *SIAM Journal on Scientific and Statistical Computing* 6.1 (1985), pp. 104–117.

[9]   Chi-Wang Shu. "High order weighted essentially nonoscillatory schemes for convection dominated problems". In: *SIAM review* 51.1 (2009), pp. 82–126.

[10]   Neumann J. Von and R. Richtmyer. "A method for the numerical calculation of hydrodynamic shocks". In: *Journal of Applied Physics* 21 (1950), p. 232.

[11]   Antony Jameson. "Analysis and design of numerical schemes for gas dynamics, 1: artificial diffusion, upwind biasing, limiters and their effect on accuracy and multigrid convergence". In: *International Journal of Computational Fluid Dynamics* 4 (1994), pp. 171–218.

[12]   A Harten. "High resolution schemes for hyperbolic conservation laws". In: *Journal of Computational Physics* 49 (1983), pp. 357–393.

[13]   Xu Dong Liu, Stanley Osher, and Tony Chan. "Weighted Essentially Non-oscillatory Schemes". In: *Journal of Computational Physics* 115 (1994), pp. 200–212.

[14]   Guang Shan Jiang and C.-W. Shu. "Efficient Implementation of Weighted ENO Schemes". In: *Journal of Computational Physics* 126.1 (1996), pp. 202–228.

[15]   Lin Fu, Xiangyu Y Hu, and Nikolaus A Adams. "A family of high-order Targeted ENO schemes for compressible-fluid simulations". In: *Journal of Computational Physics* 305 (2016), pp. 333–359.

[16]   Yinhao Zhu et al. "Physics-constrained deep learning for high-dimensional surrogate modeling and uncertainty quantification without labeled data". In: *Journal of Computational Physics* 394 (2019), pp. 56–81.

[17]   Amir Mosavi et al. "Prediction of multi-inputs bubble column reactor using a novel hybrid model of computational fluid dynamics and machine learning". In: *Engineering Applications of Computational Fluid Mechanics* 13.1 (2019), pp. 482–492.

[18]   Anand Pratap Singh, Shivaji Medida, and Karthik Duraisamy. "Machine-learning-augmented predictive modeling of turbulent separated flows over airfoils". In: *AIAA journal* 55.7 (2017), pp. 2215–2227.

[19]   S Müller, M Milano, and P Koumoutsakos. "Application of machine learning algorithms to flow modeling and optimization". In: *Annual Research Briefs* (1999), pp. 169–178.

[20]   Linyang Zhu et al. "Machine learning methods for turbulence modeling in subsonic flows around airfoils". In: *Physics of Fluids* 31.1 (2019), p. 015105.

[21]   Kai Fukami, Koji Fukagata, and Kunihiko Taira. "Machine-learning-based spatio-temporal super resolution reconstruction of turbulent flows". In: *Journal of Fluid Mechanics* 909 (2021), A9.

[22]   Ze Jia Zhang and Karthikeyan Duraisamy. "Machine learning methods for data-driven turbulence modeling". In: *22nd AIAA Computational Fluid Dynamics Conference*. 2015, p. 2460.

[23]   Yohai Bar-Sinai et al. "Learning data-driven discretizations for partial differential equations". In: *Proceedings of the National Academy of Sciences* 116.31 (2019), pp. 15344–15349.

[24]   Ben Stevens and Tim Colonius. "Enhancement of shock-capturing methods via machine learning". In: *Theoretical and Computational Fluid Dynamics* (2020).

[25]   Andrea D Beck et al. "A Neural Network based Shock Detection and Localization Approach for Discontinuous Galerkin Methods". In: *arXiv preprint arXiv:2001.08201* (2020).

[26]   Mathew Monfort et al. "A deep learning approach to identifying shock locations in turbulent combustion tensor fields". In: *Modeling, Analysis, and Visualization of Anisotropy*. Springer, 2017, pp. 375–392.

[27]   Deep Ray and Jan S Hesthaven. "An artificial neural network as a troubled-cell indicator". In: *Journal of computational physics* 367 (2018), pp. 166–191.

[28]   Nicolas Gautier et al. "Closed-loop separation control using machine learning". In: *Journal of Fluid Mechanics* 770 (2015), pp. 442–457.

[29]   Kai Fukami et al. "Synthetic turbulent inflow generator using machine learning". In: *Physical Review Fluids* 4.6 (2019), p. 064603.

[30]   David E Rumelhart, Geoffrey E Hinton, and Ronald J Williams. "Learning representations by back-propagating errors". In: *nature* 323.6088 (1986), pp. 533–536.

[31]   Leon O Chua and Lin Yang. "Cellular neural networks: Theory". In: *IEEE Transactions on circuits and systems* 35.10 (1988), pp. 1257–1272.

[32]   Sepp Hochreiter and Jürgen Schmidhuber. "Long short-term memory". In: *Neural computation* 9.8 (1997), pp. 1735–1780.

[33] Alex Graves, Santiago Fernández, and Jürgen Schmidhuber. "Multi-dimensional recurrent neural networks". In: *Artificial Neural Networks–ICANN 2007: 17th International Conference, Porto, Portugal, September 9-13, 2007, Proceedings, Part I 17*. Springer. 2007, pp. 549–558.

[34] Philip L Roe. "Approximate Riemann solvers, parameter vectors, and difference schemes". In: *Journal of Computational Physics* 43.2 (1981), pp. 357–372.

[35] V V Rusanov. "Calculation of interaction of non-steady shock waves with obstacles". In: *USSR J. Comp. Math. Phys.* (1961), pp. 267 –279.

[36] Sigal Gottlieb, Chi-Wang Shu, and Eitan Tadmor. "Strong stability-preserving high-order time discretization methods". In: *SIAM review* 43.1 (2001), pp. 89–112.

[37] Richard Courant, Kurt Friedrichs, and Hans Lewy. "On the partial difference equations of mathematical physics". In: *IBM journal of Research and Development* 11.2 (1967), pp. 215–234.

[38] Sergio Pirozzoli. "Numerical methods for high-speed flows". In: *Annual review of fluid mechanics* 43 (2011), pp. 163–194.

[39] Lin Fu et al. "Shock-induced heating and transition to turbulence in a hypersonic boundary layer". In: *Journal of Fluid Mechanics* 909 (2021), A8.

[40] A K Henrick, T D Aslam, and J M Powers. "Mapped weighted essentially non-oscillatory schemes: achieving optimal order near critical points". In: *Journal of Computational Physics* 207 (2005), pp. 542–567.

[41] Rafael Borges et al. "An improved weighted essentially non-oscillatory scheme for hyperbolic conservation laws". In: *Journal of Computational Physics* 227 (2008), pp. 3191–3211.

[42] Wai-Sun Don and Rafael Borges. "Accuracy of the weighted essentially non-oscillatory conservative finite difference schemes". In: *Journal of Computational Physics* 250 (2013), pp. 347–372.

[43] Andrew K Henrick, Tariq D Aslam, and Joseph M Powers. "Mapped Weighted Essentially Non-oscillatory schemes: achieving optimal order near critical points". In: *Journal of Computational Physics* 207.2 (2005), pp. 542–567.

[44] Rafael Borges et al. "An improved Weighted Essentially Non-oscillatory scheme for hyperbolic conservation laws". In: *Journal of Computational Physics* 227.6 (2008), pp. 3191–3211.

[45] David J Hill and Dale I Pullin. "Hybrid tuned center-difference-WENO method for large eddy simulations in the presence of strong shocks". In: *Journal of Computational Physics* 194.2 (2004), pp. 435–450.

[46] Conghai Wu, Ling Wu, and Shuhai Zhang. "A smoothness indicator constant for sine functions". In: *Journal of Computational Physics* 419 (2020), p. 109661.

[47] M Pino Martín et al. "A bandwidth-optimized WENO scheme for the effective direct numerical simulation of compressible turbulence". In: *Journal of Computational Physics* 220.1 (2006), pp. 270–289.

[48] X Y Hu, Q Wang, and N A Adams. "An adaptive central-upwind Weighted Essentially Non-oscillatory scheme". In: *Journal of Computational Physics* 229 (2010), pp. 8952–8965.

[49] F Acker, RBR Borges, and Bruno Costa. "An improved WENO-Z scheme". In: *Journal of Computational Physics* 313 (2016), pp. 726–753.

[50] Marcos Castro, Bruno Costa, and Wai Sun Don. "High order weighted essentially non-oscillatory WENO-Z schemes for hyperbolic conservation laws". In: *Journal of Computational Physics* 230.5 (2011), pp. 1766–1792.

[51] Lin Fu, Xiangyu Y Hu, and Nikolaus A Adams. "Targeted ENO schemes with tailored resolution property for hyperbolic conservation laws". In: *Journal of Computational Physics* 349 (2017), pp. 97–121.

[52] Lin Fu, Xiangyu Y Hu, and Nikolaus A Adams. "A new class of adaptive high-order Targeted ENO schemes for hyperbolic conservation laws". In: *Journal of Computational Physics* 374 (2018), pp. 724–751.

[53] Lin Fu. "A low-dissipation finite-volume method based on a new TENO shock-capturing scheme". In: *Computer Physics Communications* 235 (2019), pp. 25–39.

[54] Lin Fu, XY Hu, and Nikolaus A Adams. "A Targeted ENO scheme as implicit model for turbulent and genuine subgrid scales". In: *Communications in Computational Physics* 26 (2019), pp. 311–345.

[55] Lin Fu, Xiangyu Y Hu, and Nikolaus A Adams. "Improved Five- and Six-Point Targeted Essentially Non-oscillatory Schemes with Adaptive Dissipation". In: *AIAA Journal* 57.3 (2018), pp. 1143–1158.

[56] Yu Xin Ren, Hanxin Zhang, et al. "A characteristic-wise hybrid compact-WENO scheme for solving hyperbolic conservation laws". In: *Journal of Computational Physics* 192.2 (2003), pp. 365–386.

[57] Bram Van Leer. "Towards the ultimate conservative difference scheme. V. A second-order sequel to Godunov's method". In: *Journal of computational Physics* 32.1 (1979), pp. 101–136.

[58] GD Van Albada, Bram Van Leer, and WWjun Roberts. "A comparative study of computational methods in cosmic gas dynamics". In: *Upwind and High-Resolution Schemes*. Springer, 1997, pp. 95–103.

[59] A Suresh and HT Huynh. "Accurate Monotonicity Preserving schemes with Runge–Kutta time stepping". In: *Journal of Computational Physics* 136.1 (1997), pp. 83–99.

[60] Dinshaw S Balsara and Chi-Wang Shu. "Monotonicity Preserving Weighted Essentially Non-oscillatory schemes with increasingly high order of accuracy". In: *Journal of Computational Physics* 160.2 (2000), pp. 405–452.

[61] Steven L Brunton, Bernd R Noack, and Petros Koumoutsakos. "Machine learning for fluid mechanics". In: *Annual Review of Fluid Mechanics* 52 (2020), pp. 477–508.

[62] Sandeep Pandey, Jörg Schumacher, and Katepalli R Sreenivasan. "A perspective on machine learning in turbulent flows". In: *Journal of Turbulence* 21.9-10 (2020), pp. 567–584.

[63] Kurt Hornik, Maxwell Stinchcombe, and Halbert White. "Multilayer feedforward networks are universal approximators". In: *Neural networks* 2.5 (1989), pp. 359–366.

[64] Dengsheng Chen and Kai Xu. "AReLU: Attention-based Rectified Linear Unit". In: *arXiv preprint arXiv:2006.13858* (2020).

[65] MWMG Dissanayake and Nhan Phan-Thien. "Neural-network-based approximations for solving partial differential equations". In: *communications in Numerical Methods in Engineering* 10.3 (1994), pp. 195–201.

[66] Hyuk Lee and In Seok Kang. "Neural algorithm for solving differential equations". In: *Journal of Computational Physics* 91.1 (1990), pp. 110–131.

[67] Andrew J Meade Jr and Alvaro A Fernandez. "The numerical solution of linear ordinary differential equations by feedforward neural networks". In: *Mathematical and Computer Modelling* 19.12 (1994), pp. 1–25.

[68] Lixin Wang and Jerry M Mendel. "Structured trainable networks for matrix algebra". In: *1990 IJCNN International Joint Conference on Neural Networks*. IEEE. 1990, pp. 125–132.

[69] Isaac E Lagaris, Aristidis Likas, and Dimitrios I Fotiadis. "Artificial neural networks for solving ordinary and partial differential equations". In: *IEEE transactions on neural networks* 9.5 (1998), pp. 987–1000.

[70] Maziar Raissi, Paris Perdikaris, and George E Karniadakis. "Physics-informed neural networks: A deep learning framework for solving forward and inverse problems involving nonlinear partial differential equations". In: *Journal of Computational Physics* 378 (2019), pp. 686–707.

[71] Lu Lu et al. "DeepXDE: A deep learning library for solving differential equations". In: *SIAM Review* 63.1 (2021), pp. 208–228.

[72] Justin Sirignano and Konstantinos Spiliopoulos. "DGM: A deep learning algorithm for solving partial differential equations". In: *Journal of computational physics* 375 (2018), pp. 1339–1364.

[73] Mohammad Amin Nabian and Hadi Meidani. "A deep neural network surrogate for high-dimensional random partial differential equations". In: *arXiv preprint arXiv:1806.02957* (2018).

[74] Guofei Pang, Lu Lu, and George Em Karniadakis. "fPINNs: Fractional physics-informed neural networks". In: *SIAM Journal on Scientific Computing* 41.4 (2019), A2603–A2626.

[75] Dongkun Zhang, Ling Guo, and George Em Karniadakis. "Learning in modal space: Solving time-dependent stochastic PDEs using physics-informed neural networks". In: *SIAM Journal on Scientific Computing* 42.2 (2020), A639–A665.

[76] Liu Yang, Dongkun Zhang, and George Em Karniadakis. "Physics-informed generative adversarial networks for stochastic differential equations". In: *SIAM Journal on Scientific Computing* 42.1 (2020), A292–A317.

[77] Dongkun Zhang et al. "Quantifying total uncertainty in physics-informed neural networks for solving forward and inverse stochastic problems". In: *Journal of Computational Physics* 397 (2019), p. 108850.

[78] Guillaume Bal and Yvon Maday. "A "parareal" time discretization for nonlinear PDE's with application to the pricing of an American put". In: *Recent developments in domain decomposition methods*. Springer, 2002, pp. 189–202.

[79] Yvon Maday and Gabriel Turinici. "The parareal in time iterative solver: a further direction to parallel implementation". In: *Domain decomposition methods in science and engineering*. Springer, 2005, pp. 441–448.

[80] Xuhui Meng et al. "PPINN: Parareal physics-informed neural network for time-dependent PDEs". In: *Computer Methods in Applied Mechanics and Engineering* 370 (2020), p. 113250.

[81] Eric J Parish and Karthik Duraisamy. "A paradigm for data-driven predictive modeling using field inversion and machine learning". In: *Journal of Computational Physics* 305 (2016), pp. 758–774.

[82] H Zhang, TJ Craft, and H Iacovides. "The formulation of the RANS equations for supersonic and hypersonic turbulent flows". In: *The Aeronautical Journal* 125.1285 (2021), pp. 525–555.

[83] Julia Ling, Andrew Kurzawski, and Jeremy Templeton. "Reynolds averaged turbulence modelling using deep neural networks with embedded invariance". In: *Journal of Fluid Mechanics* 807 (2016), pp. 155–166.

[84] Fabrizio Sarghini, G De Felice, and Stefania Santini. "Neural networks based subgrid scale modeling in large eddy simulations". In: *Computers & fluids* 32.1 (2003), pp. 97–108.

[85] Andrea Beck, David Flad, and Claus-Dieter Munz. "Deep neural networks for data-driven LES closure models". In: *Journal of Computational Physics* 398 (2019), p. 108910.

[86] Deep Ray and Jan S Hesthaven. "Detecting troubled-cells on two-dimensional unstructured grids using a neural network". In: *Journal of Computational Physics* 397 (2019), p. 108845.

[87] Nathaniel R Morgan et al. "A machine learning approach for detecting shocks with high-order hydrodynamic methods". In: *AIAA Scitech 2020 Forum*. 2020, p. 2024.

[88] Seongmun Jung and Oh Joon Kwon. "A Flux Reconstruction Model Based on an Artificial Neural Network". In: *AIAA Scitech 2021 Forum*. 2021, p. 0243.

[89] G A Gerolymos, D Sénéchal, and I Vallet. "Very-high-order WENO schemes". In: *Journal of Computational Physics* 228.23 (2009), pp. 8481–8524.

[90] Jun Zhu and Chi-Wang Shu. "A new type of multi-resolution WENO schemes with increasingly higher order of accuracy". In: *Journal of Computational Physics* 375 (2018), pp. 659–683.

[91] Doron Levy, Gabriella Puppo, and Giovanni Russo. "Central WENO schemes for hyperbolic systems of conservation laws". In: *ESAIM: Mathematical Modelling and Numerical Analysis-Modélisation Mathématique et Analyse Numérique* 33.3 (1999), pp. 547–571.

[92] Doron Levy, Gabriella Puppo, and Giovanni Russo. "Compact central WENO schemes for multidimensional conservation laws". In: *SIAM Journal on Scientific Computing* 22.2 (2000), pp. 656–672.

[93] Lin Fu. "A hybrid method with TENO based discontinuity indicator for hyperbolic conservation laws". In: *Communications in Computational Physics* 26.4 (2019), pp. 973–1007.

[94] Zhe Ji, Tian Liang, and Lin Fu. "A class of new high-order finite-volume TENO schemes for hyperbolic conservation laws with unstructured meshes". In: *Journal of Scientific Computing* 92 (2022), p. 61.

[95] XY Hu, Q Wang, and Nikolaus A Adams. "An adaptive central-upwind weighted essentially non-oscillatory scheme". In: *Journal of Computational Physics* 229.23 (2010), pp. 8952–8965.

[96] Rémi Abgrall and Maria Han Veiga. "Neural Network-Based Limiter with Transfer Learning". In: *Communications on Applied Mathematics and Computation* (2020), pp. 1–41.

[97] Xiangxiong Zhang and Chi-Wang Shu. "Positivity-preserving high order finite difference WENO schemes for compressible Euler equations". In: *Journal of Computational Physics* 231.5 (2012), pp. 2245–2258.

Appendix A

Original journal papers

Here, the peer-reviewed journal publications of the present work are attached.

A.1 Paper I

Yue Li, Lin Fu, Nikolaus A. Adams

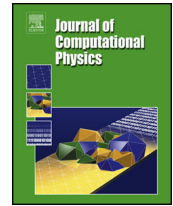## A low-dissipation shock-capturing framework with flexible nonlinear dissipation control

Contribution: My contribution to this work was the development of the method and the corresponding computer code for its implementation. I performed simulations and analyzed the results, and wrote the manuscript for the publication.

A low-dissipation shock-capturing framework with flexible nonlinear dissipation control

Yue Li [a], Lin Fu [b,*], Nikolaus A. Adams [a]

[a] *Chair of Aerodynamics and Fluid Mechanics, Department of Mechanical Engineering, Technical University of Munich, 85748 Garching, Germany*
[b] *Center for Turbulence Research, Stanford University, Stanford, CA 94305, USA*

ABSTRACT

In this work, a framework to construct arbitrarily high-order low-dissipation shock-capturing schemes with flexible and controllable nonlinear dissipation for convection-dominated problems is proposed. While a set of candidate stencils of incremental width is constructed, each one is indicated as smooth or nonsmooth by the ENO-like stencil selection procedure proposed in the targeted essentially non-oscillatory (TENO) scheme (Fu et al. 2016 [9]). Rather than being discarded directly as with TENO schemes, the nonsmooth candidates are filtered by an extra nonlinear limiter, such as a monotonicity-preserving (MP) limiter or a total variation diminishing (TVD) limiter. Consequently, high-order reconstruction is achieved by assembling candidate fluxes with optimal linear weights since they are either smooth reconstructions or filtered ones which feature good non-oscillation property. A weight renormalization procedure as with the standard TENO paradigm is not necessary. This new framework concatenates the concepts of TENO, WENO and other nonlinear limiters for shock-capturing, and provides a new insight to designing low-dissipation nonlinear schemes. Through the adaptation of nonlinear limiters, nonlinear dissipation in the newly proposed framework can be controlled separately without affecting the performance in smooth regions. Based on the proposed framework, a family of new six- and eight-point nonlinear schemes with controllable dissipation is proposed. A set of critical benchmark cases involving strong discontinuities and broadband fluctuations is simulated. Numerical results reveal that the proposed new schemes capture discontinuities sharply and resolve the high-wavenumber fluctuations with low dissipation, while maintaining the desired accuracy order in smooth regions.

© 2020 Elsevier Inc. All rights reserved.

1. Introduction

High-order and high-resolution shock-capturing schemes are popular numerical methods to solve compressible fluid problems, which may involve discontinuities. However, there still is a need for flexible environments to design such schemes that are highly accurate in smooth regions with low numerical dissipation and can capture discontinuities with low parasitic noise in smooth regions near discontinuous.

Among all the schemes, weighted essentially non-oscillatory (WENO) schemes, first proposed by Liu et al. [1] and further improved by Jiang and Shu [2], probably are the most widely accepted discretization schemes. These schemes are devel-

---

oped from the essentially non-oscillatory (ENO) concept [3], which selects the smoothest stencil from a set of candidates to prevent the reconstruction from crossing discontinuities. Instead of selecting the smoothest candidate, WENO deploys a convex combination of all candidate stencils to achieve high-order accuracy in smooth regions. In nonsmooth regions, reduced weights are assigned to the stencils through nonlinear smoothness indicators. Thus, spurious numerical oscillations can be largely avoided. However, practical implementations reveal that the WENO-JS scheme [2] is rather dissipative and may lose the accuracy order near critical points due to the strong nonlinear adaptation within the weighting strategy.

In order to reduce dissipation while maintaining high-order accuracy in smooth regions and shock-capturing capability, two main methods have been introduced: (i) decreasing the nonlinear adaptive dissipation [4][5][6], and (ii) optimizing the background counterpart linear scheme [7][8]. Henrick et al. [4] suggest that restoring the optimal accuracy order near critical points can resolve the over-dissipation issue. Necessary and sufficient conditions have been derived and a mapping strategy based on classical WENO, referred to as WENO-M, has been developed accordingly. However, as investigated by Borges et al. [5], the improvements demonstrated by WENO-M [4] over WENO-JS result from larger weights of nonsmooth candidate stencils and less nonlinear adaptive dissipation, rather than from higher accuracy near critical points. To further decrease the nonlinear adaptive dissipation, a new smoothness indicator has been proposed by Borges et al. [5], which introduces a global high-order undivided difference into the weighting strategy of the WENO-JS scheme. As an alternative approach [6], the nonlinear dissipation adaptation can be controlled by comparing the ratio between the largest and the smallest calculated smoothness indicator. By introducing a problem-dependent threshold, adaptation is eliminated when the ratio is below the threshold. The aforementioned WENO-like schemes reduce the dissipation of the classical WENO significantly. However, they are still too dissipative for resolving turbulence-like high-wavenumber fluctuations. Besides decreasing the nonlinear adaptive dissipation, optimizing the background counterpart linear scheme of WENO also can improve the overall dissipation property. The WENO-SYMOO [7] and WENO-CU6 [8] schemes optimize the background scheme as a central scheme by introducing the contribution of the downwind stencil. However, anti-dissipation is inherently built in for a certain wavenumber range, which may be problematic for critical applications. Therefore, in terms of designing low-dissipation shock capturing schemes, the strategy of choosing a stable linear scheme with upwind-biased candidate stencils as a background scheme and then optimizing the nonlinear dissipation adaptation to its limit is preferable.

To further reduce the dissipation by suppressing nonlinear adaptation and achieve stable shock-capturing capability, a family of high-order targeted ENO (TENO) schemes has been proposed by Fu et al. [9][10][11][12]. Unlike the WENO-like smooth convex combination, TENO either adopts a candidate stencil with its optimal weight for the final reconstruction or discards it completely when crossed by a genuine discontinuity. This procedure is ensured by a cut-off parameter C_T, which identifies the smooth and nonsmooth regions. In smooth regions, nonlinear adaptation is unnecessary and the numerical dissipation is reduced to that of the linear background scheme. In nonsmooth regions, nonlinear dissipation is introduced to suppress oscillations and to achieve the robust shock-capturing capability. This strategy successfully reduces the numerical dissipation so that turbulence-like high-wavenumber fluctuations can be sustained [10]. However, based on many observations [10][12], tailored nonlinear dissipation instead of constant low dissipation is needed in nonsmooth regions to mitigate numerical artifacts caused by the low-dissipation linear background schemes.

An alternative solution is to introduce the hybrid concept, for which the efficient linear scheme is applied in smooth regions while the expensive nonlinear scheme is adopted in the vicinity of discontinuities. Adams and Shariff [13] have introduced the concept of hybridization of a high-resolution compact scheme with the nonlinear high-order ENO scheme. Pirozzoli [14] proposes a conservative hybrid scheme for resolving the compressible turbulent flows by combining a compact scheme with WENO. However, the performance of these hybrid methods strongly depends on an effective discontinuity indicator [15], which is mostly case-sensitive.

In this paper, we propose an extended framework based on the TENO concept. The main objective is to achieve adaptive nonlinear dissipation property without deteriorating the spectral resolution properties of TENO in low-wavenumber regions. The key idea is that rather than discarding completely the nonsmooth candidate stencils, their contributions are filtered by a nonlinear limiter. The filtered candidate stencil contributions are assembled to form the final reconstruction with their respective optimal linear weights. On smooth candidate stencils, the nonlinear limiter will not be activated and consequently the properties of TENO schemes in smooth regions are maintained. Different choices of the nonlinear limiter are possible, such that a new family of schemes with adjustable nonlinear dissipation in nonsmooth regions is obtained.

The rest of this paper is organized as follows. In section 2, the concept of the finite-difference high-order reconstruction schemes and the construction of standard TENO schemes are briefly reviewed. In section 3, a general framework to construct nonlinear shock-capturing schemes is proposed and the filtering strategy for nonsmooth candidate stencils are elaborated. In section 4, a set of benchmark cases is considered for assessment of the developed schemes. The concluding remarks are given in the last section.

2. Concepts of standard TENO schemes for hyperbolic conservation laws

To facilitate the presentation, we consider a one-dimensional scalar hyperbolic conservation law

$$\frac{\partial u}{\partial t} + \frac{\partial}{\partial x} f(u) = 0, \tag{1}$$

where u and f denote the conservative variable and the flux function respectively. The characteristic signal speed is assumed to be positive $\frac{\partial f(u)}{\partial u} > 0$. The developed schemes can be extended to systems of conservation laws and multi-dimensional problems in a straight-forward manner.

For a uniform Cartesian mesh with cell centers $x_i = i\Delta x$ and cell interfaces $x_{i+1/2} = x_i + \frac{\Delta x}{2}$, the spatial discretization results in a set of ordinary differential equations

$$\frac{du_i(t)}{dt} = -\frac{\partial f}{\partial x}\Big|_{x=x_i}, \quad i = 0, \cdots, n, \tag{2}$$

where u_i is a numerical approximation to the point value $u(x_i, t)$. The semi-discretization with Eq. (2) can be further discretized by a conservative finite-difference scheme as

$$\frac{du_i}{dt} = -\frac{1}{\Delta x}(h_{i+1/2} - h_{i-1/2}), \tag{3}$$

where the primitive function $h(x)$ is implicitly defined by

$$f(x) = \frac{1}{\Delta x}\int_{x-\Delta x/2}^{x+\Delta x/2} h(\xi)d\xi, \tag{4}$$

and $h_{i\pm1/2} = h(x_i \pm \frac{\Delta x}{2})$. A high-order approximation of $h(x)$ at the cell interface has to be reconstructed from the cell-averaged values of $f(x)$ at the cell centers. Eq. (3) can be written as

$$\frac{du_i}{dt} \approx -\frac{1}{\Delta x}(\widehat{f}_{i+1/2} - \widehat{f}_{i-1/2}), \tag{5}$$

where $\hat{f}_{i\pm1/2}$ denotes the high-order approximate numerical fluxes and can be computed from a convex combination of $K-2$ candidate-stencil fluxes

$$\widehat{f}_{i+1/2} = \sum_{k=0}^{K-3} w_k \widehat{f}_{k,i+1/2}. \tag{6}$$

A $(r_k - 1)$-degree polynomial is assumed for each candidate stencil as

$$h(x) \approx \hat{f}_k(x) = \sum_{l=0}^{r_k-1} a_{l,k} x^l, \tag{7}$$

where r_k denotes the point number of candidate stencil k. After substituting Eq. (7) into Eq. (4) and evaluating the integral functions at the stencil nodes, the coefficients $a_{l,k}$ are determined by solving the resulting system of linear algebraic equations.

For hyperbolic conservation laws, discontinuities may occur even when the initial condition is smooth enough. The challenge is to develop a reconstruction scheme which is high-order accurate in smooth regions and captures discontinuities sharply and stably in nonsmooth regions. In the following, we recall essential elements of the recently proposed TENO [9][10][11][12][16] concept.

2.1. Candidate stencil arrangement

As shown in Fig. 1, arbitrarily high-order TENO schemes are constructed from a set of candidate stencils with incremental width [9]. The sequence of stencil width r varying versus the accuracy order K is as

$$\{r_k\} = \begin{cases} \{3, 3, 3, 4, \cdots, \underbrace{\frac{K+2}{2}}_{0,\cdots,K-3}\}, & \text{if } \mathrm{mod}\,(K,2) = 0, \\ \{3, 3, 3, 4, \cdots, \underbrace{\frac{K+1}{2}}_{0,\cdots,K-3}\}, & \text{if } \mathrm{mod}\,(K,2) = 1. \end{cases} \tag{8}$$

Note that, although the general candidate stencil arrangement of classical WENO schemes has some limitations [9], the following ideas discussed will still be applicable even if it is employed.
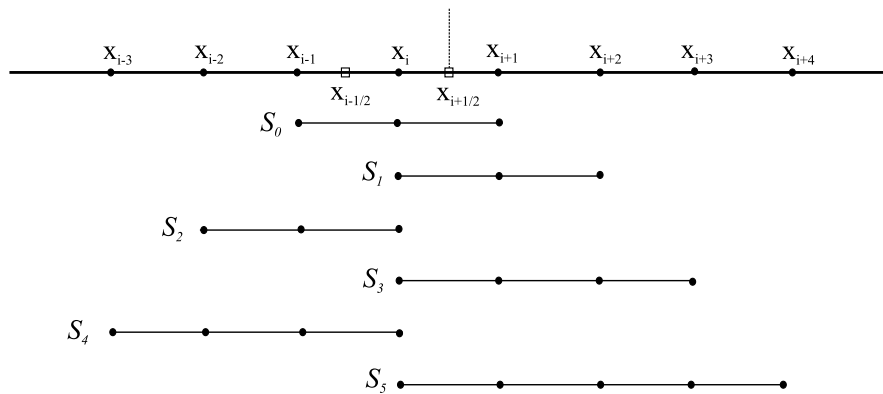
Fig. 1. Candidate stencils with incremental width towards high-order reconstruction. While the first three stencils are identical to that of the classical fifth-order WENO-JS scheme, all candidate stencils possess at least one upwind point. The maximum Kth-order scheme can be constructed by combining candidates ranging from S_0 to S_{K-3}. The advantage of such candidate stencil arrangement over that of classical WENO schemes is the robustness improvement in very-high-order versions.

2.2. Scale-separation procedure

To isolate effectively discontinuities from smooth regions, smoothness indicators with strong scale-separation capability are given as [9]

$$\gamma_k = \left(C + \frac{\tau_K}{\beta_{k,r} + \varepsilon} \right)^q, \, k = 0, \cdots, K - 3, \tag{9}$$

where $\varepsilon = 10^{-40}$ is introduced to prevent the zero denominator. The parameters $C = 1$ and $q = 6$ are chosen for strong scale separation. Following Jiang and Shu [2], by counting all the possible high-order undivided differences, $\beta_{k,r}$ can be given as

$$\beta_{k,r} = \sum_{j=1}^{r-1} \Delta x^{2j-1} \int_{x_{i-1/2}}^{x_{i+1/2}} \left(\frac{d^j}{dx^j} \hat{f}_k(x) \right)^2 dx. \tag{10}$$

A sixth-order τ_K, which allows for good stability with a reasonable large CFL number, can be constructed as [10]

$$\tau_K = \left| \beta_K - \frac{1}{6} (\beta_{1,3} + \beta_{2,3} + 4\beta_{0,3}) \right| = O(\Delta x^6), \tag{11}$$

where the β_K measures the global smoothness on the K-point full stencil.

2.3. ENO-like stencil selection

For TENO schemes [9], the measured smoothness indicators are first normalized as

$$\chi_k = \frac{\gamma_k}{\sum_{k=0}^{K-3} \gamma_k}, \tag{12}$$

and subsequently filtered by a sharp cut-off function

$$\delta_k = \begin{cases} 0, & \text{if } \chi_k < C_T, \\ 1, & \text{otherwise.} \end{cases} \tag{13}$$

In such a way, all candidate stencils are then identified to be either sufficiently smooth or nonsmooth with a discontinuity crossing the stencil.

2.4. Nonlinear adaptation strategy for C_T

Although the above weighting strategy is sufficient to separate smooth regions from discontinuities, undesirable numerical dissipation is generated for turbulence-like high-wavenumber fluctuations since they are treated in a similar manner as discontinuities. Previous research reveals that the low-order undivided difference is more sensitive to distinguish high-wavenumber fluctuations from genuine discontinuities than high-order undivided differences [11][17][18].

Motivated by Ren et al. [19], the local smoothness of flow field can be indicated by

$$
\begin{cases}
m = 1 - \min(1, \frac{\eta_{i+1/2}}{C_r}), \\
\eta_{i+1/2} = \min(\eta_{i-1}, \eta_i, \eta_{i+1}, \eta_{i+2}),
\end{cases}
\tag{14}
$$

where

$$
\eta_i = \frac{|2\Delta f_{i+1/2} \Delta f_{i-1/2}| + \epsilon}{(\Delta f_{i+1/2})^2 + (\Delta f_{i-1/2})^2 + \epsilon},
\tag{15}
$$

$$
\Delta f_{i+1/2} = f_{i+1} - f_i, \qquad \epsilon = \frac{0.9 C_r}{1 - 0.9 C_r} \xi^2,
\tag{16}
$$

and the parameters $\xi = 10^{-3}$, $C_r = 0.23$ are used for the eight-point TENO schemes [17]. Low numerical dissipation for turbulence-like high-wavenumber fluctuations is achieved by adjusting the cut-off parameter C_T as

$$
\begin{cases}
g(m) = (1 - m)^4 (1 + 4m), \\
\beta = \alpha_1 - \alpha_2 (1 - g(m)), \\
C_T = 10^{-[\beta]},
\end{cases}
\tag{17}
$$

where $[\beta]$ denotes the maximum integer which is not larger than β. $g(m)$ is a smoothing kernel based mapping function, and $\alpha_1 = 10.5$, $\alpha_2 = 3.5$ are set for the eight-point TENO schemes [17]. The eight-point TENO scheme with C_T adaptation is referred to as TENO8A in this paper.

2.5. The final high-order reconstruction

In order to remove contributions from candidate stencils containing discontinuities, optimal weights d_k subjected to the cut-off δ_k are renormalized as

$$
w_k = \frac{d_k \delta_k}{\sum_{k=0}^{K-3} d_k \delta_k}.
\tag{18}
$$

The Kth-order reconstructed numerical flux evaluated at cell face $i + \frac{1}{2}$ is assembled as

$$
\hat{f}_{i+1/2}^K = \sum_{k=0}^{K-3} w_k \hat{f}_{k,i+1/2}.
\tag{19}
$$

3. New framework with flexible nonlinear dissipation control

In this section, we describe the details of the new reconstruction framework for TENO with flexible nonlinear dissipation control. The new schemes are referred to as TENO-M schemes hereafter. The advantages of TENO-M schemes are not only in keeping the contribution of nonsmooth stencils but also maintaining the performance improvement of TENO. The possibility of keeping nonsmooth stencils rather than abandoning them entirely is achieved by a flexible filtering procedure. As the nonsmooth stencils are filtered to be oscillation free by an extra limiter, they are able to contribute to the final reconstruction without detriment to computational stability. In regions of smooth stencils, nonlinear limiters will not be activated and consequently the performance of TENO in terms of restoring the background linear scheme in low-wavenumber regions is maintained.

3.1. Evaluation of the candidate numerical fluxes and label stencils based on smoothness indicator

As shown in Fig. 1, arbitrarily high-order TENO schemes, i.e. both odd and even order, are constructed from a set of candidate stencils with incremental width [9]. The numerical flux $\widehat{f}_{k,i+1/2}$ of the candidate stencil S_k is evaluated by solving the linear system results from Eq. (7) and Eq. (4). The corresponding coefficients for TENO schemes up to eighth-order accuracy are presented in Table 1.

Based on the smoothness indicator, each candidate stencil is identified as smooth or nonsmooth by the ENO-like stencil selection procedure, i.e. Eq. (12) and Eq. (13).

Table 1
Numerical flux $\widehat{f}_{k,i+1/2} = \sum_m c_m f_m$ evaluated from the candidate stencil S_k.

$\widehat{f}_{k,i+1/2}$	c_{i-3}	c_{i-2}	c_{i-1}	c_i	c_{i+1}	c_{i+2}	c_{i+3}	c_{i+4}
$k=0$			$-\frac{1}{6}$	$\frac{5}{6}$	$\frac{2}{6}$			
$k=1$				$\frac{2}{6}$	$\frac{5}{6}$	$-\frac{1}{6}$		
$k=2$		$\frac{2}{6}$	$-\frac{7}{6}$	$\frac{11}{6}$				
$k=3$				$\frac{3}{12}$	$\frac{13}{12}$	$-\frac{5}{12}$	$\frac{1}{12}$	
$k=4$	$-\frac{3}{12}$	$\frac{13}{12}$	$-\frac{23}{12}$	$\frac{25}{12}$				
$k=5$				$\frac{12}{60}$	$\frac{77}{60}$	$-\frac{43}{60}$	$\frac{17}{60}$	$-\frac{3}{60}$

3.2. Filtering of the nonsmooth stencils with an extra limiter

Different from the standard TENO schemes, where the detected nonsmooth stencils will be discarded completely, in the present framework, they are filtered by a specific nonlinear limiter and then adopted for the final reconstruction by

$$\hat{f}^{\mathrm{M}}_{k,i+1/2} = \begin{cases} f^{\lim}_{k,i+1/2} & \text{if } \delta_k = 0, \\ \hat{f}_{k,i+1/2}, & \text{otherwise}, \end{cases} \tag{20}$$

where $f^{\lim}_{k,i+1/2}$ denotes the numerical flux filtered by a nonlinear limiter. A monotonicity-preserving limiter [20], a fifth-order TVD limiter [21] and a second-order Van Albada limiter [22][23] are deployed to derive the $f^{\lim}_{k,i+1/2}$ and are referred to as $f^{\mathrm{MP}}_{k,i+1/2}$, $f^{\mathrm{TVD5}}_{k,i+1/2}$, and $f^{\mathrm{VA}}_{k,i+1/2}$ respectively. Consequently, the nonlinear numerical dissipation property of TENO schemes can be tailored by deploying different nonlinear limiters to the nonsmooth stencils. The accuracy order and low-dissipation property of the resulting TENO schemes are maintained in smooth and low-wavenumber regions.

This new framework connects the concepts of TENO and other nonlinear limiters for shock-capturing. Although only three nonlinear limiters are considered in this paper, any other established limiters can be introduced into Eq. (20).

3.2.1. TVD nonlinear limiter

Following [24], TVD nonlinear limiters enforce the TVD property by introducing the slope function $\phi(r)$ to limit the gradient variation. Several second- and third-order TVD schemes with different slope functions have been developed, e.g. with the Minmod limiter, the Superbee limiter and the Van Leer limiter [25][26][27]. Here, we take a Van Albada limiter as an example to exemplify its implementation. Following [28], the slope function of a Van Albada limiter $\phi(r)_{\mathrm{VA}}$ is defined as

$$\phi_{\mathrm{VA}}(r) = \frac{2r}{r^2 + 1}, \tag{21}$$

and the slope ratio r based on a three-cell stencil centered at i is

$$r = \delta^+/\delta^-, \tag{22}$$

where $\delta^- = f_i - f_{i-1}$, $\delta^+ = f_{i+1} - f_i$. Therefore, the reconstruction scheme filtered by a Van Albada limiter can be written as

$$f^{\mathrm{VA}}_{i+\frac{1}{2}} = f_i + \frac{\phi_{\mathrm{VA}}}{4}[(1 - \kappa\phi_{\mathrm{VA}})\delta^- + (1 + \kappa\phi_{\mathrm{VA}})\delta^+]. \tag{23}$$

In smooth regions, a third-order reconstruction is restored by setting $\kappa = 1/3$ and the resulting TENO schemes are referred to as TENO-M-VA.

However, these reconstructions fail to incorporate concrete information of the variation of δ^+ except for the monotonicity constraint. Kim et al. [21] propose to incorporate the curvature information of δ^+ into TVD limiters by the proper choice of an optimal variation function β and develop a class of high-order TVD limiters. As suggested in [21], the slope function of a high-order TVD limiter $\phi(r)_{\mathrm{TVD5}}$ based on a five-cell stencil centered at i is defined as

$$\phi_{\mathrm{TVD5}}(r) = \max(0, \min(\alpha, \alpha r, \beta)), \tag{24}$$

where $\alpha = 2$ and β is given as

$$\beta = \frac{-2/r_{j-1} + 11 + 24r_j - 3r_j r_{j+1}}{30}. \tag{25}$$

A reconstruction scheme filtered by a high-order TVD limiter can be written as

$$f^{\mathrm{TVD5}}_{i+\frac{1}{2}} = f_i + \frac{1}{2}\phi_{\mathrm{TVD5}}\delta^-. \tag{26}$$

The resulting TENO schemes with this fifth-order limiter are referred to as TENO-M-TVD5.

3.2.2. Monotonicity-preserving limiter

Suresh and Huynh [20] propose a monotonicity-preserving method to bound the high-order reconstructed data at cell interface by distinguishing smooth local extrema from genuine discontinuity. The resulting monotonicity-preserving schemes allow for the local extremum to develop in the evaluation of cell interface data and is robust for shock-dominated flows. The minmod function with two arguments is

$$\text{minmod}(x, y) = \frac{1}{2}[\text{sgn}(x) + \text{sgn}(y)]\min(|x|, |y|), \tag{27}$$

and the minmod function with four arguments is

$$\text{minmod}(a, b, c, d) = \frac{1}{8}[\text{sgn}(a) + \text{sgn}(b)]|[\text{sgn}(a) + \text{sgn}(c)][\text{sgn}(a) + \text{sgn}(d)]|\min(|a|, |b|, |c|, |d|). \tag{28}$$

The median function is

$$\text{median}(x, y, z) = x + \text{minmod}(y - x, z - x). \tag{29}$$

While the curvature at the cell center i can be approximated by

$$d_i = f_{i+1} - 2f_i + f_{i-1}, \tag{30}$$

the curvature measurement at the cell interface $i + 1/2$ can be defined as

$$d_{i+1/2}^{\text{M4}} = \text{minmod}(4d_i - d_{i+1}, 4d_{i+1} - d_i, d_i, d_{i+1}). \tag{31}$$

This definition is more restrictive since the room for local extrema to develop is reduced when the ratio d_{i+1}/d_i is smaller than $1/4$ or larger than 4.

In order to define the minimum and maximum bounds of data at the interface $x_{i+1/2}$, the left-side upper limiter is given as

$$f_{i+1/2}^{\text{UL}} = f_i + \alpha(f_i - f_{i-1}), \tag{32}$$

where the choice of α in principle should satisfy the condition that $\text{CFL} \leq 1/(1 + \alpha)$ for stability. In our simulations, $\alpha = 1.25$ is employed to enable a choice of $\text{CFL} = 0.4$.

The median value of the solution at $x_{i+1/2}$ is given by

$$f_{i+1/2}^{\text{MD}} = \frac{1}{2}(f_i + f_{i+1}) - \frac{1}{2}d_{i+1/2}^{\text{MD}}. \tag{33}$$

The left-side value allowing for a large curvature in the solution at $x_{i+1/2}$ can be given by

$$f_{i+1/2}^{\text{LC}} = f_i + \frac{1}{2}(f_i - f_{i-1}) + \frac{\beta}{3}d_{i-1/2}^{\text{LC}}, \tag{34}$$

where it is recommended to set $\beta = 4$. Following [20] and [29], $d_{i+1/2}^{\text{MD}} = d_{i+1/2}^{\text{LC}} = d_{i+1/2}^{\text{M4}}$ is adopted. In numerical validations, the parameters in MP limiters are set as $d_{i+1/2} = d_{i+1/2}^{\text{M4}}$ and $\beta = 4$. The bounds are given by

$$\begin{aligned} f_{i+1/2}^{\text{L,min}} &= \max[\min(f_i, f_{i+1}, f_{i+1/2}^{\text{MD}}), \min(f_i, f_{i+1/2}^{\text{UL}}, f_{i+1/2}^{\text{LC}})], \\ f_{i+1/2}^{\text{L,max}} &= \min[\max(f_i, f_{i+1}, f_{i+1/2}^{\text{MD}}), \max(f_i, f_{i+1/2}^{\text{UL}}, f_{i+1/2}^{\text{LC}})], \end{aligned} \tag{35}$$

and the monotonicity preserving value for data at the interface $x_{i+1/2}$ is obtained by limiting the predicted value from other reconstructions as

$$f_{i+1/2}^{\text{MP}} = \text{median}(\widehat{f}_{i+1/2}, f_{i+1/2}^{\text{L,min}}, f_{i+1/2}^{\text{L,max}}). \tag{36}$$

This monotonicity-preserving limiter is implemented in the new framework through Eq. (20), and the resulting scheme is referred to as TENO-M-MP.

3.2.3. Implementation discussions

Within the TENO-M framework, the implementation of the MP limiter is slightly different from the TVD-type limiter. With a MP limiter, the minimum and maximum bounds of flux at the interface $x_{i+1/2}$ are first computed. Afterwards, these bounds are used to filter the candidate fluxes on the nonsmooth stencils identified by TENO, ensuring that the filtered nonsmooth flux is within the bounds computed by the MP limiter. In terms of the TVD-type limiters, a second-order (fifth-order) scheme with the Van Albada limiter (the TVD limiter) can be constructed based on the fixed three-cell (five-cell) stencil centered at i. Once a candidate stencil is identified as nonsmooth by the TENO weighting strategy, the nonsmooth flux will be replaced by the predefined second-order (fifth-order) flux. Both strategies yield flexible and controllable dissipation for the resulting TENO-M schemes.

Note that, in principle, the TVD-type limiter can also be applied to each identified nonsmooth candidate stencils and the filtering procedure will be similar to that of the MP limiter. The present choice, however, reduces the computational operations since only one limited flux is computed on fixed cells, and provides similar performance.

3.3. Full high-order construction

Since the candidate reconstructions are either smooth or filtered by nonlinear limiters, the high-order reconstruction at the cell interface $x_{i+1/2}$ can be achieved by a linear combination

$$\hat{f}_{i+1/2}^K = \sum_{k=0}^{K-3} w_k \hat{f}_{k,i+1/2}^M, \ k=0,\cdots,K-3, \tag{37}$$

where $w_k = d_k$, which denotes the optimal linear weights. A weight renormalization procedure as with the standard TENO paradigm, Eq. (18), is not needed. In practice, optimal weights d_k can either be optimized to approach the maximum accuracy order or to achieve better spectral properties with low dissipation and low dispersion.

3.4. Spectral property

The spectral properties of the nonlinear shock-capturing schemes, i.e. dissipation and dispersion property, can be analyzed by the approximate dispersion relation (ADR) [30]. As shown in Fig. 2, the numerical dissipation and dispersion of the newly proposed six- and eight-point TENO-M schemes are evaluated by computing the imaginary and real parts of the modified wavenumber. The dissipation and dispersion spectra of the standard WENO-CU6 [8], TENO6 [9], and TENO8A [17] schemes are also plotted for comparison.

It is observed that the good spectral resolutions of TENO6 and TENO8A are generally maintained by both TENO6-M and TENO8A-M schemes, which show remarkable improvements over the WENO-CU6 scheme. Both TENO and TENO-M schemes recover the dispersion and dissipation property of the background optimal linear schemes up to the wavenumber of about 1.5. The adjustment of nonlinear dissipation of TENO-M schemes are restricted to high-wavenumber regions. Owing to the flexibility of the present framework to choose nonlinear limiters, the dissipation property of TENO-M schemes in the high-wavenumber regions can be further manipulated by deploying different nonlinear limiters. For the limiters in the present paper, the low- and high-order TVD-type limiters provide more dissipation than the standard TENO schemes. As for the MP limiter, the numerical dissipation of TENO-M-MP schemes can be less than that of the counterpart TENO schemes in certain regions. These results demonstrate that with different choices of nonlinear limiters, the newly proposed framework conveys a broad range of nonlinear-dissipation variations in high wavenumber regions. By the proposed extension, TENO-M schemes can be tailored to handle different kinds of physical computations, such as shocks and turbulence, by a suitable choice of nonlinear limiter.

4. Numerical validations

In this section, a set of benchmark cases involving strong discontinuities and broadband flow scales is simulated. The proposed TENO-M schemes are extended to multi-dimensional problems in a dimension-by-dimension manner. For systems of hyperbolic conservation laws, the characteristic decomposition method based on the Roe average [31] is employed. The Rusanov scheme [32] is adopted for flux splitting. The third-order strong stability-preserving (SSP) Runge-Kutta method [33] with a typical CFL number of 0.4 is adopted for the time advancement. Numerical results from WENO-CU6 [8], TENO6 [9] and TENO8A [17] are compared. The parameters in TENO6 and TENO8A schemes are identical to those in [9] and [17].

4.1. Advection problems

4.1.1. Accuracy test

We first consider the one-dimensional Gaussian pulse advection problem [34]. The linear advection equation

$$\frac{\partial u}{\partial t} + \frac{\partial u}{\partial x} = 0, \tag{38}$$
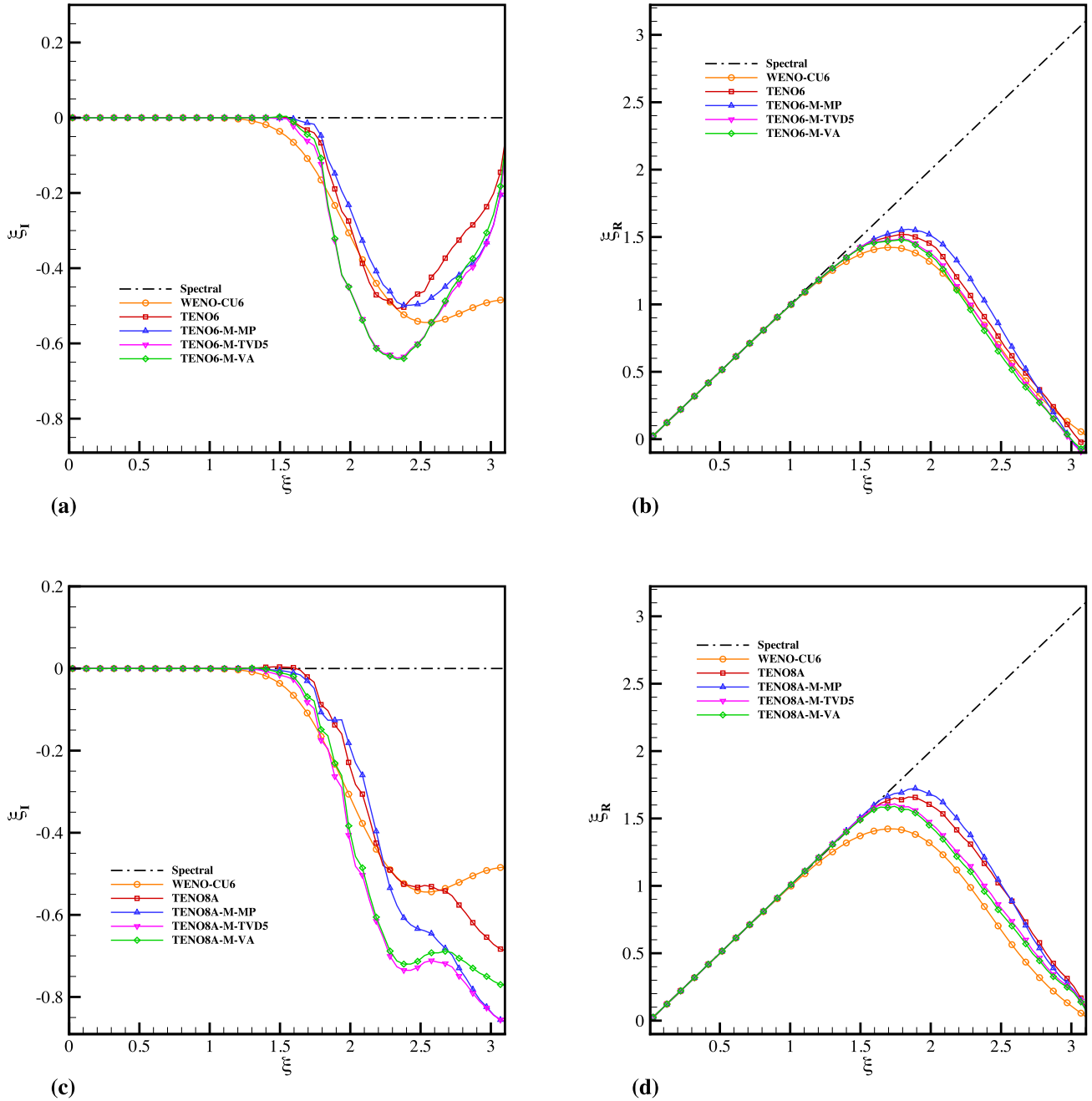
Fig. 2. Spectral properties. Top: dissipation (a) and dispersion (b) properties of the six-point TENO and TENO-M schemes; bottom: dissipation (c) and dispersion (d) properties of the eight-point TENO and TENO-M schemes.

with initial condition

$$u(x, 0) = e^{-300(x-x_c)^2}, \ x_c = 0.5, \tag{39}$$

is solved in a computational domain $0 \leq x \leq 1$ and the final time is $t = 1$. Periodic boundary conditions are imposed at $x = 0$ and $x = 1$.

As shown in Fig. 3, the desired accuracy order is achieved for both TENO6-M and TENO8A-M schemes. As all solutions are identified as smooth, optimal accuracy order is achieved.

4.1.2. Multi-wave advection

This case is taken from Jiang and Shu [2]. We solve the advection equation

$$\frac{\partial u}{\partial t} + \frac{\partial u}{\partial x} = 0, \tag{40}$$
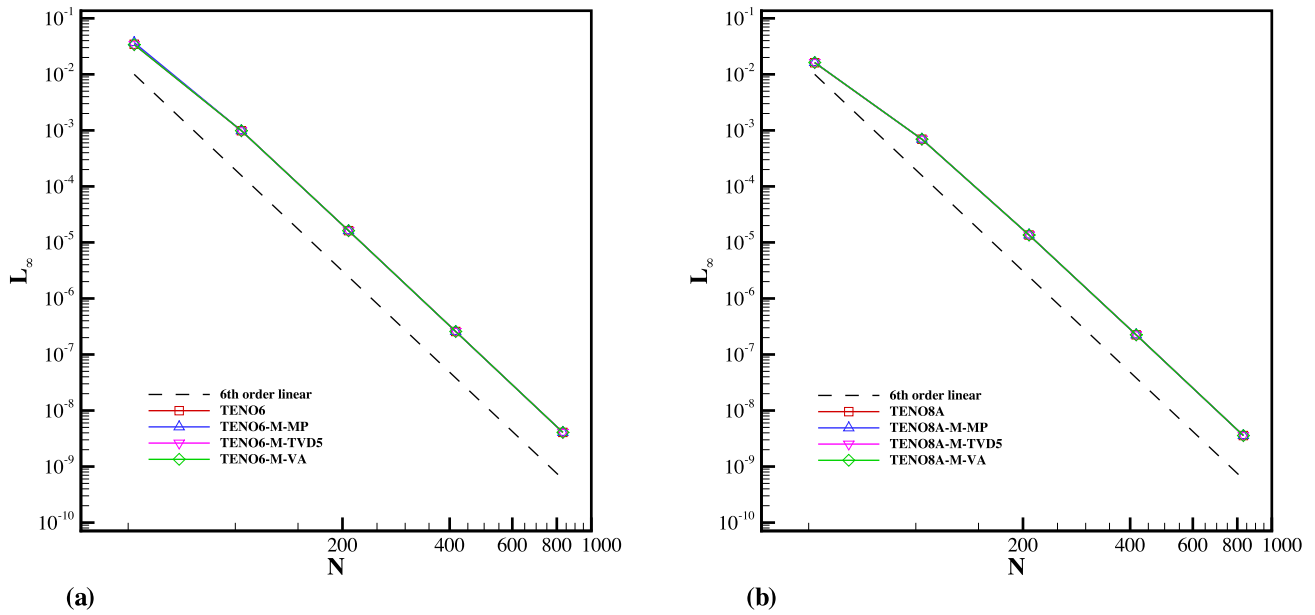
Fig. 3. Convergence of the L_∞ error from the TENO6-M (a) and TENO8A-M (b) schemes. N denotes the grid number.

with the initial condition

$$u(x,0) = \begin{cases} \frac{1}{6}[G(x-1,\beta,z-\theta) + G(x-1,\beta,z+\theta) + 4G(x-1,\beta,z)], & \text{if } 0.2 \le x < 0.4, \\ 1, & \text{if } 0.6 \le x \le 0.8, \\ 1 - |10(x-1.1)|, & \text{if } 1.0 \le x \le 1.2, \\ \frac{1}{6}[F(x-1,\alpha,a-\theta) + F(x-1,\alpha,a+\theta) + 4F(x-1,\alpha,a)], & \text{if } 1.4 \le x < 1.6, \\ 0, & \text{otherwise,} \end{cases} \tag{41}$$

where

$$G(x,\beta,z) = e^{-\beta(x-z)^2}, \qquad F(x,\alpha,a) = \sqrt{\max(1 - \alpha^2(x-a)^2, 0)}. \tag{42}$$

The parameters in Eqs. (41)–(42) are given as

$$a = 0.5, \; z = -0.7, \; \theta = 0.005, \; \alpha = 10, \; \beta = \frac{\log 2}{36\theta^2}. \tag{43}$$

The initial distribution consists of a Gaussian pulse, a square wave, a sharply peaked triangle and a half-ellipse arranged from left to right in the computational domain $x \in [0, 2]$. The computation is performed with $N = 200$ uniformly distributed mesh cells and the final simulation time is $t = 2$.

As shown in Fig. 4, for the advection of the square wave, all schemes are free from numerical oscillations. Concerning the advection of the half-ellipse wave, TENO-M schemes eliminate the overshoots generated by the standard TENO and WENO-CU6 schemes. Qualitatively, TENO-M-VA schemes exhibit best symmetry preservation.

4.2. Gas dynamics

4.2.1. Shock-tube problem

The Lax problem [35] and the Sod problem [36] are considered. The initial condition for Lax problem [35] is

$$(\rho, u, p) = \begin{cases} (0.445, 0.698, 3.528), & \text{if } 0 \le x < 0.5, \\ (0.5, 0, 0.5710), & \text{if } 0.5 \le x \le 1, \end{cases} \tag{44}$$

and the final simulation time is $t = 0.14$.

The initial condition for Sod problem [36] is

$$(\rho, u, p) = \begin{cases} (1, 0, 1), & \text{if } 0 \le x < 0.5, \\ (0.125, 0, 0.1), & \text{if } 0.5 \le x \le 1, \end{cases} \tag{45}$$

and the final simulation time is $t = 0.2$. The computations are done on 100 uniformly distributed grid points.
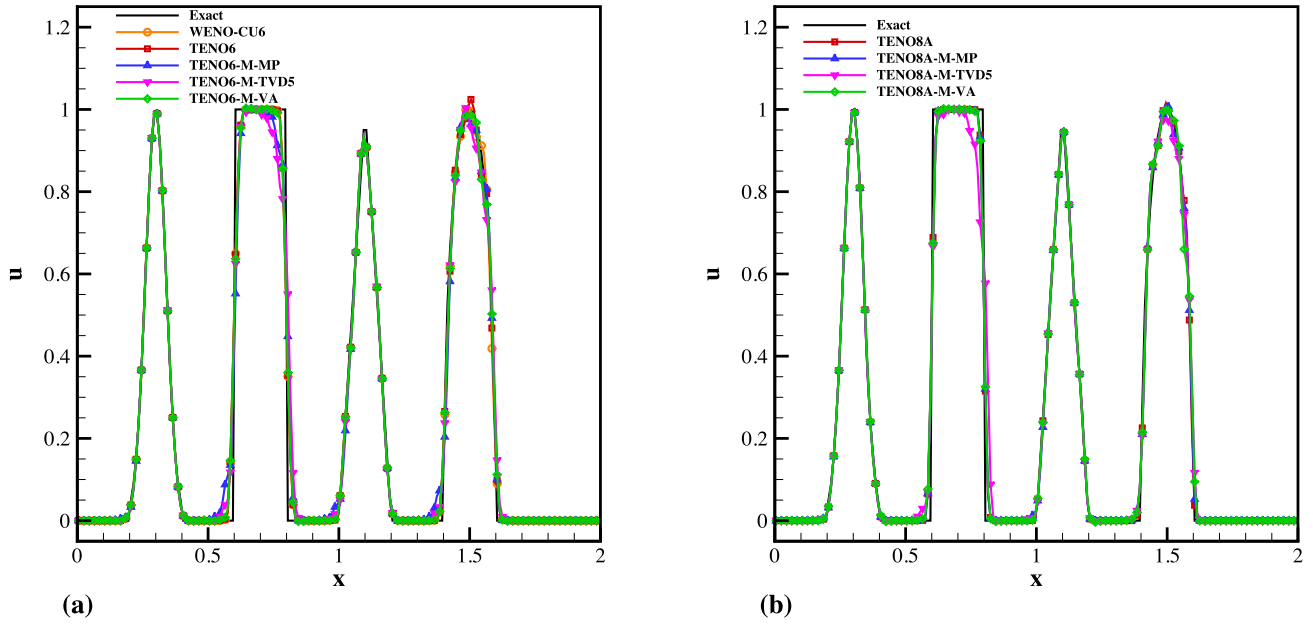
Fig. 4. Numerical results of advection of multi-wave with TENO6-M (a) and TENO8A-M (b) schemes. Discretization is on 200 uniformly distributed grid points.

As shown in Fig. 5 and Fig. 6, both the proposed TENO6-M and TENO8A-M schemes recover the shock-capturing capability of standard TENO schemes with the nonsmooth stencils being filtered by nonlinear limiters.

4.2.2. Shock density-wave interaction problem

This case is proposed by Shu and Osher [37]. A one-dimensional Mach-3 shock wave interacts with a perturbed density field generating both small-scale structures and discontinuities. The initial condition is

$$(\rho, u, p) = \begin{cases} (3.857, 2.629, 10.333), & \text{if } 0 \leq x < 1, \\ (1 + 0.2\sin(5(x-5)), 0, 1), & \text{if } 1 \leq x \leq 10. \end{cases} \tag{46}$$

The computational domain is [0,10] with $N = 200$ uniformly distributed mesh cells and the final evolution time is $t = 1.8$. The exact solution for reference is obtained by the fifth-order WENO-JS scheme with $N = 2000$.

Fig. 7 shows the computed density distributions from both six- and eight-point TENO-M schemes. It is observed that the proposed TENO6-M and TENO8A-M schemes resolve the high-wavenumber fluctuations with very low numerical dissipation while capturing the shocklets as sharply as the WENO-CU6 and standard TENO schemes. Among TENO-M schemes, the TENO-M-TVD5 and TENO-M-VA schemes provide slightly more dissipation than the standard TENO schemes in the under-resolved regions while the TENO-M-MP schemes are less dissipative with better wave-resolution property. By adapting the nonlinear limiters, the numerical dissipation in nonsmooth regions is tuned accordingly without sacrificing the shock-capturing capability and the high-order accuracy with this new TENO framework.

4.2.3. Interacting blast waves

The two-blast-waves interaction problem taken from [38] is considered. The initial condition is

$$(\rho, u, p) = \begin{cases} (1, 0, 1000), & \text{if } 0 \leq x < 0.1, \\ (1, 0, 0.01), & \text{if } 0.1 \leq x < 0.9, \\ (1, 0, 100), & \text{if } 0.9 \leq x \leq 1. \end{cases} \tag{47}$$

The simulation is performed on a uniform mesh with $N = 400$ and the final simulation time is $t = 0.038$. The exact solution for reference is computed by the fifth-order WENO-JS scheme on a uniform mesh with $N = 2500$. For this case the Roe scheme with entropy-fix is employed as numerical flux function.

As shown in Fig. 8, all schemes generate good results and the TENO6-M and TENO8A-M schemes perform better than WENO-CU6 in resolving the density peak at $x = 0.78$. In addition, TENO-M-MP schemes provide similar dissipation compared to the standard TENO schemes while TENO-M-TVD5 and TENO-M-VA schemes provide more dissipation, which confirms that a broad range of nonlinear-dissipation variations can be achieved through adopting different nonlinear limiters.
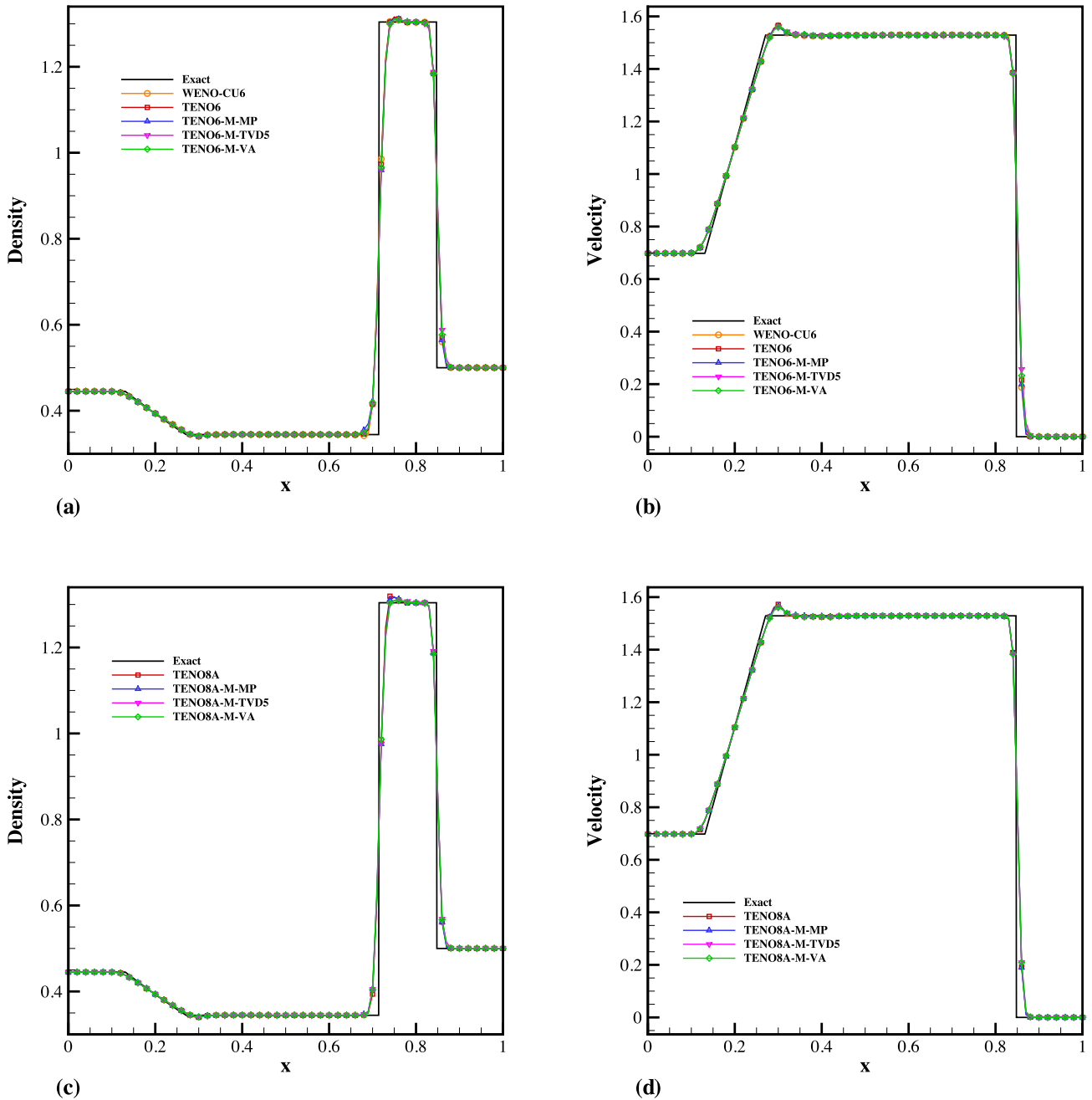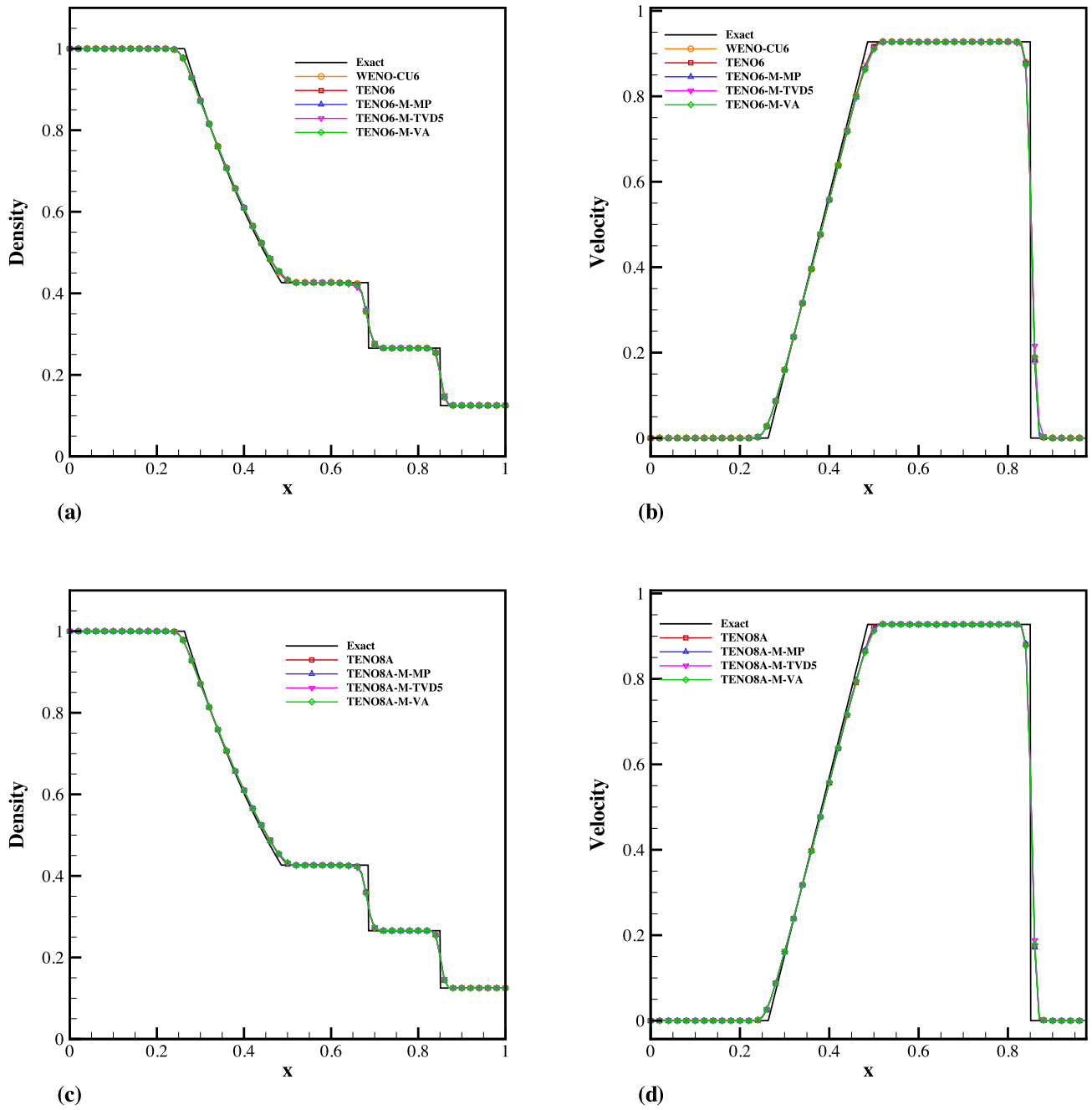
Fig. 5. Shock-tube problem: the Lax problem. Top: density profile (a) and velocity profile (b) of WENO-CU6, TENO6 and TENO6-M schemes; bottom: density profile (c) and velocity profile (d) of the TENO8A and TENO8A-M schemes. Discretization is on 100 uniformly distributed grid points and the final simulation time is $t = 0.14$.

4.2.4. Rayleigh-Taylor instability

The inviscid Rayleigh-Taylor instability case proposed by Xu and Shu [39] is considered here. The initial condition is

$$(\rho, u, v, p) = \begin{cases} (2, 0, -0.025c\cos(8\pi x), 1 + 2y), & \text{if } 0 \le y < 1/2, \\ (1, 0, -0.025c\cos(8\pi x), y + 3/2), & \text{if } 1/2 \le y \le 1, \end{cases} \tag{48}$$

where the sound speed $c = \sqrt{\gamma \frac{p}{\rho}}$ with $\gamma = \frac{5}{3}$. The computational domain is $[0, 0.25] \times [0, 1]$. Reflective boundary conditions are imposed at the left and right side of the domain. Constant primitive variables $(\rho, u, v, p) = (2, 0, 0, 1)$ and $(\rho, u, v, p) = (1, 0, 0, 2.5)$ are set for the bottom and top boundaries, respectively.

In Fig. 9, the computed density contours with the proposed TENO6-M and TENO8A-M schemes at resolution of 64×256 are shown. The results show that the newly proposed TENO6-M and TENO8A-M schemes resolve finer small-scale structures

Fig. 6. Shock-tube problem: the Sod problem. Top: density profile (a) and velocity profile (b) of WENO-CU6, TENO6 and TENO6-M schemes; bottom: density profile (c) and velocity profile (d) of TENO8A and TENO8A-M schemes. Discretization is on 100 uniformly distributed grid points and the final simulation time is $t = 0.2$.

than WENO-CU6 scheme. For all newly proposed schemes, the nonsmooth contact interface regions are captured sharply. In terms of vortex structures, TENO6-M-MP and TENO6-M-TVD5 schemes generate finer structures compared with TENO6-M-VA. While TENO6-M-MP exhibits breaking of flow symmetry, better symmetry preservation is visible for TENO6-M-VA. Similar observations can be seen for TENO8A and TENO8A-M.

4.2.5. Double Mach reflection of a strong shock

This two-dimensional case is taken from Woodward and Colella [38]. The initial condition is

$$(\rho, u, v, p) = \begin{cases} (1.4, 0, 0, 1), & \text{if } y < 1.732(x - 0.1667), \\ (8, 7.145, -4.125, 116.8333), & \text{otherwise.} \end{cases} \tag{49}$$
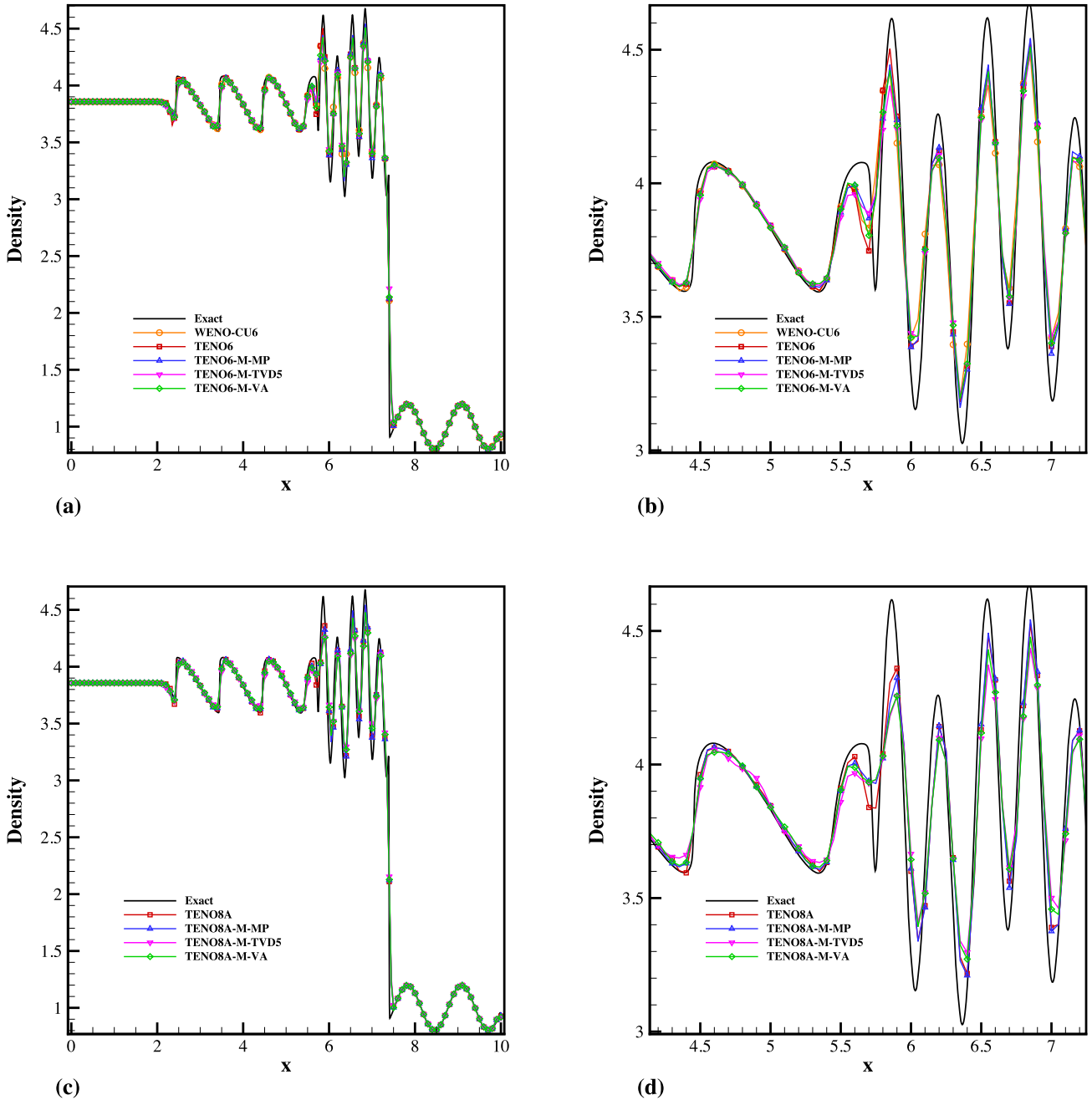
Fig. 7. Shock density-wave interaction problem: solutions from the WENO-CU6, TENO and TENO-M schemes. Top: density distribution (a) and a zoom-in view of the density distribution (b) of WENO-CU6, six-point TENO6 and TENO6-M schemes; bottom: density distribution (c) and a zoom-in view of the density distribution (d) of eight-point TENO8A and TENO8A-M schemes. Discretization is on 200 uniformly distributed grid points and the final simulation time is $t = 1.8$.

The computational domain is $[0, 4] \times [0, 1]$ and the final simulation time is $t = 0.2$. The boundary condition setup is the same as [38].

As shown in Fig. 10, Fig. 11 and Fig. 12, TENO and TENO-M schemes perform better than WENO-CU6 in resolving the small-scale structures. The shock-wave patterns are captured sharply without spurious numerical oscillations. Compared with the results of the TENO6-M-MP scheme, that of TENO6-M-TVD5 and TENO6-M-VA are slightly more dissipative.

Moreover, to address the flexibility of the unified framework, it is worth noting that the effect of the MP limiter can be adjusted through tuning of the curvature measurement $d_{i+1/2}^{M4}$ and β. In the following, we test the dissipation property of MP limiter with a smaller $\beta = 2$ and a less restrictive curvature measurement $d_{i+1/2}^{MM}$ at the cell interface $i + 1/2$ which is defined as

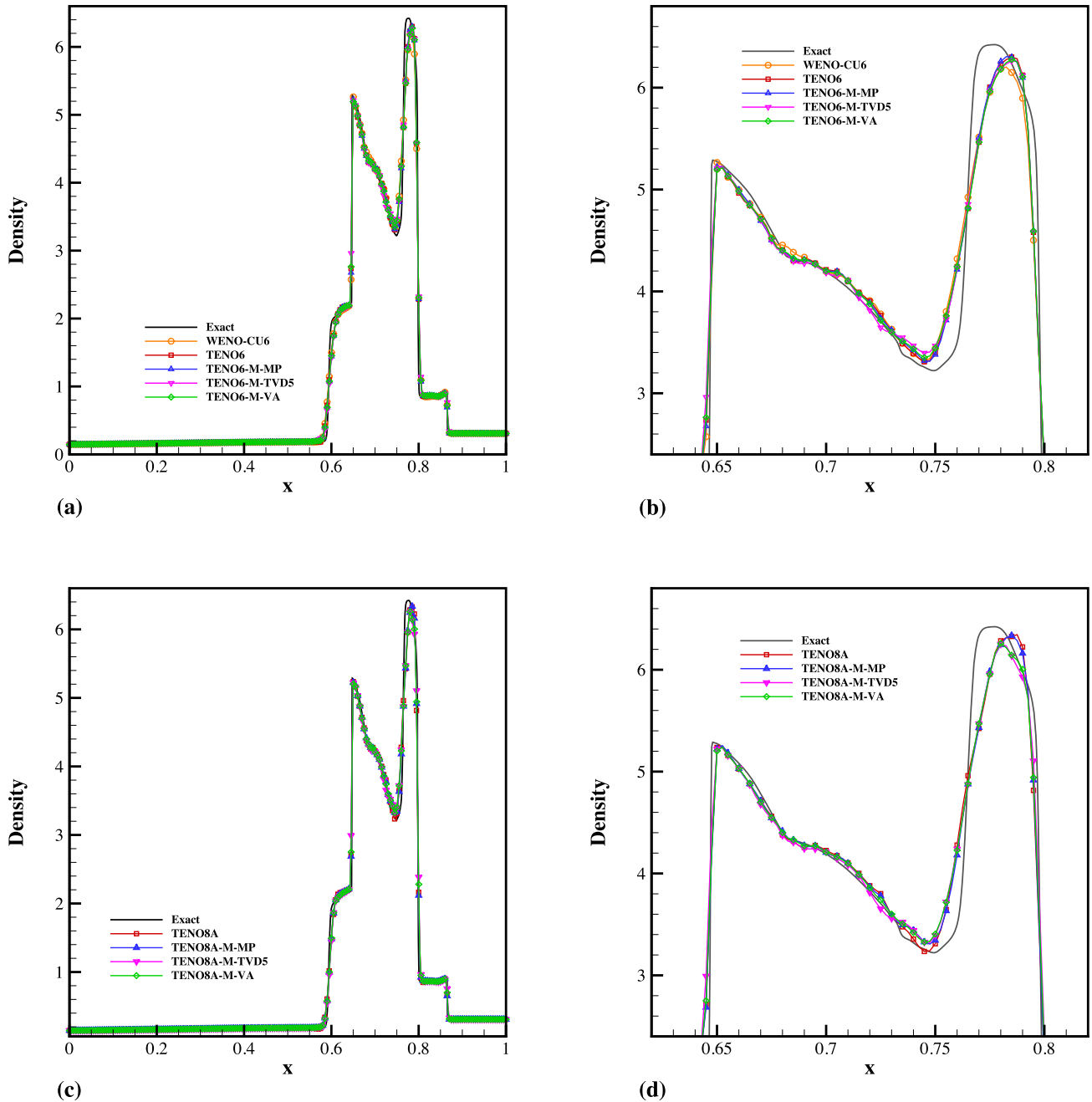$$d_{i+1/2}^{MM} = \text{minmod}(d_i, d_{i+1}). \tag{50}$$

Fig. 8. Interacting blast waves problem: solutions from the WENO-CU6, TENO and TENO-M schemes. Top: density distribution (a) and a zoom-in view of the density distribution (b) of WENO-CU6, six-point TENO and TENO-M schemes; bottom: density distribution (c) and a zoom-in view of the density distribution (d) of the eight-point TENO and TENO-M schemes. Discretization is on 400 uniformly distributed grid points and the final simulation time is $t = 0.038$.

As shown in Fig. 13, the dissipation property is more sensitive to β, which determines the amount of freedom allowing for large curvature. And Fig. 13 shows that, a more restrictive curvature measurement results in a less dissipative MP limiter.

We further perform simulations with a low-dissipation flux-splitting method and higher resolution. In Fig. 14 and Fig. 15, simulations with the resolution of $N = 1200 \times 300$ are performed on uniform meshes with TENO6 and TENO6-M schemes. Following Fleischmann et al. [40], to cure the grid-aligned shock instability in low-dissipation computations, the newly proposed Roe-M flux-splitting method is deployed to perform the simulations. With additional nonlinear limiters to filter the nonsmooth candidate stencils, TENO6-M-TVD5 and TENO6-M-VA can pass the case without difficulties. As shown in Fig. 15, TENO6-M schemes capture the shock-wave pattern sharply. In terms of the vortex structures, TENO6-M-TVD5 and TENO6-M-VA schemes generate these small scale structures with reduced numerical noise.
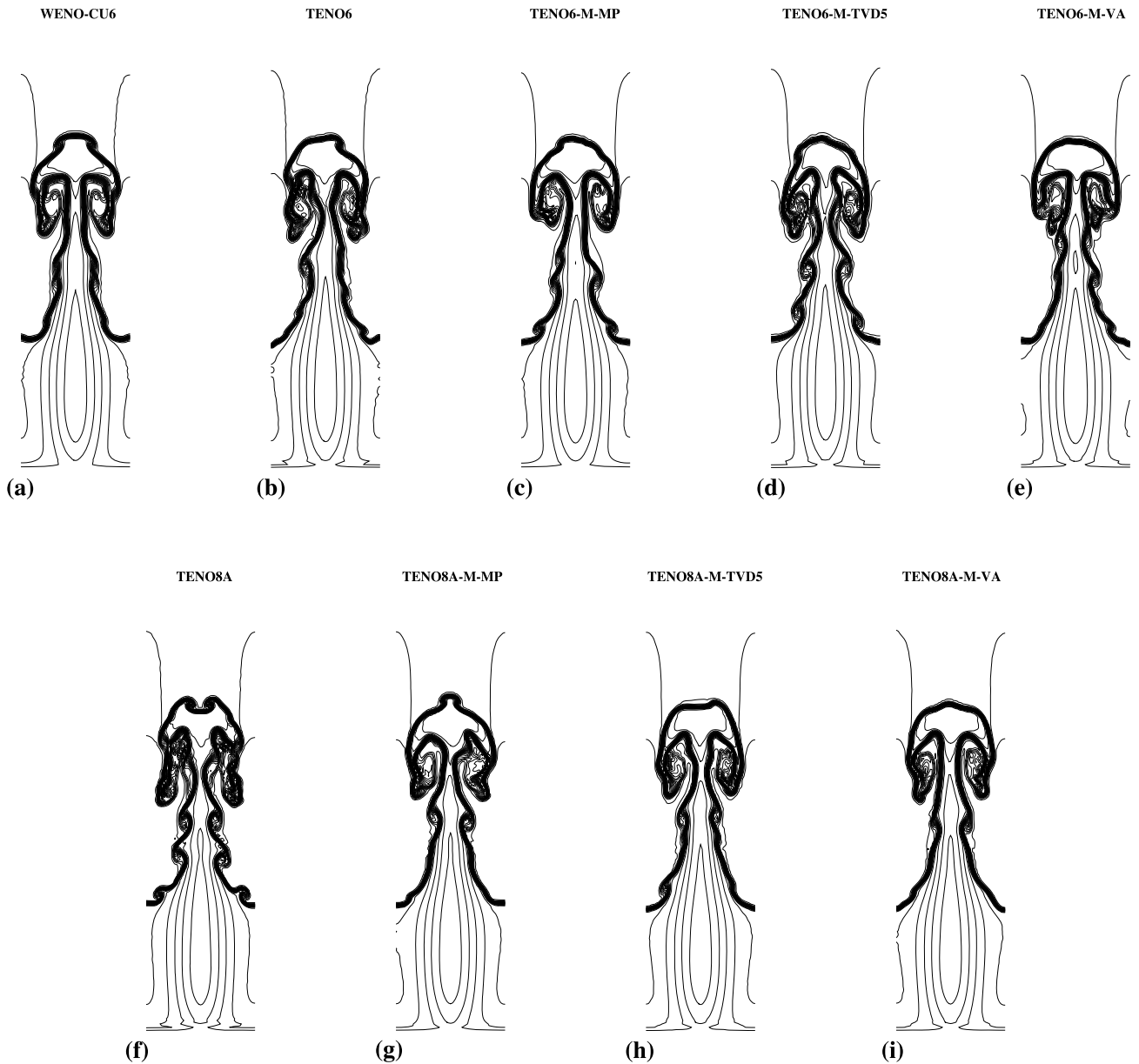
Fig. 9. Rayleigh-Taylor instability: density contours from the WENO-CU6 (a), TENO6 (b), TENO6-M (c)(d)(e), TENO8A (f) and TENO8A-M (g)(h)(i) schemes at simulation time $t = 1.95$. Resolution is 64×256. This figure is drawn with 25 density contours between 0.9 and 2.2.

4.3. Turbulent flows

4.3.1. Inviscid incompressible isotropic Taylor-Green vortex (TGV)

In order to assess the proposed TENO-M scheme for implicit large eddy simulations (ILES), we consider the typical incompressible isotropic Taylor-Green vortex case. The initial condition follows

$$
\begin{aligned}
u(x, y, z, 0) &= \sin(x)\cos(y)\cos(z) , \\
v(x, y, z, 0) &= \text{-}\cos(x)\sin(y)\cos(z), \\
w(x, y, z, 0) &= 0, \\
\rho(x, y, z, 0) &= 1.0, \\
p(x, y, z, 0) &= 100 + \frac{1}{16}[(\cos(2x)+\cos(2y))(2+\cos(2z)) - 2].
\end{aligned}
\tag{51}
$$

The computational domain is $[0, 2\pi] \times [0, 2\pi] \times [0, 2\pi]$ with periodic boundary conditions applied on the six boundaries. The mesh resolution is 64^3. The evolution of normalized total kinetic energy is shown in Fig. 16(a). The kinetic energy
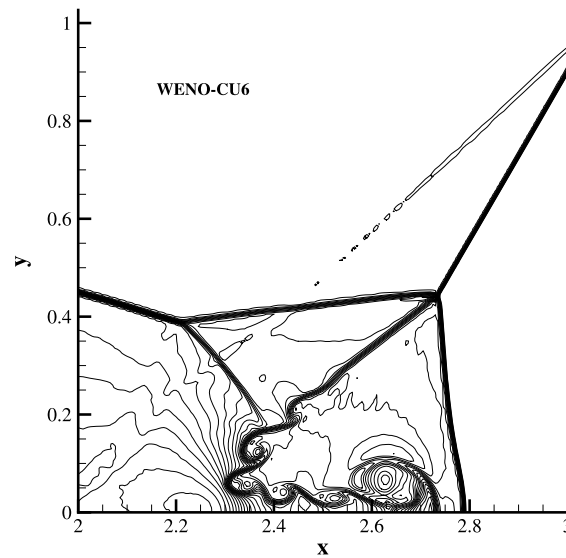
Fig. 10. Double Mach reflection of a strong shock: density contours from WENO-CU6 for reference at simulation time $t = 0.2$. Resolution is 800×200. This figure is drawn with 42 density contours between 3.27335 and 20.1335.

decays as $t^{-1.2}$, which agrees well with [41]. For very large Reynolds number incompressible TGV flows, three-dimensional statistically isotropic turbulence develops, and the kinetic-energy spectra $E(k) \propto k^{-5/3}$ is observed within the inertial sub-range after $t \simeq 9$. As shown in Fig. 16(b), although TENO8A-M is slightly more dissipative than TENO8A (for which the built-in parameters are particularly optimized for this case [17]) at high wavenumbers, it can faithfully reproduce the Kolmogorov scaling up to 2/3 of the cut-off wavenumber at $t = 10$. The present results suggest that TENO8-A-M scheme can be applied to under-resolved simulations without parameter tuning and has potential to function as an ILES model.

4.3.2. Viscous incompressible isotropic Taylor-Green vortex

With finite Reynolds numbers, the favorable numerical method is expected to reproduce the flow transition and the developed turbulence. Viscous incompressible isotropic case with a Reynolds number of 800 is computed with coarse resolutions of 64^3 and 96^3. Results from the implicit LES model ALDM [42] and the dynamic Smagorinsky model (DSGS) [43] are also provided for comparisons. As shown in Fig. 17, TENO8A-M-MP exhibits slightly higher dissipation than ALDM and TENO8A (both are optimized for this case [17][42]) at the time stage from $t = 5$ to $t = 8$ on the coarse mesh of 64^3. However, the result is better than that of the dynamic Smagorinsky model. With the finer mesh of 96^3, TENO8A-M-MP scheme shows good agreement with the DNS reference (computed on a mesh of 256^3 [44]) and predicts the peak dissipation rate at the later time stage very well. Therefore, TENO8A-M-MP can be applied as a physically-consistent ILES model without parameter tuning on coarse meshes.

4.4. Extreme simulations

In this part, we consider two challenging cases to demonstrate the advantage of the newly proposed framework. Following [45], the positivity-preserving flux limiter [46] is applied to guarantee positivity of pressure and density. With the present MP limiter, a less restrictive curvature parameter $d_{i+1/2}^{MM}$ and $\beta = 1$ are adopted to eliminate artificial local extrema generated by spurious oscillations.

4.4.1. Noh problem

The Noh problem [47] is a challenging case to test shock-capturing algorithms, where a uniform inwards radial inflow generates an infinitely strong shock wave moving outwards at a constant speed. The computational domain is $[0, 0.256] \times [0, 0.256] \times [0, 0.256]$ and the initial condition is described as $(\rho, u, v, w, p) = (1, -x/r, -y/r, -z/r, 1 \times 10^{-6})$. The final simulation time is 0.6 and the mesh resolution is 64^3.

As shown in Fig. 18, the position of the shock wave is well captured and the density distributions from TENO and TENO-M show good agreement with the exact solution. Unlike the density drop caused by wall over-heating at the center observed with WENO schemes, e.g. see Fig. 10 in [48], no artificial wall heating appears with the TENO and TENO-M schemes. Moreover, compared with the classical TENO schemes, TENO-M-TVD5 and TENO-M-MP show an improved suppression of spurious oscillations.
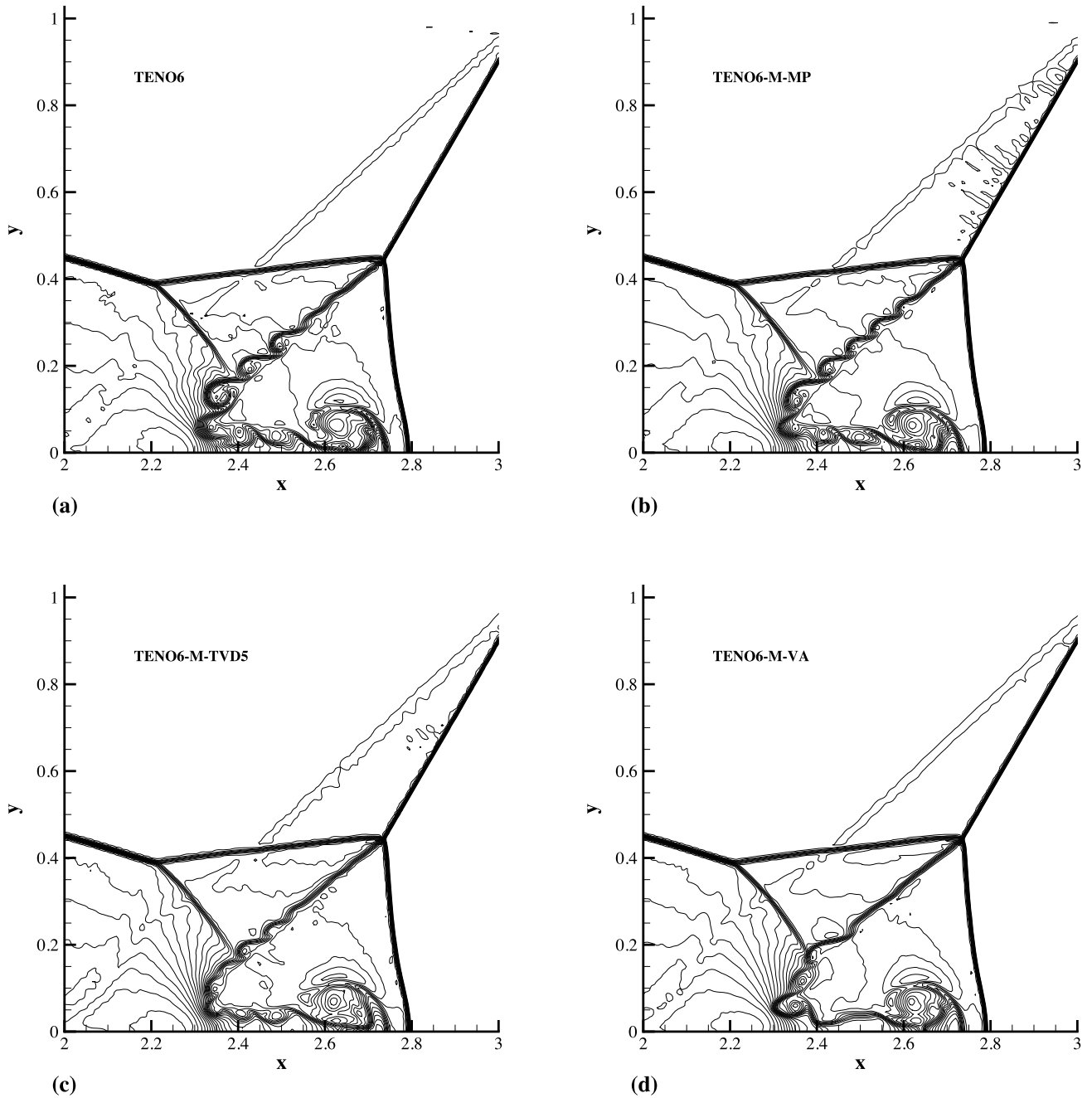
Fig. 11. Double Mach reflection of a strong shock: density contours from TENO6 (a) and TENO6-M schemes (b)(c)(d) at simulation time $t = 0.2$. Resolution is 800×200. This figure is drawn with 42 density contours between 3.27335 and 20.1335.

4.4.2. Le Blanc problem

The Le Blanc problem [49] is a challenging case with very strong discontinues. The initial condition is

$$
(\rho, u, p) = \begin{cases} (1, 0, \frac{2}{3} \times 10^{-1}), & \text{if } 0 \leq x < 3, \\ (10^{-3}, 0, \frac{2}{3} \times 10^{-10}), & \text{if } 3 \leq x \leq 9. \end{cases} \tag{52}
$$

The mesh resolution is $N = 900$ and the final simulation time is $t = 6$. The reference solutions are computed with the fifth-order WENO-JS scheme at a resolution $N = 2500$. The adiabatic coefficient is $\gamma = \frac{5}{3}$.

As shown in Fig. 19, the TENO8A scheme leads to obvious numerical oscillations in density and velocity profiles. For the density profile, TENO8A-M-MP eliminates the overshoot at $x = 6$ generated by the standard TENO8A scheme. In addition, TENO8A-M-MP preserves the monotonicity well in the velocity profile.
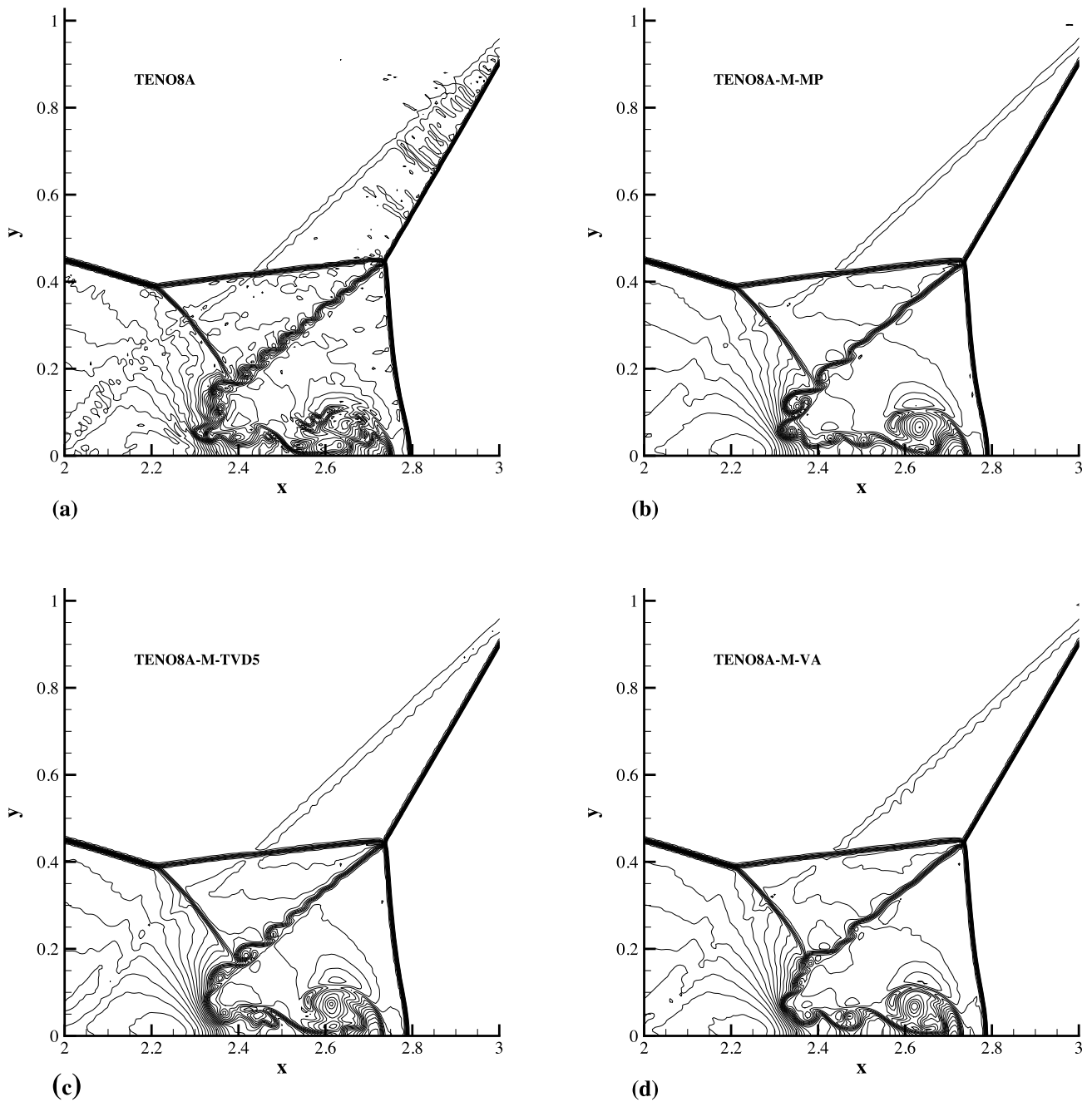
Fig. 12. Double Mach reflection of a strong shock: density contours from TENO8A (a) and TENO8A-M schemes (b)(c)(d) at simulation time $t = 0.2$. Resolution is 800×200. This figure is drawn with 42 density contours between 3.27335 and 20.1335.

4.5. Computational efficiency

In order to assess the computational efficiency of the proposed TENO-M scheme, we consider typical two-dimensional simulations, see Table 2. And the cases involved are the Rayleigh-Taylor instability with a resolution of 64×256 and the double Mach reflection of a strong shock with a resolution of 800×200 respectively. All simulations are conducted on the same desktop workstation. The results show that the cost of TENO8A-M scheme depends on the computational complexity of the limiters. For simple limiters, the computational efficiency of TENO8A-M can be even higher than that of TENO8A as the renormalization procedure of TENO is not needed. The TENO8A-M-MP scheme is slightly more expensive than the TENO8A scheme by about 10%. For TVD-type limiters (TVD5 and VA), the computational efficiency of TENO8A-M is almost the same as the classical TENO8A scheme. Regarding to the good performance and flexibility of the new framework, we believe that the proposed method is promising for a wide range of applications.
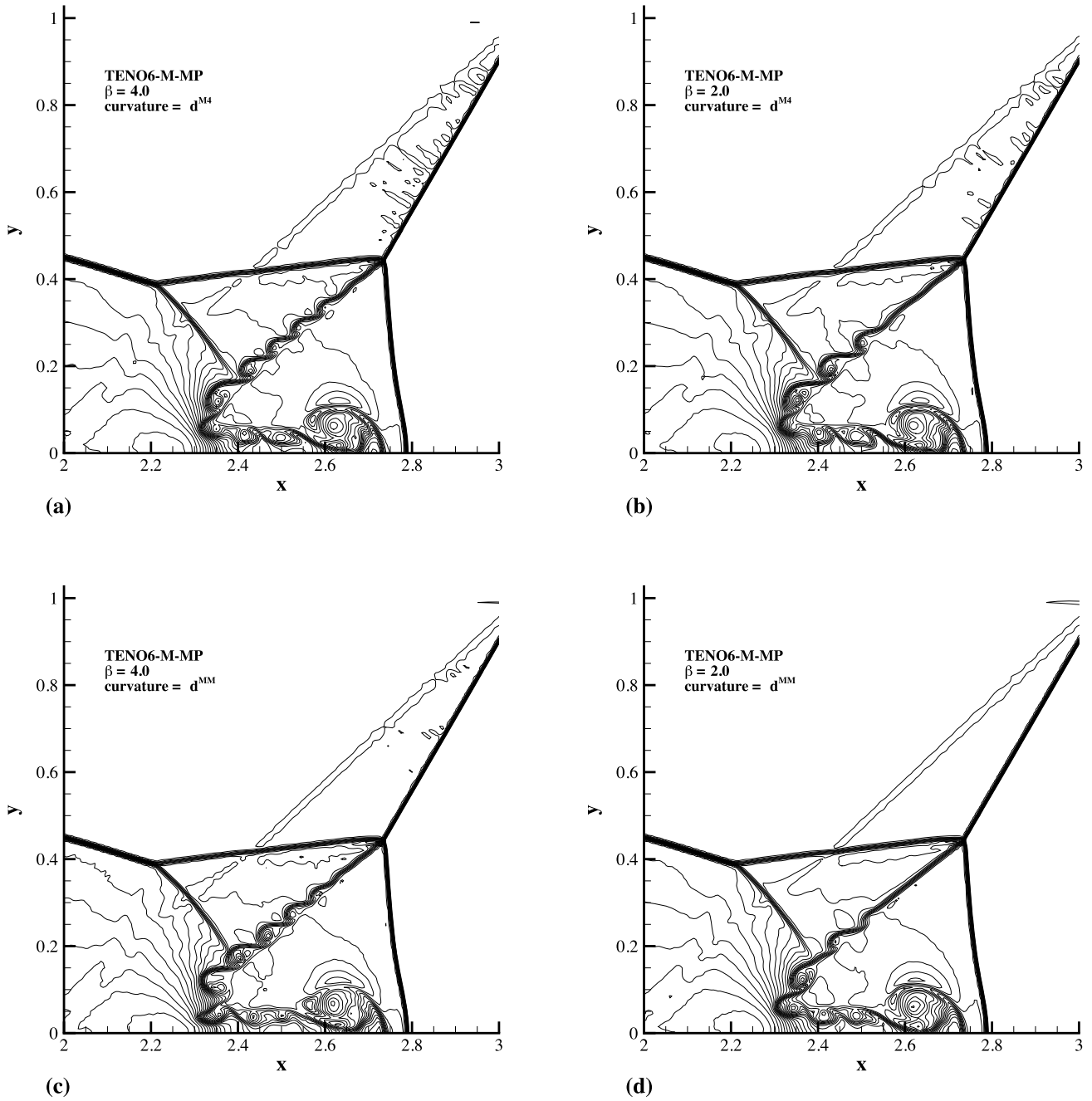
Fig. 13. Double Mach reflection of a strong shock: parameter study of monotonicity-preserving limiter. Density contours from TENO6-M-MP with d_{M4} curvature measurement and $\beta = 4.0$ (a), TENO6-M-MP with d_{M4} curvature measurement and $\beta = 2.0$ (b), TENO6-M-MP with d_{MM} curvature measurement and $\beta = 4.0$ (c) and TENO6-M-MP with d_{MM} curvature measurement and $\beta = 2.0$ (d) at simulation time $t = 0.2$. Resolution is 800×200. This figure is drawn with 42 density contours between 3.27335 and 20.1335.

5. Conclusions

In this paper a flexible framework for constructing new shock-capturing TENO schemes is proposed. Six- and eight-point TENO-M schemes are developed, and their performance is demonstrated by conducting a set of critical benchmark cases. The conclusions are as follows.

- The new framework establishes a unified concept of TENO schemes with classical nonlinear limiters for shock-capturing. Three stages are involved, (a) evaluating of candidate numerical fluxes and labeling each candidate stencil as smooth or nonsmooth by a ENO-like stencil selection procedure; (b) filtering the nonsmooth candidate stencils by an extra
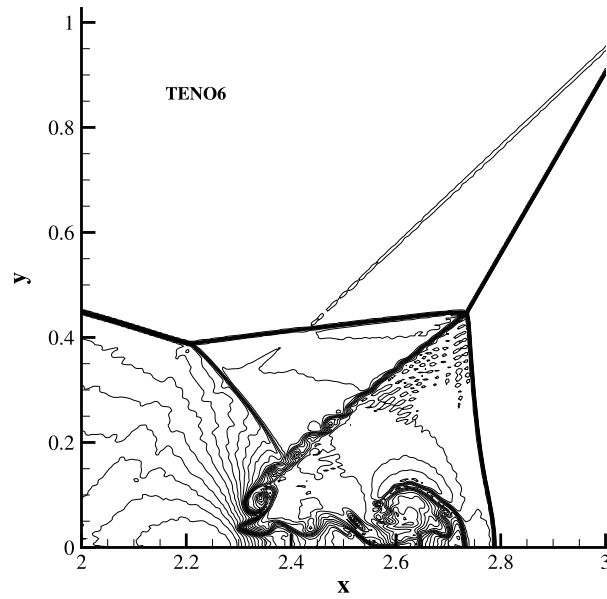
Fig. 14. Double Mach reflection of a strong shock: density contours from TENO6 at simulation time $t = 0.2$. Resolution of 1200×300. This figure is drawn with 42 density contours between 3.27335 and 20.1335.

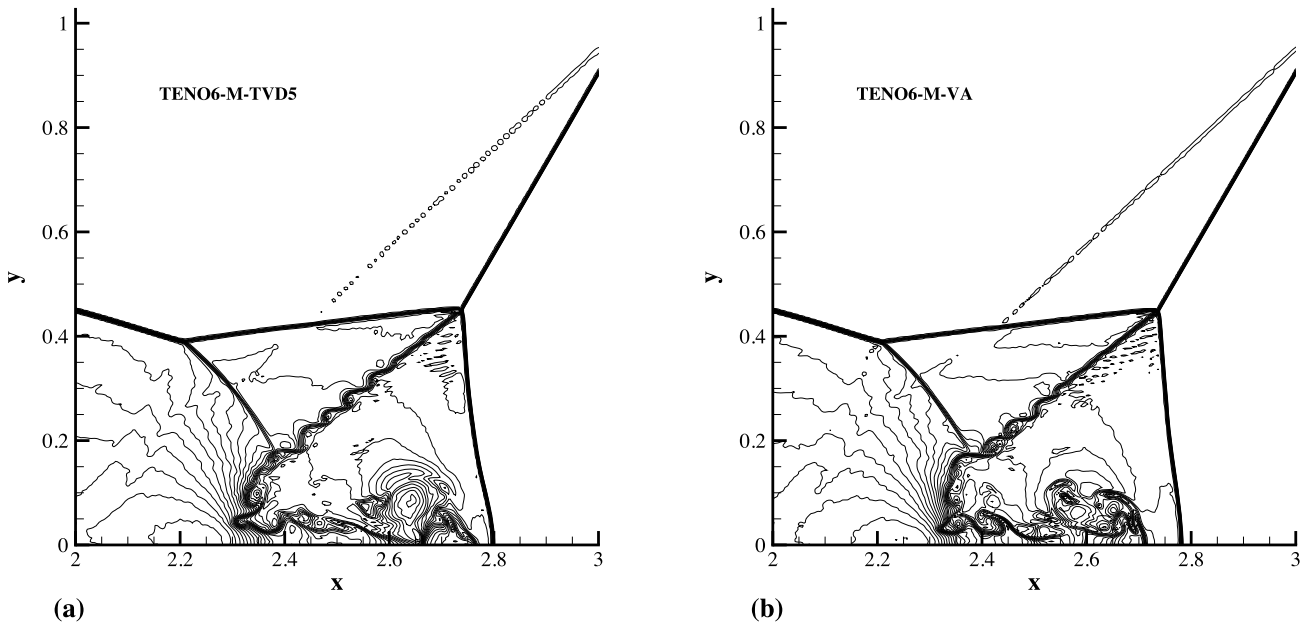**(a)**   **(b)**

Fig. 15. Double Mach reflection of a strong shock: density contours from TENO6-M schemes: TENO6-M-TVD5 (a) and TENO6-M-VA (b) at simulation time $t = 0.2$. TENO6-M-MP fails to pass. Resolution of 1200×300. This figure is drawn with 42 density contours between 3.27335 and 20.1335.

Table 2
The averaged computational time (in the parentheses) and the normalized values with respect to the computational time of TENO8A.

Case	Grid number	TENO8A	TENO8A-MP	TENO8A-TVD5	TENO8A-VA
Rayleigh-Taylor instability	64×256	1(228.44 s)	1.088(248.58 s)	0.988(225.72 s)	0.997(227.89 s)
Double Mach reflection of a strong shock	800×200	1(1153.49 s)	1.123(1295.31 s)	0.985(1137.11 s)	0.993(1145.91 s)

nonlinear limiter; (c) formulating the high-order reconstruction by combining the candidate stencils with optimal linear weights.
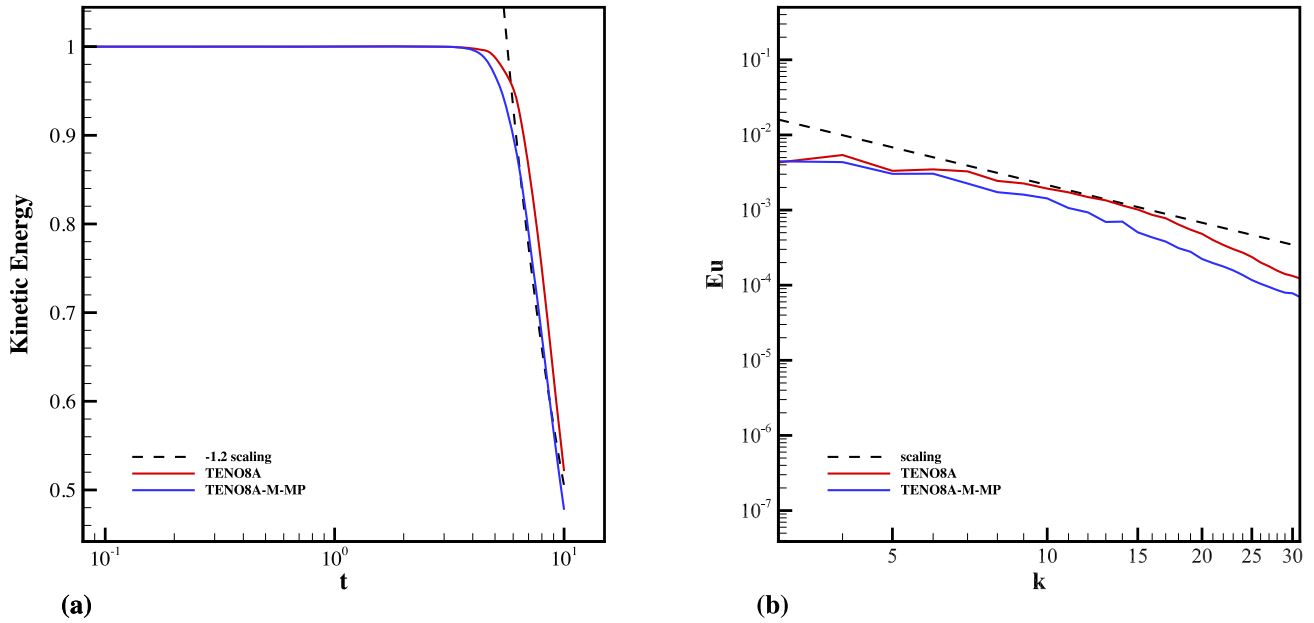
Fig. 16. Inviscid Taylor-Green vortex problem: solutions from the TENO8A and TENO8A-M schemes. The evolution of normalized total kinetic energy (a) and the energy spectrum within resolved inertial subrange at t = 10 compared to the Kolmogorov scaling $E(k) \propto k^{-5/3}$ (b). Discretization is on 64^3 uniformly distributed grid points. (For interpretation of the colors in the figure(s), the reader is referred to the web version of this article.)
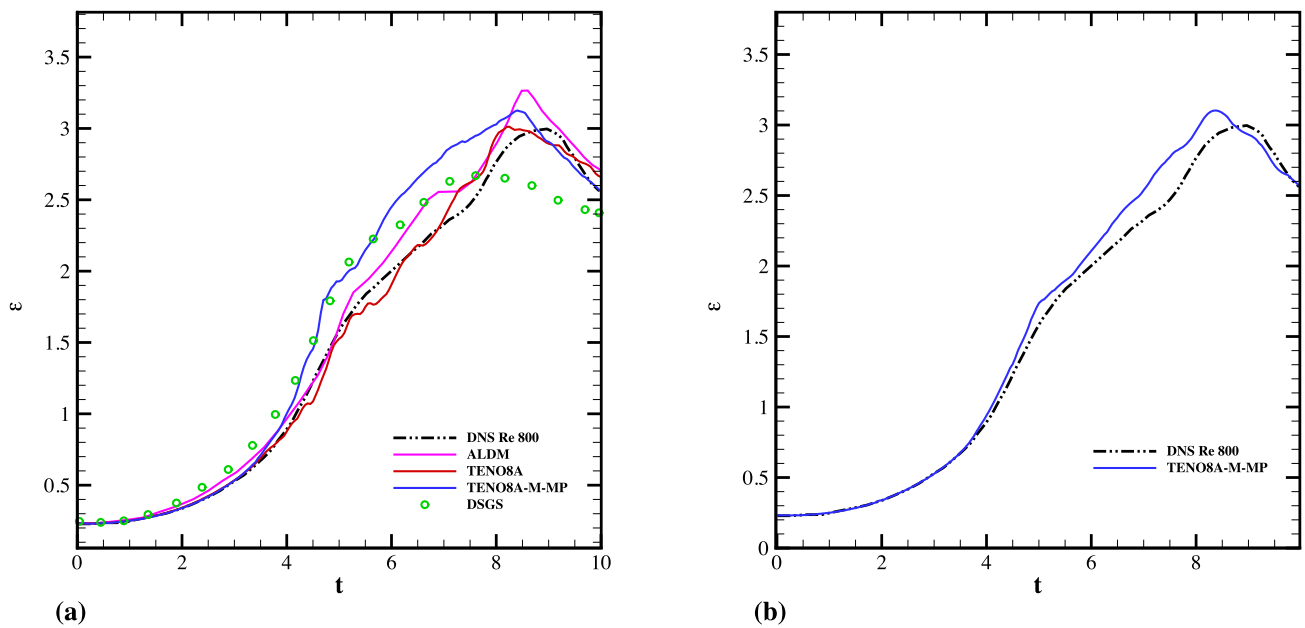

Fig. 17. Taylor-Green vortex problem with Reynolds number 800: comparison of energy dissipation rate. Left: comparison on a 64^3 mesh (a). Right: comparison on a 96^3 mesh (b). (For interpretation of the colors in the figure(s), the reader is referred to the web version of this article.)

- In smooth regions, all candidate stencils are identified as smooth by the TENO stencil selection procedure and consequently TENO-M recovers to TENO. In nonsmooth regions, stable shock-capturing capability is achieved since the nonsmooth candidates contributed to the final reconstructions are filtered to be oscillation-free by extra limiters.
- The present framework can be applied to a wide range of limiters, such as TVD and MP. Such different nonlinear limiters are deployed straightforwardly to construct a new family of high-order TENO-M schemes. TENO-M schemes enable flexible control of dissipation in nonsmooth regions. A wide range of adjustable nonlinear dissipation can be considered in the current framework without affecting global dissipation and detriment to accuracy in low-wavenumber regions.
- A set of critical benchmark cases is simulated. Numerical results demonstrate the capability of the new schemes in terms of recovering high-order accuracy in smooth regions, preserving low dissipation for resolution of fluctuations, and sharp capturing of discontinuities (eliminating spurious oscillations particularly in extreme cases). Moreover, different
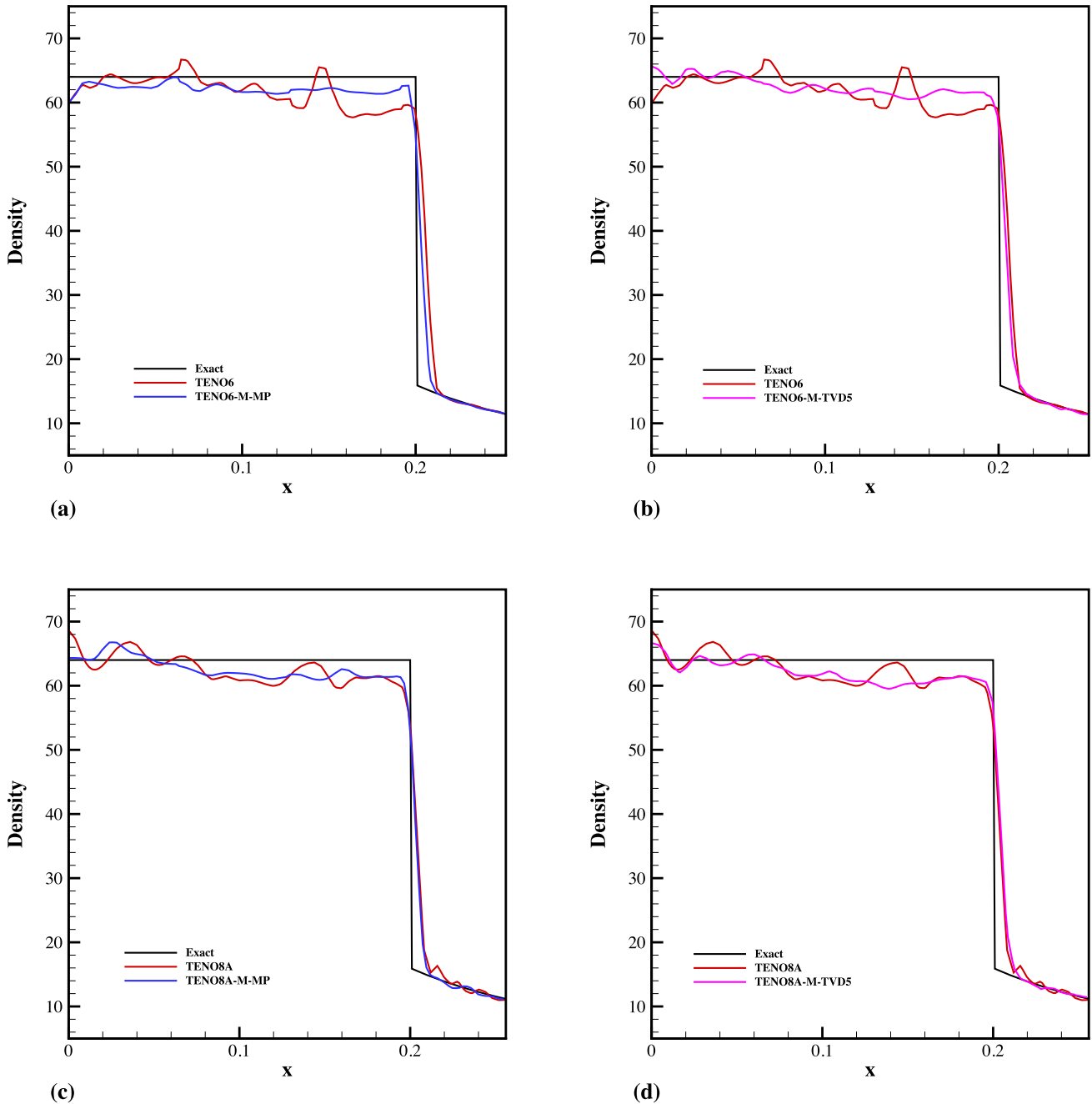
Fig. 18. Noh problem: solutions from the TENO and TENO-M schemes. Top: density distribution (a, b) of six-point TENO6 and TENO6-M schemes; bottom: density distribution (c, d) of eight-point TENO8A and TENO8A-M schemes. Discretization is on $64 \times 64 \times 64$ uniformly distributed grid points and the final simulation time is $t = 0.6$. (For interpretation of the colors in the figure(s), the reader is referred to the web version of this article.)

nonlinear limiters are tested. The results show that adapting nonlinear numerical dissipation in nonsmooth regions can be controlled by the choice of limiter function.

CRediT authorship contribution statement

Yue Li: Conceptualization, Methodology, Software, Writing - original draft. **Lin Fu:** Conceptualization, Methodology, Software, Writing - original draft. **Nikolaus A. Adams:** Conceptualization, Methodology, Supervision, Writing - review & editing.

Declaration of competing interest

The authors declare that they have no known competing financial interests or personal relationships that could have appeared to influence the work reported in this paper.
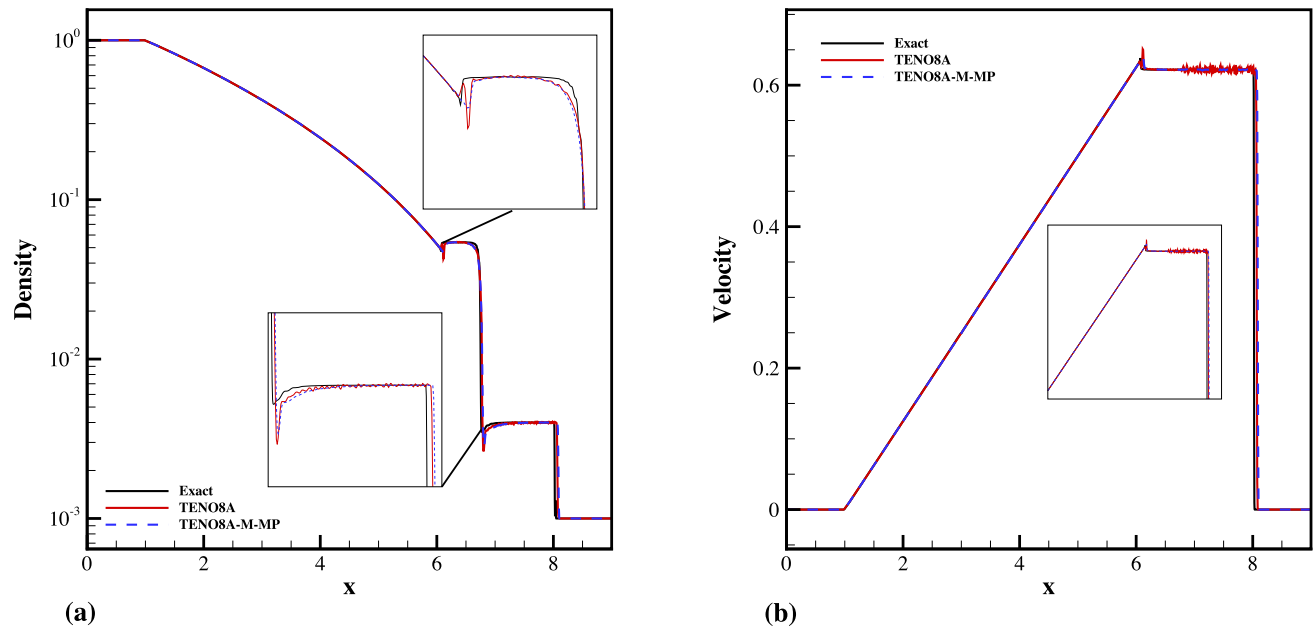
Fig. 19. Le Blanc problem: solutions from the TENO and TENO-M schemes. Density distribution (a) and velocity distribution (b) of eight-point TENO8A and TENO8A-M schemes. Discretization is on 900 uniformly distributed grid points and the final simulation time is $t = 6$. (For interpretation of the colors in the figure(s), the reader is referred to the web version of this article.)

Acknowledgements

References

[1] X.D. Liu, S. Osher, T. Chan, Weighted essentially non-oscillatory schemes, J. Comput. Phys. 115 (1994) 200–212.
[2] G.S. Jiang, C.-W. Shu, Efficient implementation of weighted ENO schemes, J. Comput. Phys. 126 (1) (1996) 202–228.
[3] A. Harten, B. Engquist, S. Osher, S.R. Chakravarthy, Uniformly high order accurate essentially non-oscillatory schemes, III, in: Upwind and High-Resolution Schemes, Springer, 1987, pp. 218–290.
[4] A.K. Henrick, T.D. Aslam, J.M. Powers, Mapped weighted essentially non-oscillatory schemes: achieving optimal order near critical points, J. Comput. Phys. 207 (2) (2005) 542–567.
[5] R. Borges, M. Carmona, B. Costa, W.S. Don, An improved weighted essentially non-oscillatory scheme for hyperbolic conservation laws, J. Comput. Phys. 227 (6) (2008) 3191–3211.
[6] D.J. Hill, D.I. Pullin, Hybrid tuned center-difference-WENO method for large eddy simulations in the presence of strong shocks, J. Comput. Phys. 194 (2) (2004) 435–450.
[7] M.P. Martín, E.M. Taylor, M. Wu, V.G. Weirs, A bandwidth-optimized WENO scheme for the effective direct numerical simulation of compressible turbulence, J. Comput. Phys. 220 (1) (2006) 270–289.
[8] X.Y. Hu, Q. Wang, N.A. Adams, An adaptive central-upwind weighted essentially non-oscillatory scheme, J. Comput. Phys. 229 (2010) 8952–8965.
[9] L. Fu, X.Y. Hu, N.A. Adams, A family of high-order targeted ENO schemes for compressible-fluid simulations, J. Comput. Phys. 305 (2016) 333–359.
[10] L. Fu, X.Y. Hu, N.A. Adams, Targeted ENO schemes with tailored resolution property for hyperbolic conservation laws, J. Comput. Phys. 349 (2017) 97–121.
[11] L. Fu, X.Y. Hu, N.A. Adams, A new class of adaptive high-order targeted ENO schemes for hyperbolic conservation laws, J. Comput. Phys. 374 (2018) 724–751.
[12] L. Fu, A low-dissipation finite-volume method based on a new TENO shock-capturing scheme, Comput. Phys. Commun. 235 (2019) 25–39.
[13] N.A. Adams, K. Shariff, A high-resolution hybrid compact-ENO scheme for shock-turbulence interaction problems, J. Comput. Phys. 127 (1) (1996) 27–51.
[14] S. Pirozzoli, Conservative hybrid compact-WENO schemes for shock-turbulence interaction, J. Comput. Phys. 178 (1) (2002) 81–117.
[15] X. Hu, B. Wang, N.A. Adams, An efficient low-dissipation hybrid weighted essentially non-oscillatory scheme, J. Comput. Phys. 301 (2015) 415–424.
[16] L. Fu, A hybrid method with TENO based discontinuity indicator for hyperbolic conservation laws, Commun. Comput. Phys. (ISSN 1991-7120) 26 (4) (2019) 973–1007.
[17] L. Fu, X. Hu, N.A. Adams, A targeted ENO scheme as implicit model for turbulent and genuine subgrid scales, Commun. Comput. Phys. 26 (2019) 311–345.
[18] L. Fu, X.Y. Hu, N.A. Adams, Improved five- and six-point targeted essentially non-oscillatory schemes with adaptive dissipation, AIAA J. 57 (3) (2018) 1143–1158.
[19] Y.-X. Ren, H. Zhang, et al., A characteristic-wise hybrid compact-WENO scheme for solving hyperbolic conservation laws, J. Comput. Phys. 192 (2) (2003) 365–386.
[20] A. Suresh, H. Huynh, Accurate monotonicity preserving schemes with Runge–Kutta time stepping, J. Comput. Phys. 136 (1) (1997) 83–99.
[21] K.H. Kim, C. Kim, Accurate, efficient and monotonic numerical methods for multi-dimensional compressible flows: part II: multi-dimensional limiting process, J. Comput. Phys. 208 (2) (2005) 570–615.
[22] A. Harten, High resolution schemes for hyperbolic conservation laws, J. Comput. Phys. 49 (3) (1983) 357–393.

[23] P.K. Sweby, High resolution schemes using flux limiters for hyperbolic conservation laws, SIAM J. Numer. Anal. 21 (5) (1984) 995–1011.

[24] B. Van Leer, Towards the ultimate conservative difference scheme. V. A second-order sequel to Godunov's method, J. Comput. Phys. 32 (1) (1979) 101–136.

[25] D. Zhang, C. Jiang, L. Cheng, D. Liang, A refined r-factor algorithm for TVD schemes on arbitrary unstructured meshes, Int. J. Numer. Methods Fluids 80 (2) (2016) 105–139.

[26] F. Kemm, A comparative study of TVD-limiters – well-known limiters and an introduction of new ones, Int. J. Numer. Methods Fluids 67 (4) (2011) 404–440.

[27] M. Arora, P.L. Roe, A well-behaved TVD limiter for high-resolution calculations of unsteady flow, J. Comput. Phys. 132 (1) (1997) 3–11.

[28] G. Van Albada, B. Van Leer, W. Roberts, A comparative study of computational methods in cosmic gas dynamics, in: Upwind and High-Resolution Schemes, Springer, 1997, pp. 95–103.

[29] D.S. Balsara, C.-W. Shu, Monotonicity preserving weighted essentially non-oscillatory schemes with increasingly high order of accuracy, J. Comput. Phys. 160 (2) (2000) 405–452.

[30] S. Pirozzoli, On the spectral properties of shock-capturing schemes, J. Comput. Phys. 219 (2) (2006) 489–497.

[31] P.L. Roe, Approximate Riemann solvers, parameter vectors, and difference schemes, J. Comput. Phys. 43 (2) (1981) 357–372.

[32] V.V. Rusanov, Calculation of interaction of non-steady shock waves with obstacles, USSR J. Comp. Math. Phys. (1961) 267–279.

[33] S. Gottlieb, C.-W. Shu, E. Tadmor, Strong stability-preserving high-order time discretization methods, SIAM Rev. 43 (1) (2001) 89–112.

[34] N.K. Yamaleev, M.H. Carpenter, A systematic methodology for constructing high-order energy stable WENO schemes, J. Comput. Phys. 228 (11) (2009) 4248–4272.

[35] P.D. Lax, Weak solutions of nonlinear hyperbolic equations and their numerical computation, Commun. Pure Appl. Math. 7 (1954) 159–193.

[36] G.A. Sod, A survey of several finite difference methods for systems of nonlinear hyperbolic conservation laws, J. Comput. Phys. 27 (1978) 1–31.

[37] C.W. Shu, S. Osher, Efficient implementation of essentially non-oscillatory shock-capturing schemes, II, J. Comput. Phys. 83 (1989) 32–78.

[38] P. Woodward, The numerical simulation of two-dimensional fluid flow with strong shocks, J. Comput. Phys. 54 (1984) 115–173.

[39] Z. Xu, C.W. Shu, Anti-diffusive flux corrections for high order finite difference WENO schemes, J. Comput. Phys. 205 (2005) 458–485.

[40] N. Fleischmann, S. Adami, X.Y. Hu, N.A. Adams, A low dissipation method to cure the grid-aligned shock instability, J. Comput. Phys. (2019) 109004.

[41] M. Lesieur, S. Ossia, 3D isotropic turbulence at very high Reynolds numbers: EDQNM study, J. Turbul. 1 (1) (2000) 007.

[42] S. Hickel, N.A. Adams, J.A. Domaradzki, An adaptive local deconvolution method for implicit LES, J. Comput. Phys. 213 (1) (2006) 413–436.

[43] M. Germano, U. Piomelli, P. Moin, W.H. Cabot, A dynamic subgrid-scale eddy viscosity model, Phys. Fluids A, Fluid Dyn. 3 (7) (1991) 1760–1765.

[44] M.E. Brachet, D.I. Meiron, S.A. Orszag, B. Nickel, R.H. Morf, U. Frisch, Small-scale structure of the Taylor–Green vortex, J. Fluid Mech. 130 (1983) 411–452.

[45] L. Fu, A very-high-order TENO scheme for all-speed gas dynamics and turbulence, Comput. Phys. Commun. 244 (2019) 117–131.

[46] X.Y. Hu, N.A. Adams, C.-W. Shu, Positivity-preserving method for high-order conservative schemes solving compressible Euler equations, J. Comput. Phys. 242 (2013) 169–180.

[47] W.F. Noh, Errors for calculations of strong shocks using an artificial viscosity and an artificial heat flux, J. Comput. Phys. 72 (1) (1987) 78–120.

[48] E. Johnsen, J. Larsson, A.V. Bhagatwala, W.H. Cabot, P. Moin, B.J. Olson, P.S. Rawat, S.K. Shankar, B. Sjögreen, H.C. Yee, et al., Assessment of high-resolution methods for numerical simulations of compressible turbulence with shock waves, J. Comput. Phys. 229 (4) (2010) 1213–1237.

[49] R. Loubère, M.J. Shashkov, A subcell remapping method on staggered polygonal grids for arbitrary-Lagrangian–Eulerian methods, J. Comput. Phys. 209 (1) (2005) 105–138.

A.2 Paper II

Yue Li, Lin Fu, Nikolaus A. Adams

A family of fast multi-resolution ENO schemes for compressible flows

Contribution: My contribution to this work was the development of the method and the corresponding computer code for its implementation. I performed simulations and analyzed the results, and wrote the manuscript for the publication.

A Family of Fast Multi-resolution ENO Schemes for Compressible Flows

Yue Li[1] · Lin Fu[2,3,4,5] · Nikolaus A. Adams[1]

Abstract

In this paper, a new class of high-order fast multi-resolution essentially non-oscillatory (FMRENO) schemes is proposed with an emphasis on both the performance and the computational efficiency. First, a new candidate stencil arrangement is developed for a multi-resolution representation of the local flow scales. A set of candidate stencils ranging from high- to low-order (from large to small stencils) is constructed in a hierarchical manner. Second, the monotonicity-preserving (MP) limiter is introduced as the regularity criterion of the candidate stencils. A candidate stencil, with which the reconstructed cell interface flux locates within the MP lower and upper bounds, is regarded to be smooth. Third, a multi-resolution stencil selection strategy, which prioritizes the stencils with better spectral property or higher-order accuracy meanwhile satisfying the MP criterion, is proposed. If all the candidate stencils are judged to be nonsmooth, the targeted stencil that violates the MP criterion the least is deployed as the final reconstruction instead. With this new framework, the desirable high-order accuracy is restored in the smooth regions while the sharp shock-capturing capability is achieved by selecting the targeted stencil satisfying the MP criterion most. Moreover, the new FMRENO schemes feature low numerical dissipation for resolving the broadband physical fluctuations by adaptively choosing the candidate stencil with better spectra or higher accu-

Lin Fu
linfu@ust.hk

Yue Li
yue06.li@tum.de

Nikolaus A. Adams
nikolaus.adams@tum.de

1   Chair of Aerodynamics and Fluid Mechanics, School of Engineering and Design, Technical University of Munich, 85748 Garching, Germany

2   Department of Mechanical and Aerospace Engineering, The Hong Kong University of Science and Technology, Clear Water Bay, Kowloon, Hong Kong

3   Department of Mathematics, The Hong Kong University of Science and Technology, Clear Water Bay, Kowloon, Hong Kong

4   HKUST Shenzhen-Hong Kong Collaborative Innovation Research Institute, Futian, Shenzhen, China

5   Shenzhen Research Institute, The Hong Kong University of Science and Technology, Shenzhen, China

racy order based on the local flow regularity. Compared to the standard weighted/targeted essentially non-oscillatory (W/TENO) schemes, the computational efficiency is dramatically enhanced by avoiding the expensive evaluations of the classical smoothness indicators. A set of benchmark simulations demonstrate the performance of the new FMRENO schemes for handling complex fluid problems with a wide range of length scales.

Keywords WENO · TENO · Multi-resolution · High-order schemes · Shockwaves · Compressible flow · Turbulence

1 Introduction

High-order and high-resolution shock-capturing schemes are essential numerical methods to solve compressible fluid problems, which may involve discontinuities and broadband flow scales [1–4]. The main objectives are to restore the high-order accuracy in smooth regions with low numerical dissipation while capturing discontinuities sharply without generating spurious oscillations. Among all the concepts proposed in the past decades to cope with this issue [5–10], the family of essentially non-oscillatory (ENO) schemes belongs to one of the most popular methods [2, 11, 12].

The development of the ENO-family schemes and the related variants are briefly reviewed in the following. Harten et al. [7] first propose the high-order ENO scheme, which selects the smoothest stencil from a set of predefined candidate stencils to avoid the Gibbs phenomenon near discontinuities. Widely accepted discretization schemes, weighted essentially non-oscillatory (WENO) schemes, first proposed by Liu et al. [8] and further improved by Jiang and Shu [9], are developed from the ENO concept. Instead of selecting the smoothest candidate, WENO deploys a convex combination of all candidate stencils to achieve high-order accuracy in smooth regions. The optimal linear weights are modulated based on the smoothness indicators such that the desired accuracy order is restored in smooth regions and the ENO property is preserved near discontinuities. The performance of the WENO schemes can be further enhanced by improving the nonlinear weighting strategy, e.g., the WENO-M [13] and WENO-Z [14, 15] schemes avoid the order degeneration near critical points through correcting the nonlinear weights to be closer to the optimal linear ones. On the other hand, the excessive numerical dissipation of WENO (as another typical flaw of WENO-family schemes) can be remedied by freezing the nonlinear adaptation when the ratio between the largest and the smallest calculated smoothness indicator is below a problem-dependent threshold [16]. Alternatively, to reduce the numerical dissipation of the fifth-order WENO scheme, an adaptive central-upwind sixth-order WENO-CU6 [17] scheme is proposed by introducing the contribution of an additional downwind stencil. Other recent work following this direction includes the development of WENO-Z+ scheme [18]. To improve the numerical robustness of the very-high-order WENO reconstructions, monotonicity-preserving WENO schemes [19], positivity-preserving WENO schemes [20], and WENO schemes with recursive-order-reduction [21] are proposed. More recently, Zhu and Shu [22] develop the finite-difference and finite-volume multi-resolution WENO schemes based on a hierarchy of nested unequal-sized central spatial stencils. Following the nonlinear weighting concept of central WENO (CWENO) schemes [23, 24], arbitrary positive linear weights can be employed and the resulting schemes have a gradual degrading of accuracy near discontinuities. However, the aforementioned WENO schemes are rather expensive especially for the very-high-order reconstructions since the calculations of smoothness indicators are inevitable.

As the most recent innovation, the high-order TENO schemes improve the numerical robustness and reduce the unnecessary numerical dissipation by a new candidate stencil arrangement and a novel ENO-like stencil selection strategy [10, 25–33]. In contrast to the WENO-like smooth convex combination of candidate stencils, the TENO scheme either deploys a candidate stencil with its optimal linear weight or discards it completely when crossed by a discontinuity. The TENO scheme has been extended to unstructured meshes [34] and multi-resolution methods [35].

In this paper, a family of FMRENO schemes for both the odd- and even-order reconstructions in a unified framework is proposed. With a set of predefined candidate stencils as the multi-resolution representation of local flow scales, a novel stencil selection strategy is proposed to form the final reconstruction. The selection criterion is provided by the MP limiter [19], with which a candidate stencil is regarded to be smooth if the reconstructed cell interface flux locates within the upper and lower bounds of the MP limiter. Then, the optimal smooth stencil with higher-order accuracy or better spectral property will be adopted as the final reconstruction scheme. As a result, the FMRENO scheme achieves the multi-resolution property by adaptively selecting the targeted candidate stencil according to the local flow regularity and degenerates from high- to low-order reconstruction when approaching the discontinuities. Moreover, the computational efficiency is improved when compared to W/TENO since the evaluations of the smoothness indicators are unnecessary.

The rest of this paper is organized as follows. In Sect. 2, the basic concepts of the WENO and TENO schemes are briefly reviewed. In Sect. 3, a general framework to construct arbitrarily high-order FMRENO schemes is proposed. In Sect. 4, the explicit expressions of FMRENO schemes ranging from fifth- to eighth-order are given. In Sect. 5, a set of benchmark cases is considered to assess the proposed schemes. The concluding remarks are given in the last section.

2 Basic Concepts of W/TENO Schemes

To facilitate the presentation, we consider a one-dimensional scalar hyperbolic conservation law

$$\frac{\partial u}{\partial t} + \frac{\partial}{\partial x} f(u) = 0, \tag{1}$$

where u and f denote the conservative variable and the flux function, respectively. Without losing the generality, the characteristic signal velocity is assumed to be positive $\frac{\partial f(u)}{\partial u} > 0$ in the entire computational domain hereafter.

For a uniform Cartesian mesh with cell centers $x_i = i \Delta x$ and cell interfaces $x_{i+1/2} = x_i + \Delta x/2$, the spatial discretization results in a set of ordinary differential equations

$$\frac{du_i(t)}{dt} = -\frac{\partial f}{\partial x}\Big|_{x=x_i}, \ i = 0, \ldots, n, \tag{2}$$

where u_i denotes the numerical approximation to the point value $u(x_i, t)$. Eq. (2) can be further discretized by a conservative finite-difference scheme as

$$\frac{du_i}{dt} = -\frac{1}{\Delta x}(h_{i+1/2} - h_{i-1/2}), \tag{3}$$

where the primitive function $h(x)$ is implicitly defined by

$$f(x) = \frac{1}{\Delta x} \int_{x-\Delta x/2}^{x+\Delta x/2} h(\xi)d\xi, \tag{4}$$

and $h_{i\pm1/2} = h(x_i \pm \Delta x/2)$. For the purpose of achieving global high-order accuracy of spatial discretization, a high-order approximation of the function $h(x)$ at the cell interface has to be reconstructed from the cell-averaged values of $f(x)$ at the cell centers. Eq. (3) can be written as

$$\frac{du_i}{dt} \approx -\frac{1}{\Delta x}(\hat{f}_{i+1/2} - \hat{f}_{i-1/2}), \tag{5}$$

where $\hat{f}_{i\pm1/2}$ denotes the approximate numerical fluxes and can be computed from different stencils. For a K-point stencil, a K-th order polynomial interpolation of function $h(x)$ can be assumed as

$$h(x) \approx \hat{f}(x) = \sum_{l=0}^{K-1} a_l x^l. \tag{6}$$

After substituting Eq. (6) into Eq. (4) and evaluating the integral functions at the stencil nodes, the coefficients a_l are uniquely determined by solving the resulting system of linear algebraic equations.

For solving hyperbolic conservation laws, discontinuities may occur in the computational domain even when the initial condition is smooth enough. The long-term numerical challenge is to develop a reconstruction scheme that is high-order accurate in smooth regions and captures discontinuities sharply and stably in nonsmooth regions. In the following, we recall the essential elements of different strategies to ensure the above properties.

2.1 The WENO-Z Scheme

With the WENO-family schemes [9, 14], a global ($K = 2r - 1$)-th order approximate numerical flux can be computed from a convex combination of r candidate stencils with the same width r as

$$\hat{f}_{i+1/2} = \sum_{k=0}^{r-1} w_k \hat{f}_{k,i+1/2}, \tag{7}$$

where ω_k denotes the nonlinear weight for each candidate flux, and $\hat{f}_{k,i\pm1/2}$ denotes the r-th order approximate numerical flux similar to the definition in Eq. (6). For WENO-Z schemes [14], the nonlinear weight ω_k of each stencil is renormalized from the optimal linear weight d_k as

$$\omega_k = \frac{\alpha_k^Z}{\sum_{k=0}^{r-1} \alpha_k^Z}, \text{ and } \alpha_k^Z = \frac{d_k}{\beta_k^Z}. \tag{8}$$

In the WENO-Z scheme, the optimal linear weight d_k is the corresponding coefficient for each candidate stencil to achieve maximum accuracy order of the background linear scheme.

Following [36], the calculation of the β_k^Z function is obtained by

$$\frac{1}{\beta_k^Z} = \left(1 + (\frac{\tau_{2r-1}}{\beta_{k,r} + \epsilon})^p\right), \text{ and } p = 1 \text{ or } 2. \tag{9}$$

Following Jiang and Shu [9], the smoothness indicator $\beta_{k,r}$ for the k-th candidate stencil can be given as

$$\beta_{k,r} = \sum_{j=1}^{r-1} \Delta x^{2j-1} \int_{x_{i-1/2}}^{x_{i+1/2}} \left(\frac{d^j}{dx^j} \hat{f}_k(x) \right)^2 dx \tag{10}$$

based on the L_2 norm of the derivatives of the reconstructed candidate polynomials.

The global high-order smoothness indicator τ_{2r-1} is defined with a linear combination of existing low-order smoothness indicators $\beta_{0,r}, \ldots, \beta_{r-1,r}$ as:

$$\tau_{2r-1} = \begin{cases} |\beta_{0,r} - \beta_{r-1,r}|, & \text{if } \mod(r,2) = 1, \\ |\beta_{0,r} - \beta_{1,r} - \beta_{r-2,r} + \beta_{r-1,r}|, & \text{if } \mod(r,2) = 0. \end{cases} \tag{11}$$

2.2 The WENO-S Scheme

In [37], a new smoothness indicator that can decrease the measured smoothness variances on different candidate stencils in smooth regions is proposed. The resulting new schemes based on the same candidate stencils of classical WENO schemes are called WENO-S. For WENO-S schemes [37], the nonlinear weight ω_k^S of each stencil is renormalized from the optimal linear weight d_k as

$$\omega_k^S = \frac{\alpha_k^S}{\sum_{k=0}^{r-1} \alpha_k^S}, \quad \text{and } \alpha_k^S = d_k \left(1 + (\frac{\tau^S}{\beta_k^S + \epsilon}) \right), \tag{12}$$

where the formula of the β_k^S function is given by

$$\beta_k^S = (f_{i+k-3} - f_{i+k-2} - f_{i+k-1} + f_{i+k})^2 + \\ |(-f_{i+k-3} - f_{i+k-2} + f_{i+k-1} + f_{i+k})(-f_{i+k-3} + 3f_{i+k-2} - 3f_{i+k-1} + f_{i+k})|. \tag{13}$$

For the seven-point WENO-S scheme, the global smoothness indicator τ^S can be written as

$$\tau^S = (-f_{i-3} + 4f_{i-2} - 5f_{i-1} + 5f_{i+1} - 4f_{i+2} + f_{i+3})^2 + \\ + |(f_{i-3} - 2f_{i-2} - f_{i-1} + 4f_i - f_{i+1} - 2f_{i+2} + f_{i+3}) \\ (f_{i-3} - 6f_{i-2} + 15f_{i-1} - 20f_i + 15f_{i+1} - 6f_{i+2} + f_{i+3})|. \tag{14}$$

2.3 The TENO Scheme

Different from WENO schemes, arbitrarily high-order TENO schemes can be constructed from a set of candidate stencils with incremental width [10, 25], as shown in Fig. 1. The sequence of stencil width r varying versus the global accuracy order K is as

$$\{r_k\} = \begin{cases} \underbrace{\{3, 3, 3, 4, \ldots, \frac{K+2}{2}\}}_{0,\ldots,K-3}, & \text{if } \mod(K,2) = 0, \\ \underbrace{\{3, 3, 3, 4, \ldots, \frac{K+1}{2}\}}_{0,\ldots,K-3}, & \text{if } \mod(K,2) = 1. \end{cases} \tag{15}$$
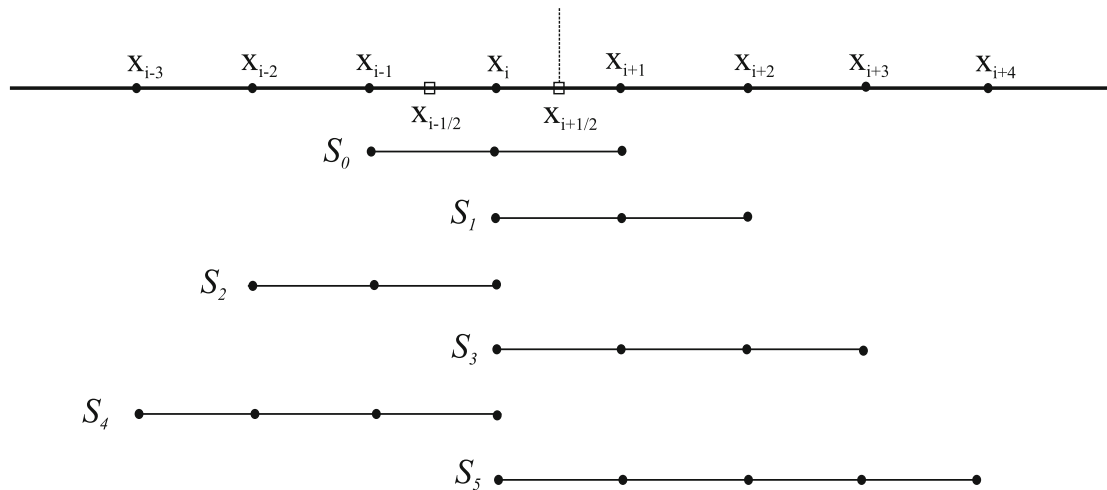
Fig. 1 Sketch of the candidate stencils with incremental width towards high-order TENO reconstructions. The candidate stencils for the eight-point TENO reconstruction scheme are shown in this plot

As WENO schemes, the Kth-order reconstructed numerical flux by TENO at the cell face $i + 1/2$ is given as

$$\hat{f}_{i+1/2} = \sum_{k=0}^{K-3} w_k \hat{f}_{k,i+1/2}, \tag{16}$$

where the nonlinear weight ω_k of each stencil is renormalized from the optimal linear weight d_k as

$$w_k = \frac{d_k \delta_k}{\sum_{k=0}^{K-3} d_k \delta_k}, \tag{17}$$

and δ_k, given as

$$\delta_k = \begin{cases} 0, & \text{if } \chi_k < C_T, \\ 1, & \text{otherwise,} \end{cases} \tag{18}$$

is a sharp cut-off function with the parameter C_T which controls the numerical dissipation and can be determined by spectral analysis [10].

χ_k is a normalized function of the smoothness indicator γ_k, which can be defined as

$$\chi_k = \frac{\gamma_k}{\sum_{k=0}^{K-3} \gamma_k}, \tag{19}$$

and

$$\gamma_k = \left(C + \frac{\tau_K}{\beta_{k,r} + \varepsilon} \right)^q, \quad k = 0, \ldots, K - 3. \tag{20}$$

Here, τ_K is the high-order smoothness indicator which allows for good stability with a reasonably large CFL number and can be constructed as [25]

$$\tau_K = \left| \beta_K - \frac{1}{6}(\beta_{1,3} + \beta_{2,3} + 4\beta_{0,3}) \right| = \mathcal{O}(\Delta x^6), \quad K \geq 5 \tag{21}$$

where β_K measures the global smoothness on the K-point full stencil, for any Kth-order TENO scheme (higher than fourth-order). $\varepsilon = 10^{-40}$ is introduced to prevent the zero

denominator. Moreover, the parameters $C = 1$ and $q = 6$ are adopted for strong scale separation, which means that discontinuities can be isolated from smooth regions effectively. Similarly to WENO schemes, $\beta_{k,r}$ can be defined following Eq. (10) [9].

3 Framework for Constructing the High-Order FMRENO Schemes

The previous work of TENO [26] demonstrates that the high-order accuracy and the ENO property can be enforced by properly selecting the targeted stencil from a set of predefined candidates and the linear/nonlinear convex combination is not necessary. The main flaw of TENO schemes [26], which applies to the WENO-family schemes [9, 14] as well, is that the evaluation of the smoothness indicators is expensive, particularly for very-high-order reconstructions [29].

The objective of this work is to propose a new family of FMRENO schemes, which is computationally cheap and also competitive in terms of performance. In this section, the three main phases for constructing the high-order FMRENO schemes are elaborated in detail, i.e. (1) prepare the hierarchically nested candidate stencils; (2) provide the regularity criterion based on the MP concept; (3) form the final high-order reconstruction by a new multi-resolution stencil selection strategy.

3.1 The Hierarchical Nested Candidate Stencil Arrangement

Motivated by the construction of TENO schemes [26], the candidate stencil arrangement of a K-th order reconstruction should satisfy the following principles: (1) in order to achieve a multi-resolution representation of the local flow scales, a set of candidate stencils with interpolation polynomials of order $k = 3, \ldots, K$ is constructed in a hierarchical nested manner; (2) all candidate stencils contain at least one-point upwinding such that no pure downwind stencil can be deployed for the final reconstruction. As shown in the standard TENO schemes [10], this condition ensures the good numerical stability of even-order reconstructions in non-smooth regions; (3) the candidate stencil arrangement allows that, in nonsmooth regions, at least one candidate stencil is not crossed by discontinuities to ensure the ENO property.

Following the above principles, the candidate stencil arrangements for the five-, six-, seven- and eight-point FMRENO schemes are given in Figs. 2, 3, 4 and 5, respectively. It is worth noting that, such a candidate stencil arrangement is applicable for arbitrarily high-order reconstructions, i.e., for both the odd- and even-order FMRENO schemes.

For each candidate stencil $S_{r,m}$, a polynomial interpolation function (typically r-th order with r stencil points) for $h(x)$ can be constructed similar to the definition in Eq. (6) and the resulting flux function evaluated at $i + 1/2$ is denoted as $\hat{f}^r_{m,i+1/2}$. Among all candidate stencils with the same width r, a priority sequence (as indicated by the value m) to form the final reconstruction is: the high-order central schemes, the optimized central schemes (if there are), the downwind-biased schemes, and the upwind-biased schemes. Such an arrangement ensures that the candidate stencil with higher accuracy order or better spectral property features the priority to be selected for the final reconstruction.

3.2 MP-Based Regularity Criterion

Extensive numerical experiments demonstrate that the MP scheme proposed by Suresh and Huynh [19] is able to distinguish smooth local extrema from genuine discontinuities and is
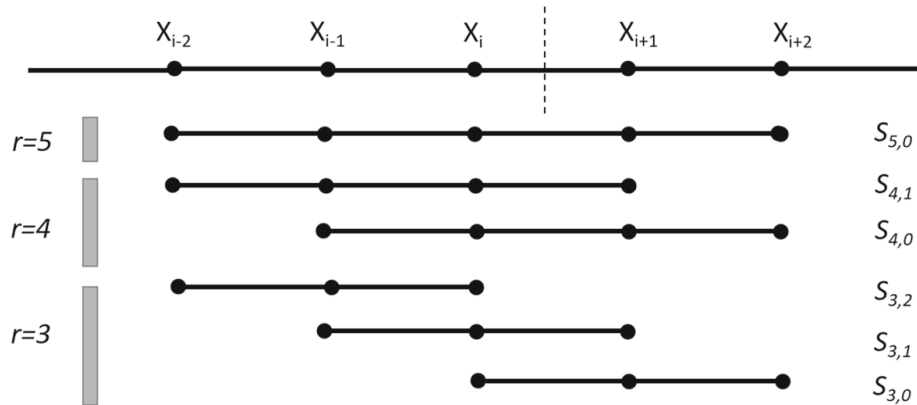
Fig. 2 Hierarchically nested candidate stencils for five-point FMRENO scheme: admissible stencils with stencil point number $r = 3, 4, 5$. For candidate stencil $S_{r,m}$, m denotes the sequence order among all the r-point candidates and a smaller value indicates a higher priority to be selected for the final reconstruction
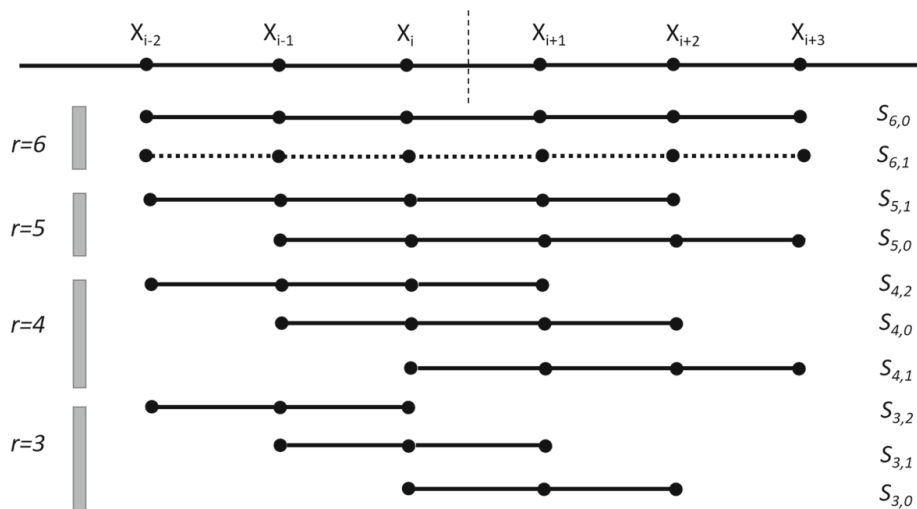

Fig. 3 The hierarchically nested candidate stencils for six-point FMRENO scheme: admissible stencils with stencil point number $r = 3, 4, 5, 6$. For candidate stencil $S_{r,m}$, m denotes the sequence order among all the r-point candidates and a smaller value indicates a higher priority to be selected for the final reconstruction. Also included is the stencil $S_{6,1}$ represented with the dashed line, which is generally an optimized six-point scheme for a better spectral property by relaxing the accuracy-order constraint. Note that, for the odd-order reconstruction, such an additional optimal scheme is not necessary

robust for shock-dominated flows [38–40]. Instead of deploying the MP limiter to modify the reconstructed cell interface flux for suppressing numerical oscillations as in [19] and [40], in this work, we propose to utilize the MP limiter as a local regularity criterion, which judges the candidate stencil to be smooth or not. More specifically, one candidate stencil is judged to be smooth only when the reconstructed cell interface flux locates within the MP upper and lower bounds, which will be defined as follows.

As given in [19] and [40], the lower and upper bounds of the cell interface flux at $i + 1/2$ are given by

$$
\begin{aligned}
\hat{f}_{i+1/2}^{\min} &= \max[\min(f_i, f_{i+1}, \hat{f}_{i+1/2}^{\mathrm{MD}}), \min(f_i, \hat{f}_{i+1/2}^{\mathrm{UL}}, \hat{f}_{i+1/2}^{\mathrm{LC}})], \\
\hat{f}_{i+1/2}^{\max} &= \min[\max(f_i, f_{i+1}, \hat{f}_{i+1/2}^{\mathrm{MD}}), \max(f_i, \hat{f}_{i+1/2}^{\mathrm{UL}}, \hat{f}_{i+1/2}^{\mathrm{LC}})],
\end{aligned}
\tag{22}
$$

where $\hat{f}_{i+1/2}^{\mathrm{UL}}$, $\hat{f}_{i+1/2}^{\mathrm{MD}}$ and $\hat{f}_{i+1/2}^{\mathrm{LC}}$ denote the left-side upper limiter, the median value of the solution, and the left-side value allowing for a large curvature in the solution, respectively.
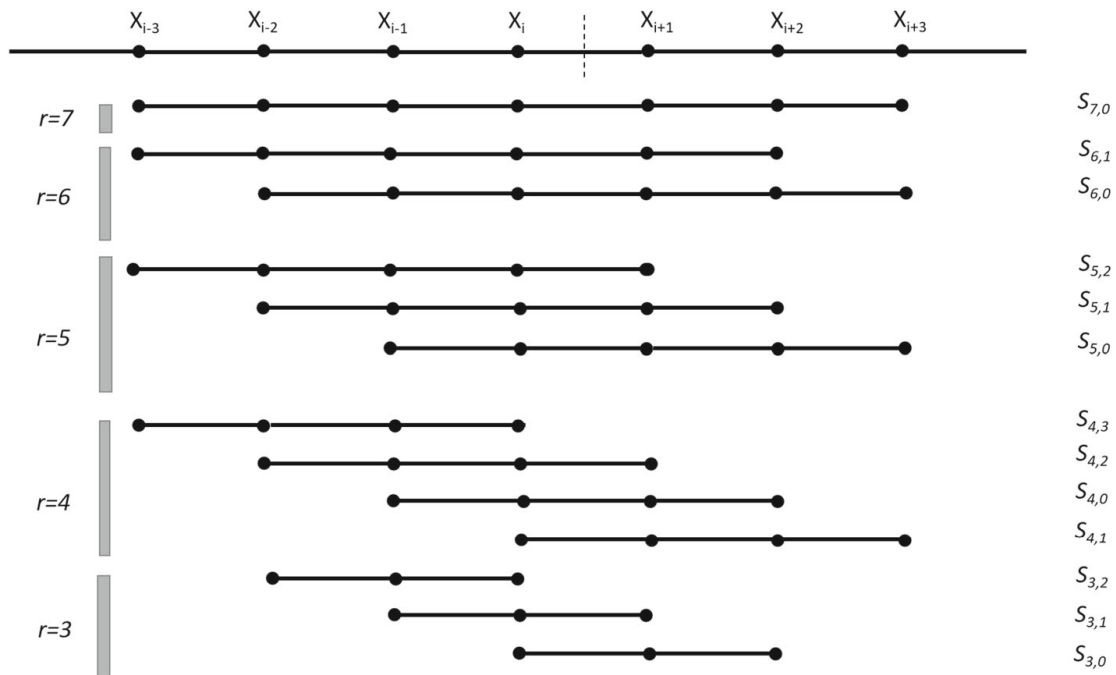
Fig. 4 Hierarchically nested candidate stencils for seven-point FMRENO scheme: admissible stencils with stencil point number $r = 3, 4, 5, 6, 7$. For candidate stencil $S_{r,m}$, m denotes the sequence order among all the r-point candidates and a smaller value indicates a higher priority to be selected for the final reconstruction.
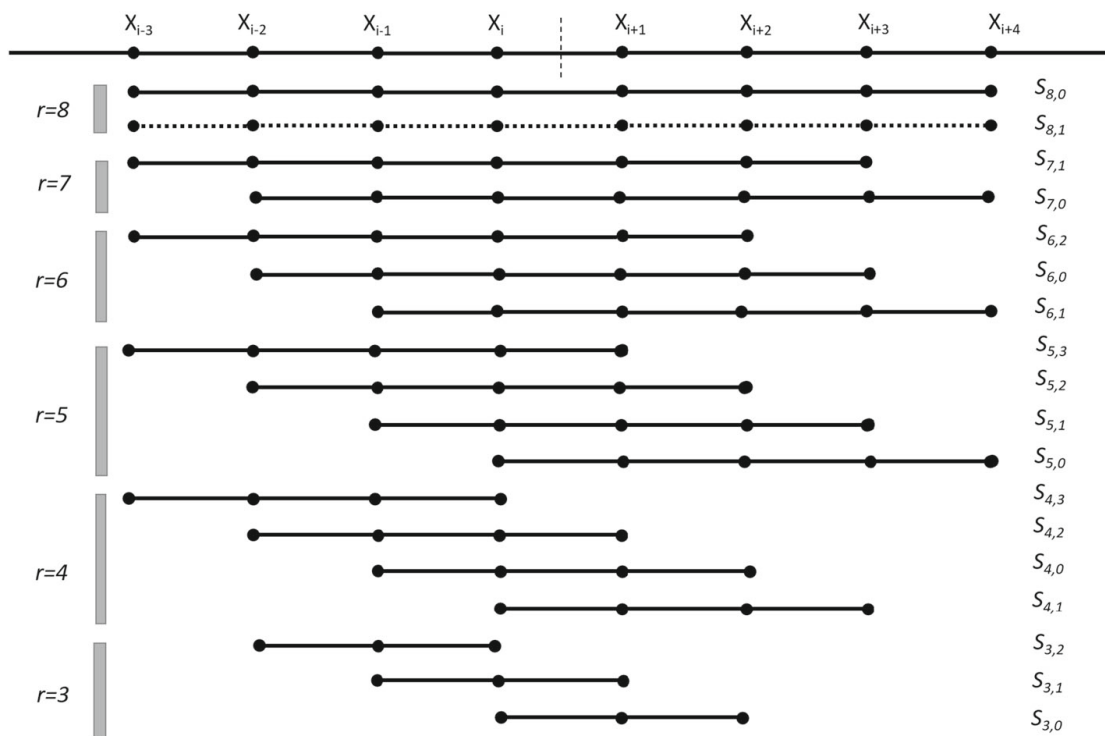

Fig. 5 Hierarchically nested candidate stencils for eight-point FMRENO scheme: admissible stencils with stencil point number $r = 3, 4, 5, 6, 7, 8$. For candidate stencil $S_{r,m}$, m denotes the sequence order among all the r-point candidates and a smaller value indicates a higher priority to be selected for the final reconstruction. Also included is the stencil $S_{8,1}$ represented with the dashed line, which is generally an optimized eight-point scheme for a better spectral property by relaxing the accuracy-order constraint.

Specifically, the left-side upper limiter is given by

$$\hat{f}_{i+1/2}^{UL} = f_i + \alpha(f_i - f_{i-1}), \tag{23}$$

where $\alpha = 2.5$ is employed to enable stability.

The median value of the solution at $x_{i+1/2}$ is given by

$$\hat{f}_{i+1/2}^{MD} = \frac{1}{2}(f_i + f_{i+1}) - \frac{1}{2}d_{i+1/2}^{MD}. \tag{24}$$

The left-side value allowing for a large curvature in the solution at $x_{i+1/2}$ can be given by

$$\hat{f}_{i+1/2}^{LC} = f_i + \frac{1}{2}(f_i - f_{i-1}) + \frac{\beta}{3}d_{i-1/2}^{LC}, \tag{25}$$

where it is recommended to set $\beta = 4$. Following [19] and [40], $d_{i+1/2}^{MD} = d_{i+1/2}^{LC} = d_{i+1/2}^{M}$ is adopted, and the curvature measurement at the cell interface $i + 1/2$ can be defined as

$$d_{i+1/2}^{M} = \text{minmod}(d_i, d_{i+1}), \tag{26}$$

with $d_i = f_{i+1} - 2f_i + f_{i-1}$, and $d_{i+1} = f_{i+2} - 2f_{i+1} + f_i$.

3.3 A Multi-resolution Stencil Selection Strategy

In order to restore the optimal high-order accuracy in smooth regions and enforce the ENO property near discontinuities, a multi-resolution stencil selection strategy is proposed based on the new candidate stencil arrangement and the MP-based regularity criterion as described in previous subsections. The detailed algorithms are summarized as in Algorithm 1.

Specifically, the regularity of each candidate stencil is examined by the MP-based criterion in a one-by-one manner and the priority is given to the stencil with higher accuracy order (typically with larger stencil width r) or with better spectral property (e.g., with a smaller value of m in Figs. 2, 3, 4 and 5). Once one candidate stencil satisfies the regularity criterion, i.e. judged to be smooth by the MP criterion, it is assigned as the final reconstruction scheme without further turning to candidate stencils with lower priorities. If all predefined candidate stencils fail to enforce the MP criterion, then the smoothest candidate, with which the predicted cell interface value departs from the MP upper and lower bounds the least, will be adopted as the final reconstruction for numerical stability.

As a result, (i) in smooth regions, the first largest stencil will be adopted as the final reconstruction scheme ensuring that the desired high-order accuracy is restored; (2) for wave-like structures, the reconstruction tends to select the stencil assigned with a higher priority, i.e. higher accuracy order or better spectral property, according to the local flow regularity. This multi-resolution type stencil selection ensures low numerical dissipation for resolving the broadband physical fluctuations; (3) near discontinuities, the reconstruction gradually degenerates to a smaller stencil with lower priority until it is judged to be smooth by the MP regularity criterion or the so-called smoothest candidate flux which minimizes $|\hat{f}_{m,i+1/2}^{r} - \frac{1}{2}(\hat{f}_{i+1/2}^{max} + \hat{f}_{i+1/2}^{min})|$ for all r and m.

When compared to the standard W/TENO schemes, the expensive evaluation of the smoothness indicators is avoided and the linear combination of candidate stencils is not necessary. Moreover, with increasing targeted reconstruction accuracy order, the cost increase of the FMRENO scheme is negligible whilst that of W/TENO scheme is generally substantial.

Algorithm 1 Pseudo-code for constructing the Kth-order FMRENO scheme

---

1: Build the hierarchically nested candidate stencils according to the method described in Sect. 3.1;
2: Compute the MP upper and lower bounds, i.e. $\hat{f}_{i+1/2}^{\max}$ and $\hat{f}_{i+1/2}^{\min}$, following Sect. 3.2 as the stencil selection criterion;
3: **function** MULTI- RESOLUTION STENCIL SELECTION
4:     $r = K, m = 0$;
5:     **while** $r >= 3$ **do**
6:       Calculate the reconstructed cell interface flux $\hat{f}_{m,i+1/2}^r$ for the candidate stencil $S_{r,m}$;
7:       **if** $\hat{f}_{i+1/2}^{\min} - \epsilon_0 < \hat{f}_{m,i+1/2}^r < \hat{f}_{i+1/2}^{\max} + \epsilon_0$ **then** $\triangleright \epsilon_0 = 10^{-6}$ is a small number to avoid the effects of the machine round-off;
8:         $\hat{f}_{i+1/2} = \hat{f}_{m,i+1/2}^r$;
9:         **return** $\hat{f}_{i+1/2}$;   *▷ terminate the stencil selection;*
10:       **else**
11:         **while** $m \in [0, m_{max} - 1]$ for r-point stencils **do**
12:           $m \leftarrow m + 1$;
13:           go to line 6 ;
14:         **end while**
15:         $r \leftarrow r - 1$;
16:         go to line 5 ;
17:       **end if**
18:     **end while**
19:     **for** all r, m **do**   *▷ select the smoothest candidate $\hat{f}_s$;*
20:       $\hat{f}_s = \hat{f}_{m,i+1/2}^r$, **if** $|\hat{f}_{m,i+1/2}^r - \frac{1}{2}(\hat{f}_{i+1/2}^{\max} + \hat{f}_{i+1/2}^{\min})|$ **is smaller**;
21:     **end for**
22:     $\hat{f}_{i+1/2} = \hat{f}_s$;
23:     **return** $\hat{f}_{i+1/2}$;   *▷ terminate the stencil selection;*
24: **end function**

---

4 Explicit Expressions of FMRENO Schemes

In this section, the formulas for fifth- to eighth-order FMRENO schemes are explicitly given. It is worth noting that the candidate schemes may also be constructed as other non-polynomial functions [41].

4.1 Five-Point FMRENO Scheme

All candidate stencils used to construct a five-point FMRENO scheme (referred to as FMRENO5) are given as

$$\hat{f}^5_{0,i+1/2} = -\frac{1}{60}(-2f_{i-2} + 13f_{i-1} - 47f_i - 27f_{i+1} + 3f_{i+2}),$$
$$\hat{f}^4_{0,i+1/2} = -\frac{1}{12}(f_{i-1} - 7f_i - 7f_{i+1} + f_{i+2}),$$
$$\hat{f}^4_{1,i+1/2} = \frac{1}{12}(f_{i-2} - 5f_{i-1} + 13f_i + 3f_{i+1}),$$
$$\hat{f}^3_{0,i+1/2} = \frac{1}{6}(2f_i + 5f_{i+1} - f_{i+2}),$$
$$\hat{f}^3_{1,i+1/2} = \frac{1}{6}(-f_{i-1} + 5f_i + 2f_{i+1}),$$
$$\hat{f}^3_{2,i+1/2} = \frac{1}{6}(2f_{i-2} - 7f_{i-1} + 11f_i).$$

$$(27)$$

4.2 Six-Point FMRENO Scheme

All candidate stencils used to construct a six-point FMRENO scheme (referred to as FMRENO6) are given as

$$\hat{f}^6_{0,i+1/2} = \frac{1}{60}(f_{i-2} - 8f_{i-1} + 37f_i + 37f_{i+1} - 8f_{i+2} + f_{i+3}),$$
$$\hat{f}^6_{1,i+1/2} = -\frac{57}{6000}(-2f_{i-2} + 13f_{i-1} - 47f_i - 27f_{i+1} + 3f_{i+2}) +$$
$$\frac{43}{6000}(-3f_{i-1} + 27f_i + 47f_{i+1} - 13f_{i+2} + 2f_{i+3}),$$
$$\hat{f}^5_{0,i+1/2} = \frac{1}{60}(-3f_{i-1} + 27f_i + 47f_{i+1} - 13f_{i+2} + 2f_{i+3}),$$
$$\hat{f}^5_{1,i+1/2} = -\frac{1}{60}(-2f_{i-2} + 13f_{i-1} - 47f_i - 27f_{i+1} + 3f_{i+2}),$$
$$\hat{f}^4_{0,i+1/2} = -\frac{1}{12}(f_{i-1} - 7f_i - 7f_{i+1} + f_{i+2}),$$
$$\hat{f}^4_{1,i+1/2} = \frac{1}{12}(3f_i + 13f_{i+1} - 5f_{i+2} + f_{i+3}),$$
$$\hat{f}^4_{2,i+1/2} = \frac{1}{12}(f_{i-2} - 5f_{i-1} + 13f_i + 3f_{i+1}),$$
$$\hat{f}^3_{0,i+1/2} = \frac{1}{6}(2f_i + 5f_{i+1} - f_{i+2}),$$
$$\hat{f}^3_{1,i+1/2} = \frac{1}{6}(-f_{i-1} + 5f_i + 2f_{i+1}),$$
$$\hat{f}^3_{2,i+1/2} = \frac{1}{6}(2f_{i-2} - 7f_{i-1} + 11f_i),$$

$$(28)$$

where $\hat{f}^6_{1,i+1/2}$ denotes a central scheme with optimized dispersion-dissipation relation [25].

4.3 Seven-Point FMRENO Scheme

All candidate stencils used to construct a seven-point FMRENO scheme (referred to as FMRENO7) are given as

$$\hat{f}^7_{0,i+1/2} = \frac{1}{420}(-3f_{i-3} + 25f_{i-2} - 101f_{i-1} + 319f_i + 214f_{i+1} - 38f_{i+2} + 4f_{i+3}),$$
$$\hat{f}^6_{0,i+1/2} = \frac{1}{60}(f_{i-2} - 8f_{i-1} + 37f_i + 37f_{i+1} - 8f_{i+2} + f_{i+3}),$$
$$\hat{f}^6_{1,i+1/2} = -\frac{1}{60}(f_{i-3} - 7f_{i-2} + 23f_{i-1} - 57f_i - 22f_{i+1} + 2f_{i+2}),$$
$$\hat{f}^5_{0,i+1/2} = \frac{1}{60}(-3f_{i-1} + 27f_i + 47f_{i+1} - 13f_{i+2} + 2f_{i+3}),$$
$$\hat{f}^5_{1,i+1/2} = -\frac{1}{60}(-2f_{i-2} + 13f_{i-1} - 47f_i - 27f_{i+1} + 3f_{i+2}),$$
$$\hat{f}^5_{2,i+1/2} = \frac{1}{60}(-3f_{i-3} + 17f_{i-2} - 43f_{i-1} + 77f_i + 12f_{i+1}),$$
$$\hat{f}^4_{0,i+1/2} = -\frac{1}{12}(f_{i-1} - 7f_i - 7f_{i+1} + f_{i+2}),$$
$$\hat{f}^4_{1,i+1/2} = \frac{1}{12}(3f_i + 13f_{i+1} - 5f_{i+2} + f_{i+3}),$$
$$\hat{f}^4_{2,i+1/2} = \frac{1}{12}(f_{i-2} - 5f_{i-1} + 13f_i + 3f_{i+1}),$$
$$\hat{f}^4_{3,i+1/2} = \frac{1}{12}(-3f_{i-3} + 13f_{i-2} - 23f_{i-1} + 25f_i),$$
$$\hat{f}^3_{0,i+1/2} = \frac{1}{6}(2f_i + 5f_{i+1} - f_{i+2}),$$
$$\hat{f}^3_{1,i+1/2} = \frac{1}{6}(-f_{i-1} + 5f_i + 2f_{i+1}),$$
$$\hat{f}^3_{2,i+1/2} = \frac{1}{6}(2f_{i-2} - 7f_{i-1} + 11f_i).$$

$$(29)$$

4.4 Eight-Point FMRENO Scheme

All candidate stencils used to construct an eight-point FMRENO scheme (referred to as FMRENO8) are given as

$$
\begin{aligned}
\hat{f}^8_{0,i+1/2} &= -\tfrac{1}{840}(3f_{i-3} - 29f_{i-2} + 139f_{i-1} - 533f_i - 533f_{i+1} + 139f_{i+2} - 29f_{i+3} + 3f_{i+4}), \\
\hat{f}^8_{1,i+1/2} &= -0.007723837710877\,f_{i-3} + 0.05728582585522101\,f_{i-2} \\
&\quad -0.214847819872312\,f_{i-1} + 0.6852858258552214\,f_i \\
&\quad +0.6152858258552207\,f_{i+1} - 0.1728478198727316\,f_{i+2} \\
&\quad +0.04328582585522106\,f_{i+3} - 0.005723831837710886\,f_{i+4}, \\
\hat{f}^7_{0,i+1/2} &= -\tfrac{1}{420}(-4f_{i-2} + 38f_{i-1} - 214f_i - 319f_{i+1} + 101f_{i+2} - 25f_{i+3} + 3f_{i+4}), \\
\hat{f}^7_{1,i+1/2} &= \tfrac{1}{420}(-3f_{i-3} + 25f_{i-2} - 101f_{i-1} + 319f_i + 214f_{i+1} - 38f_{i+2} + 4f_{i+3}), \\
\hat{f}^6_{0,i+1/2} &= \tfrac{1}{60}(f_{i-2} - 8f_{i-1} + 37f_i + 37f_{i+1} - 8f_{i+2} + f_{i+3}), \\
\hat{f}^6_{1,i+1/2} &= -\tfrac{1}{60}(2f_{i-1} - 22f_i - 57f_{i+1} + 23f_{i+2} - 7f_{i+3} + f_{i+4}), \\
\hat{f}^6_{2,i+1/2} &= -\tfrac{1}{60}(f_{i-3} - 7f_{i-2} + 23f_{i-1} - 57f_i - 22f_{i+1} + 2f_{i+2}), \\
\hat{f}^5_{0,i+1/2} &= -\tfrac{1}{60}(-12f_i - 77f_{i+1} + 43f_{i+2} - 17f_{i+3} + 3f_{i+4}), \\
\hat{f}^5_{1,i+1/2} &= \tfrac{1}{60}(-3f_{i-1} + 27f_i + 47f_{i+1} - 13f_{i+2} + 2f_{i+3}), \\
\hat{f}^5_{2,i+1/2} &= -\tfrac{1}{60}(-2f_{i-2} + 13f_{i-1} - 47f_i - 27f_{i+1} + 3f_{i+2}), \\
\hat{f}^5_{3,i+1/2} &= \tfrac{1}{60}(-3f_{i-3} + 17f_{i-2} - 43f_{i-1} + 77f_i + 12f_{i+1}), \\
\hat{f}^4_{0,i+1/2} &= -\tfrac{1}{12}(f_{i-1} - 7f_i - 7f_{i+1} + f_{i+2}), \\
\hat{f}^4_{1,i+1/2} &= \tfrac{1}{12}(3f_i + 13f_{i+1} - 5f_{i+2} + f_{i+3}), \\
\hat{f}^4_{2,i+1/2} &= \tfrac{1}{12}(f_{i-2} - 5f_{i-1} + 13f_i + 3f_{i+1}), \\
\hat{f}^4_{3,i+1/2} &= \tfrac{1}{12}(-3f_{i-3} + 13f_{i-2} - 23f_{i-1} + 25f_i), \\
\hat{f}^3_{0,i+1/2} &= \tfrac{1}{6}(2f_i + 5f_{i+1} - f_{i+2}), \\
\hat{f}^3_{1,i+1/2} &= \tfrac{1}{6}(-f_{i-1} + 5f_i + 2f_{i+1}), \\
\hat{f}^3_{2,i+1/2} &= \tfrac{1}{6}(2f_{i-2} - 7f_{i-1} + 11f_i),
\end{aligned}
\tag{30}
$$

where $\hat{f}^8_{1,i+1/2}$ denotes a central scheme with optimized dispersion-dissipation relation [25].

5 Numerical Validations

In this section, a set of critical benchmark cases involving strong discontinuities and broadband flow length scales is simulated. With the finite-difference framework, the proposed FMRENO schemes are extended to multi-dimensional problems in a dimension-by-dimension manner. For systems of hyperbolic conservation laws, the characteristic decomposition method based on the Roe average [42] is employed for effectively suppressing numerical oscillations. The Rusanov scheme [43] is adopted as the flux splitting method if not mentioned otherwise. The third-order strong stability-preserving (SSP) Runge-Kutta method [44] with a typical CFL number of 0.4 is adopted for the time advancement. Meanwhile, the numerical results from WENO5-Z, WENO7-S [37], WENO-CU6 [45] and TENO8 [27] are compared.

To facilitate the accurate measurement of the computational time with one CPU (avoiding the effects of parallelization), the simulation resolution of some 2D cases, i.e., 2D Riemann problems, will be decreased.

Table 1 Convergence statistics of numerical error with L_∞ norm from five-point schemes for the linear advection problem

N	WENO5-Z		FMRENO5	
	L_∞ error	Order	L_∞ error	Order
25	1.04E−04	–	1.04E−04	–
50	3.27E−06	4.99	3.27E−06	4.99
75	4.32E−07	4.99	4.32E−07	4.99
100	1.02E−07	5.00	1.02E−07	5.00
150	1.35E−08	5.00	1.35E−08	5.00

Table 2 Convergence statistics of numerical error with L_∞ norm from six-point schemes for the linear advection problem

N	WENO-CU6		FMRENO6	
	L_∞ error	Order	L_∞ error	Order
25	1.11E−05	–	1.12E−05	–
50	1.76E−07	5.99	1.76E−07	5.99
75	1.55E−08	5.99	1.55E−08	5.99
100	2.76E−09	6.00	2.76E−09	6.00
150	2.43E−10	6.00	2.43E−10	6.00

5.1 Accuracy Verifications

5.1.1 Advection Problem

We first consider the one-dimensional Gaussian pulse advection problem [46]. The linear advection equation

$$\frac{\partial u}{\partial t} + \frac{\partial u}{\partial x} = 0, \tag{31}$$

with initial condition

$$u(x, 0) = \sin(\pi x), \tag{32}$$

is solved in a computational domain $0 \le x \le 2$ and the final time is $t = 2$. Periodic boundary conditions are imposed at $x = 0$ and $x = 2$.

As shown in Tables 1, 2, 3 and 4, the desired accuracy order is achieved for all the present FMRENO schemes.

5.1.2 Burgers Problem

Further, we consider the 2D inviscid nonlinear Burgers equation [47]

$$\frac{\partial u}{\partial t} + \frac{\partial (\frac{u^2}{2})}{\partial x} + \frac{\partial (\frac{u^2}{2})}{\partial y} = 0. \tag{33}$$

The equation with an initial condition $u(x, y, 0) = \sin(\pi(x + y)/2)$ is solved in a computational domain $[0, 4] \times [0, 4]$ and periodic boundary conditions are imposed at the left and

Table 3 Convergence statistics of numerical error with L_∞ norm from seven-point schemes for the linear advection problem

N	WENO7-S		FMRENO7	
	L_∞ error	Order	L_∞ error	Order
10	7.60E−04	–	7.60E−04	–
20	6.62E−06	6.84	6.62E−06	6.84
30	3.91E−07	6.98	3.91E−07	6.98
40	5.27E−08	6.97	5.27E−08	6.97
60	3.10E−09	6.98	3.10E−09	6.98

Table 4 Convergence statistics of numerical error with L_∞ norm from eight-point schemes for the linear advection problem

N	TENO8		FMRENO8	
	L_∞ error	Order	L_∞ error	Order
10	2.07E−04	–	2.07E−04	–
20	9.10E−07	7.83	9.10E−07	7.83
30	3.63E−08	7.95	3.63E−08	7.95
40	3.66E−09	7.97	3.66E−09	7.97
60	1.44E−10	7.98	1.44E−10	7.98

right boundaries. The simulation is conducted up to $t = 0.5/\pi$, when the solution is still smooth.

Numerical error statistics and accuracy orders for the WENO5-Z, WENO-CU6, WENO7-S, TENO8 and FMRENO schemes are shown in Tables 5, 6, 7 and 8, respectively. The presented data shows that FMRENO schemes can achieve the desired accuracy order even in nonlinear advection problems.

Figure 6 shows the L_∞ numerical error versus the total CPU computational time from the WENO5-Z, WENO-CU6, WENO7-S, TENO8, and FMRENO schemes. It is observed that to achieve the same level of numerical error, the required computational cost from the present scheme is lower than that from the corresponding classical W/TENO scheme of the same accuracy order.

Note that, the order of convergence with WENO7-S and TENO8 schemes is not as expected in Tables 7 and 8. This is consistent with the report by [13, 15] that the magnitude of ϵ may change the order of convergence of the scheme when the machine round-off error accumulates in smooth regions of flow with $\Delta x \to 0$. In order to study the sensitivity based on the adopted computer with double precision, in Tables 9 and 10, we show the convergence statistics of WENO7-S and TENO8 schemes with $\epsilon = 10^{-8}$, $\epsilon = 10^{-10}$ and $\epsilon = 10^{-40}$ for the Burgers problem, respectively. The expected accuracy order is restored for both schemes when a proper value of ϵ is adopted. The default value of $\epsilon = 10^{-40}$ is applied in this work, simply as recommended by the original reference papers [25, 37].

Table 5 Convergence statistics of numerical error with L_∞ norm from the five-point schemes for the Burgers problem

Resolution	WENO5-Z		FMRENO5	
	L_∞ error	Order	L_∞ error	Order
20×20	5.41E−03	–	6.91E−03	–
40×40	6.17E−04	3.13	6.35E−04	3.44
80×80	2.20E−05	4.81	2.21E−05	4.84
120×120	2.95E−06	4.96	2.95E−06	4.97
160×160	6.84E−07	5.08	6.83E−07	5.08

Table 6 Convergence statistics of numerical error with L_∞ norm from the six-point schemes for the Burgers problem

Resolution	WENO-CU6		FMRENO6	
	L_∞ error	Order	L_∞ error	Order
20×20	4.07E−03	–	4.32E−03	–
40×40	3.50E−04	3.54	3.50E−04	3.63
80×80	8.23E−06	5.41	8.23E−05	5.41
120×120	8.88E−07	5.49	8.88E−06	5.49
180×180	9.29E−08	5.57	8.17E−08	5.88

Table 7 Convergence statistics of numerical error with L_∞ norm from the seven-point schemes for the Burgers problem

Resolution	WENO7-S		FMRENO7	
	L_∞ error	Order	L_∞ error	Order
20×20	2.31E−03	–	3.19E−03	–
40×40	2.25E−04	3.36	2.24E−04	3.83
80×80	3.39E−06	6.05	3.44E−06	6.02
120×120	3.27E−07	5.77	2.20E−07	6.79
180×180	4.30E−08	5.00	1.25E−08	7.08

Table 8 Convergence statistics of numerical error with L_∞ norm from the eight-point schemes for the Burgers problem

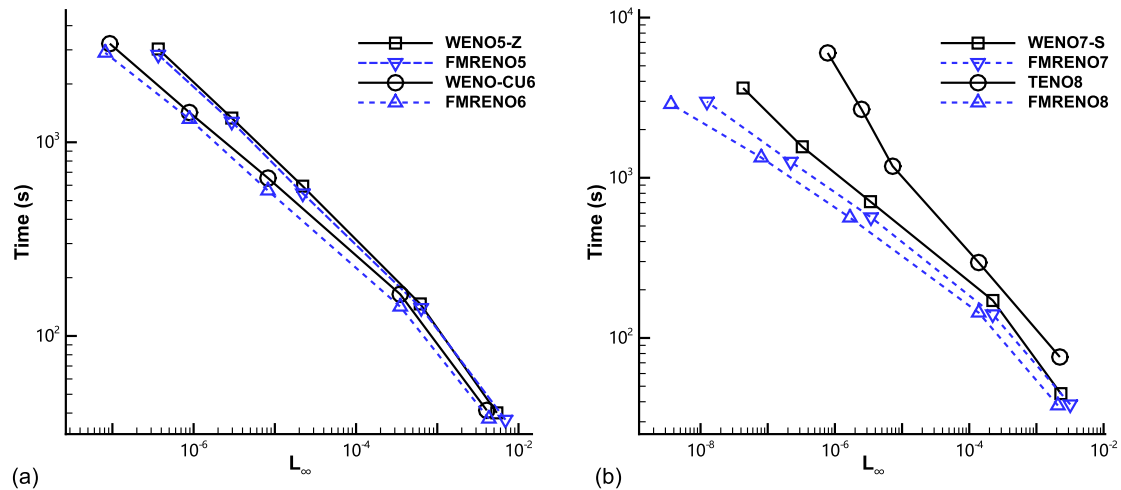| Resolution	TENO8		FMRENO8	
	L_∞ error	Order	L_∞ error	Order
20×20	2.23E−03	–	2.09E−03	–
40×40	1.38E−04	4.01	1.38E−04	3.92
80×80	7.25E−06	4.25	1.68E−06	6.37
120×120	2.49E−06	2.63	8.01E−08	7.50
180×180	7.81E−07	2.86	3.27E−09	7.89

Fig. 6 Burgers equation: the L_∞ numerical error versus the total CPU computational time from the WENO5-Z, WENO-CU6, WENO7-S, TENO8, and FMRENO schemes. Discretization is on 20×20, 40×40, 80×80, 120×120, and 180×180 uniformly distributed grid points

Table 9 Convergence statistics of numerical error with L_∞ norm from WENO7-S scheme for the Burgers problem with various ϵ

Resolution	$\epsilon = 10^{-8}$		$\epsilon = 10^{-10}$		$\epsilon = 10^{-40}$	
	L_∞ error	Order	L_∞ error	Order	L_∞ error	order
20×20	2.31E−3	–	2.31E−3	–	2.31E−3	–
40×40	2.25E−4	3.36	2.25E−4	3.36	2.25E−4	3.36
80×80	3.39E−6	6.05	3.39E−6	6.05	3.39E−6	6.05
120×120	2.20E−7	6.74	2.20E−7	6.74	3.27E−7	5.77
180×180	1.25E−8	7.08	1.25E−8	7.08	4.30E−8	5.00

Table 10 Convergence statistics of numerical error with L_∞ norm from TENO8 scheme for the Burgers problem with various ϵ

Resolution	$\epsilon = 10^{-8}$		$\epsilon = 10^{-10}$		$\epsilon = 10^{-40}$	
	L_∞ error	Order	L_∞ error	Order	L_∞ error	order
20×20	2.23E−3	–	2.23E−3	–	2.23E−3	–
40×40	1.38E−4	4.01	1.38E−4	4.01	1.38E−4	4.01
80×80	1.68E−6	6.37	1.80E−6	6.26	7.25E−6	4.25
120×120	8.01E−8	7.50	8.01E−8	7.68	2.49E−6	2.63
180×180	3.63E−9	7.63	3.63E−9	7.63	7.81E−7	2.86
200×200	1.59E−9	7.86	1.59E−9	7.86	4.78E−7	5.27

5.2 Shock-Tube Problem

Lax's problem [48] and Sod's problem [49] are considered here. The initial condition for Lax's problem [48] is

$$(\rho, u, p) = \begin{cases} (0.445, 0.698, 3.528), & \text{if } 0 \leq x < 0.5, \\ (0.5, 0, 0.5710), & \text{if } 0.5 \leq x \leq 1, \end{cases} \quad (34)$$
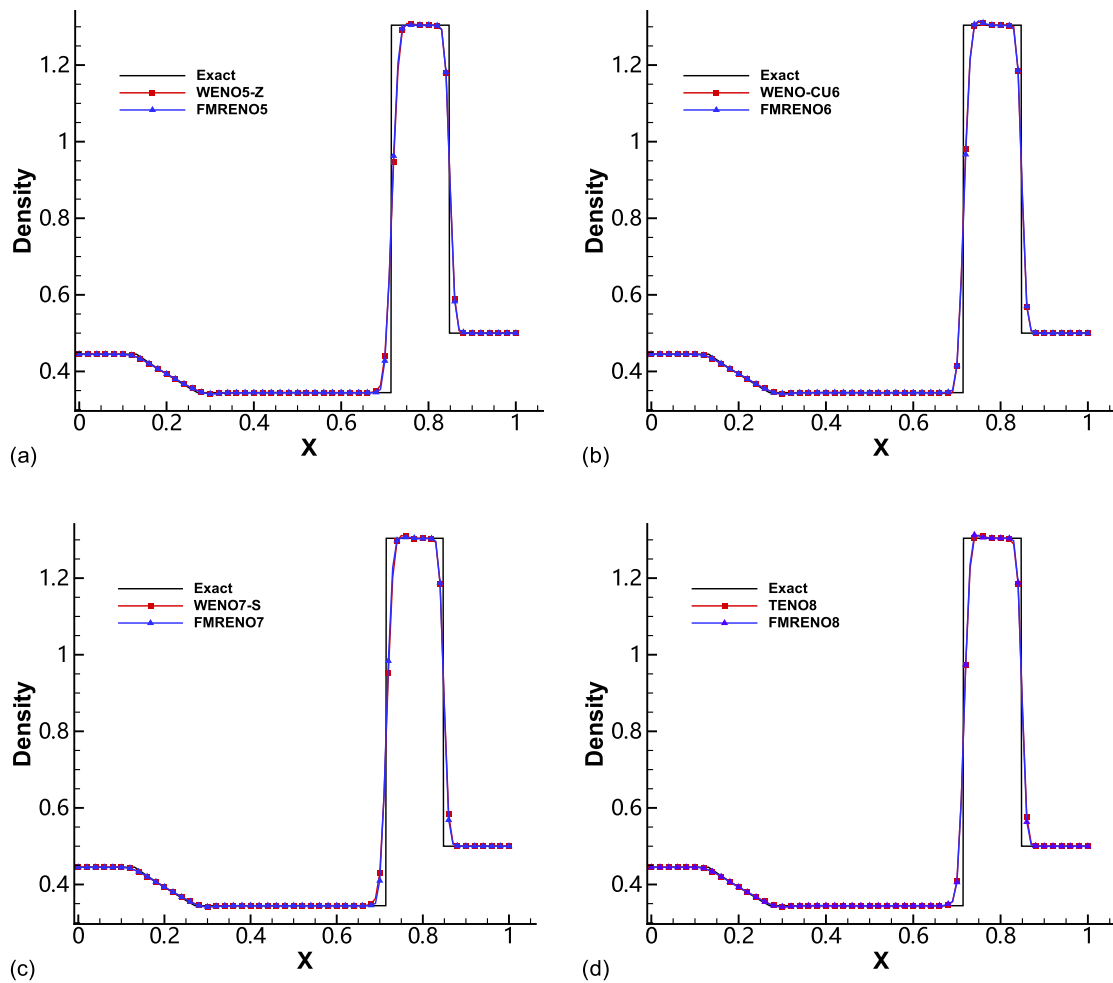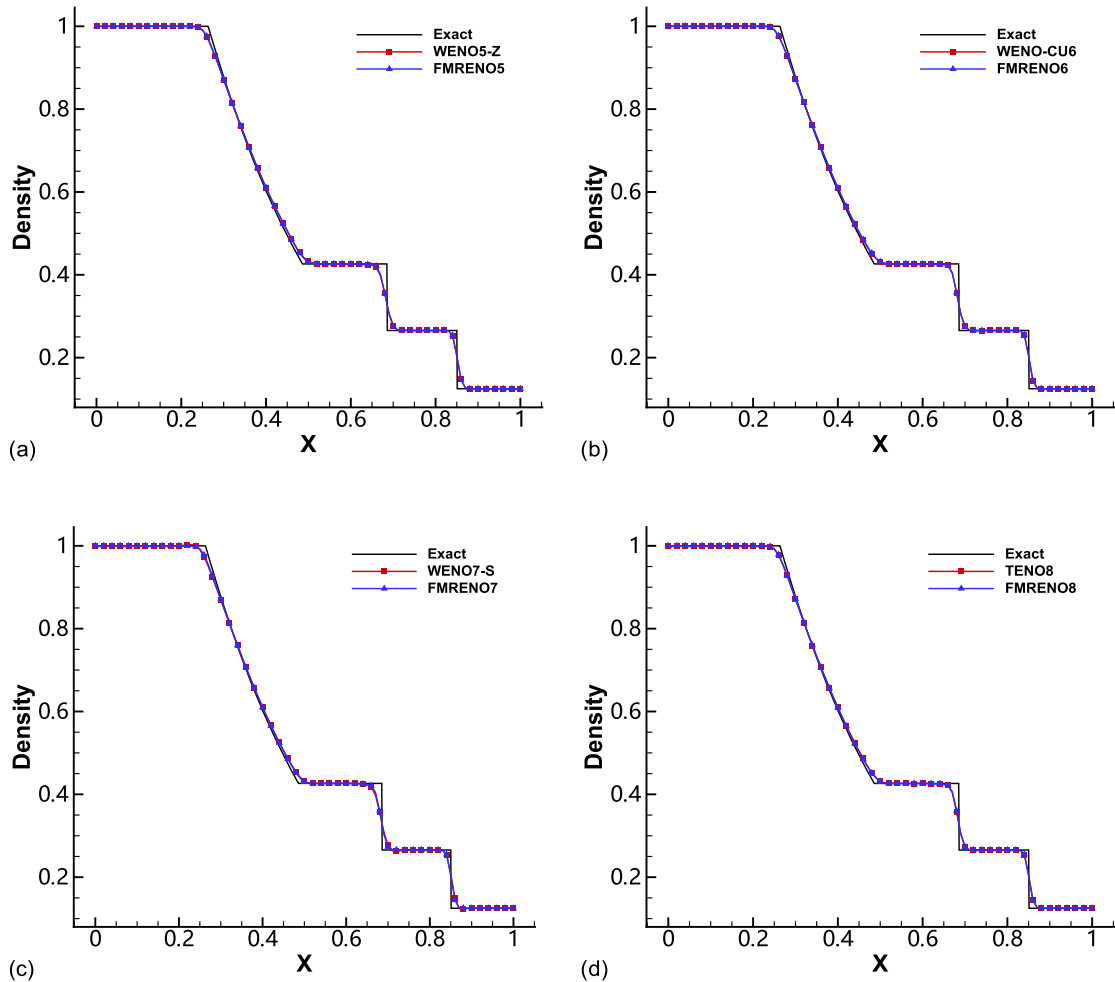
Fig. 7 Lax's problem: solutions from the WENO5-Z, WENO-CU6, WENO7-S, TENO8, and FMRENO schemes. Discretization is on 100 uniformly distributed grid points and the final simulation time is $t = 0.14$

and the final simulation time is $t = 0.14$.

The initial condition for Sod's problem [49] is

$$(\rho, u, p) = \begin{cases} (1, 0, 1), & \text{if } 0 \leq x < 0.5, \\ (0.125, 0, 0.1), & \text{if } 0.5 \leq x \leq 1, \end{cases} \tag{35}$$

and the final simulation time is $t = 0.2$. Both computations are performed on 100 uniformly distributed grid points.

As shown in Figs. 7 and 8, for both problems, the proposed FMRENO schemes show good shock-capturing properties. In addition, the efficiency improvement based on the scheme reconstruction time (referred to as Efficiency improvement 1) and that based on the total CPU computation time (referred to as Efficiency improvement 2) with FMRENO schemes are shown in Table 11. The results show that the computational time of FMRENO schemes only varies slightly when the present framework is extended to very-high-order reconstructions, whereas that of the standard high-order W/TENO schemes increases remarkably due to the expensive evaluations of the smoothness indicators.

Fig. 8 Sod's problem: solutions from the WENO5-Z, WENO-CU6, WENO7-S, TENO8, and FMRENO schemes. Discretization is on 100 uniformly distributed grid points and the final simulation time is $t = 0.2$

5.3 Shock Density-Wave Interaction Problem

This case is proposed by Shu and Osher [50]. A one-dimensional Mach-3 shock wave interacts with a perturbed density field generating both small-scale structures and discontinuities. The initial condition is

$$(\rho, u, p) = \begin{cases} (3.857, 2.629, 10.333), & \text{if } 0 \leq x < 1, \\ (1 + 0.2\sin(5(x-5)), 0, 1), & \text{if } 1 \leq x \leq 10. \end{cases} \tag{36}$$

The computational domain is [0,10] with $N = 200$ uniformly distributed mesh cells and the final evolution time is $t = 1.8$. The inflow boundary condition and outflow boundary condition are applied at $x = 0$ and $x = 10$, respectively. The "exact" solution for reference is obtained by the fifth-order WENO5-JS scheme with $N = 2000$.

The computed density profiles from the WENO5-Z, WENO-CU6, WENO7-S, TENO8, and FMRENO schemes are given by Fig. 9. For the five-point schemes, the FMRENO schemes show obvious improvement with regard to resolving the high-wavenumber fluctuations when compared to the corresponding WENO5-Z schemes. For the six-, seven-, and eight-point schemes, compared with WENO-CU6, WENO7-S, and TENO8, the present FMRENO schemes perform better in capturing the shocklets and maintaining the wave amplitude, except in the vicinity of $x = 6$.

Table 11 Averaged computational time for various reconstruction schemes and the corresponding efficiency improvements

Cases	Schemes	Reconstruction time (s)	Total CPU computation time (s)	Efficiency improvement 1 (%)	Efficiency improvement 2 (%)
Sod's problem	WENO5-Z	0.040	0.142	–	–
	FMRENO5	0.042	0.153	**−4.91**	**−7.71**
	WENO-CU6	0.051	0.158	–	–
$N = 100$	FMRENO6	0.041	0.148	**18.15**	**6.74**
	WENO7-S	0.049	0.172	–	–
	FMRENO7	0.043	0.168	**13.12**	**2.04**
	TENO8	0.092	0.214	–	–
	FMRENO8	0.041	0.156	**55.10**	**26.93**

Efficiency comparisons between various schemes are given in Table 12. All the proposed schemes show an efficiency improvement when compared to the corresponding classical W/TENO schemes of the same accuracy order.

5.4 Interacting Blast Waves

The two-blast-waves interaction problem taken from [51] is considered. The initial condition is

$$(\rho, u, p) = \begin{cases} (1, 0, 1000), & \text{if } 0 \le x < 0.1, \\ (1, 0, 0.01), & \text{if } 0.1 \le x < 0.9, \\ (1, 0, 100), & \text{if } 0.9 \le x \le 1. \end{cases} \tag{37}$$

The computational domain is [0,1], and symmetry boundary conditions are applied at $x = 0$ and $x = 1$, respectively. The simulation is performed on a uniform mesh with $N = 400$ and the final simulation time is $t = 0.038$. The "exact" solution for reference is computed by the fifth-order WENO5-JS scheme on a uniform mesh with $N = 2000$. For this case, the Roe scheme with entropy-fix is employed for flux splitting.

As shown in Fig. 10, while WENO7-S fails this case as reported by [37] due to the lack of numerical robustness, the results from all other considered schemes agree well with the reference solution. Moreover, the FMRENO5 and FMRENO6 schemes perform better than WENO5-Z and WENO-CU6 in resolving the density peak at $x = 0.78$, respectively.

Efficiency comparisons between various schemes are given in Table 13 and the efficiency improvement from the present schemes is substantial.
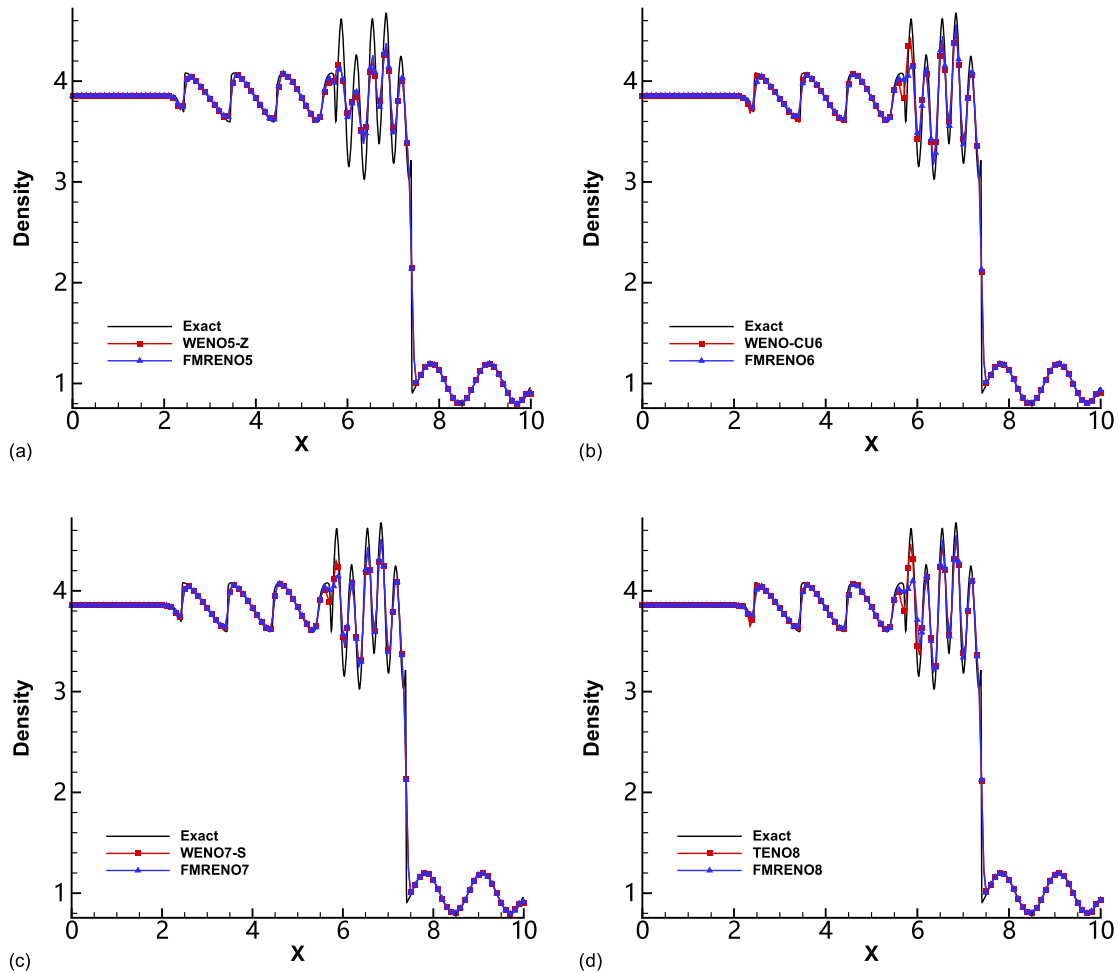
Fig. 9 Shock density-wave interaction problem: solutions from the WENO5-Z, WENO-CU6, WENO7-S, TENO8, and FMRENO schemes. Discretization is on 200 uniformly distributed grid points and the final simulation time is $t = 1.8$

5.5 Rayleigh–Taylor Instability

The inviscid Rayleigh-Taylor instability case proposed by Xu and Shu [52] is considered here. The initial condition is

$$(\rho, u, v, p) = \begin{cases} (2, 0, -0.025c\cos(8\pi x), 1 + 2y), & \text{if } 0 \le y < 1/2, \\ (1, 0, -0.025c\cos(8\pi x), y + 3/2), & \text{if } 1/2 \le y \le 1, \end{cases} \tag{38}$$

where the sound speed $c = \sqrt{\gamma \frac{p}{\rho}}$ with $\gamma = \frac{5}{3}$. The computational domain is $[0, 0.25] \times [0, 1]$. Reflective boundary conditions are imposed at the left and right sides of the domain. Constant primitive variables $(\rho, u, v, p) = (2, 0, 0, 1)$ and $(\rho, u, v, p) = (1, 0, 0, 2.5)$ are set for the bottom and top boundaries, respectively.

The computed density contours with the FMRENO and various W/TENO schemes at a resolution of 120×480 are shown in Fig. 11. It is observed that the newly proposed FMRENO5 and FMRENO7 schemes resolve finer small-scale structures than WENO5-Z and WENO7-S, respectively. On the other hand, the FMRENO6 and FMRENO8 schemes perform similarly to WENO-CU6 and TENO8.

Table 12 Averaged computational time for various reconstruction schemes and the corresponding efficiency improvements

Cases	Schemes	Reconstruction time (s)	Total CPU computation time (s)	Efficiency improvement 1 (%)	Efficiency improvement 2 (%)
Shock/ density wave interaction $N = 200$	WENO5-Z	0.295	1.008	–	–
	FMRENO5	0.287	1.007	**2.51**	**0.12**
	WENO-CU6	0.330	1.063	–	–
	FMRENO6	0.293	1.015	**11.08**	**4.50**
	WENO7-S	0.335	1.182	–	–
	FMRENO7	0.302	1.165	**9.80**	**1.43**
	TENO8	0.597	1.510	–	–
	FMRENO8	0.313	1.179	**47.52**	**21.88**

As shown in Table 14, a substantial efficiency improvement can be observed for all the considered FMRENO schemes when compared to classical W/TENO schemes of the same accuracy order.

5.6 Riemann Problem: Configuration 3

Two-dimensional Riemann (2D) problems, first proposed in [53], are classical benchmark cases for verifying numerical methods by solving the Euler equations. Here, we consider the 2D Riemann problem of configuration 3. The computational domain is $[0, 1] \times [0, 1]$ and the final simulation time is $t = 0.3$. The initial condition is given as

$$(\rho, p, u, v) = \begin{cases} (0.5323, 0.300, 1.206, 0.000), & \text{if } 0.0 < x < 0.5, 0.5 < y < 1.0, \\ (1.5000, 1.500, 0.000, 0.000), & \text{if } 0.5 < x < 1.0, 0.5 < y < 1.0, \\ (0.1380, 0.029, 1.206, 1.206), & \text{if } 0.0 < x < 0.5, 0.0 < y < 0.5, \\ (0.5323, 0.300, 0.000, 1.206), & \text{if } 0.5 < x < 1.0, 0.0 < y < 0.5. \end{cases} \quad (39)$$

As shown in Figs. 12 and 13, the FMRENO5, FMRENO6, and FMRENO7 schemes capture the shockwave patterns, and the small-scale flow structures better than WENO5-Z, WENO-CU6 and WENO7-S, respectively. For the eight-point schemes, the present FMRENO8 scheme is a bit more dissipative and at the same time generates less spurious numerical noise than the standard TENO8 scheme.

Efficiency comparisons between various schemes have been given in Table 15. Except for the five-point schemes, the present schemes show a much better efficiency in terms of both criteria.
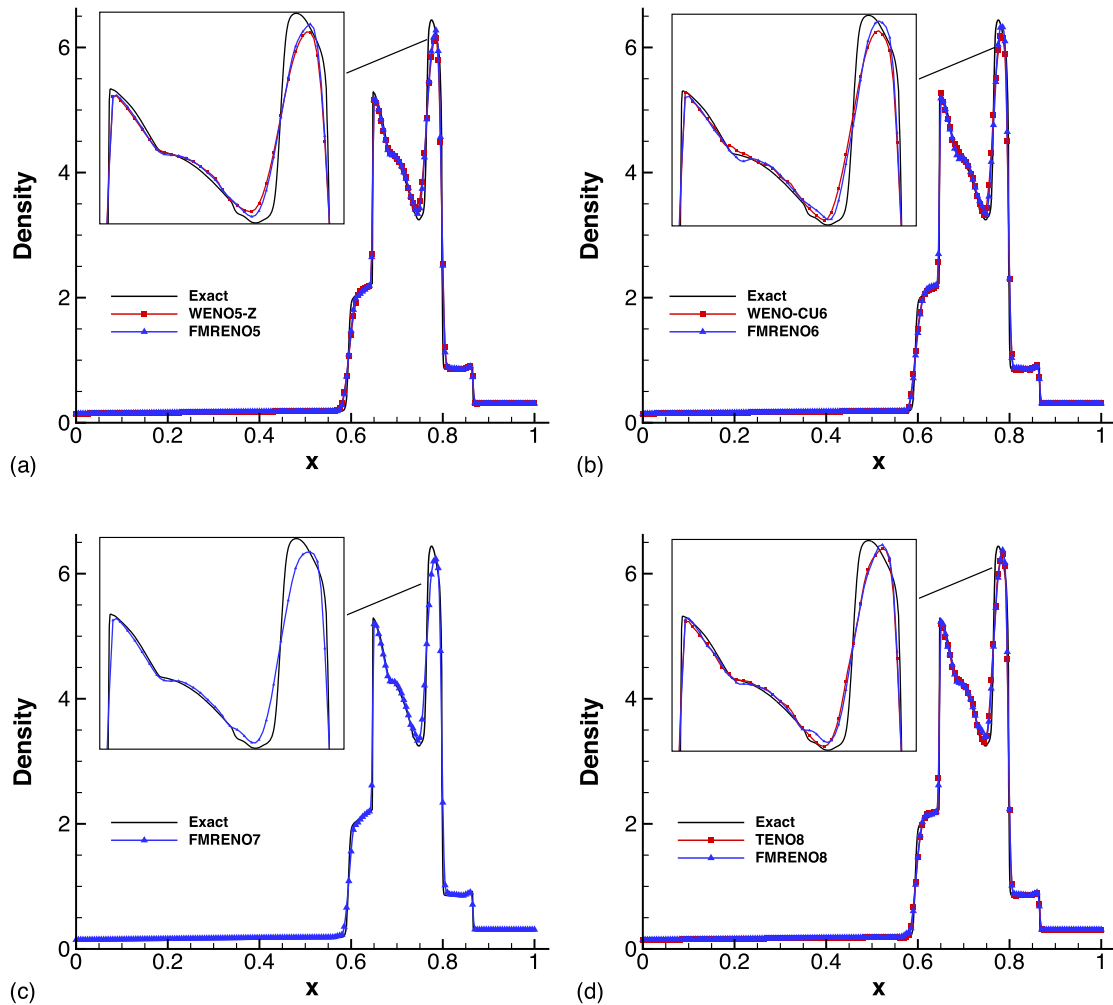
Fig. 10 Interacting blast waves problem: solutions from the WENO5-Z, WENO-CU6, TENO8, and FMRENO schemes. Discretization is on 400 uniformly distributed grid points and the final simulation time is $t = 0.038$. WENO7-S also fails due to the lack of numerical robustness as reported by [37]

5.7 Riemann Problem: Configuration 6

The 2D Riemann problem of configuration 6 is considered. The computational domain is $[0, 1] \times [0, 1]$ and the final simulation time is $t = 0.3$. The initial condition is given as

$$(\rho, u, v, p) = \begin{cases} (2.0, 0.75, 0.5, 1.0), & \text{if } 0.0 < x < 0.5, 0.5 < y < 1.0, \\ (1.0, 0.75, -0.5, 1.0), & \text{if } 0.5 < x < 1.0, 0.5 < y < 1.0, \\ (1.0, -0.75, 0.5, 1.0), & \text{if } 0.0 < x < 0.5, 0.0 < y < 0.5, \\ (3.0, -0.75, -0.5, 1.0), & \text{if } 0.5 < x < 1.0, 0.0 < y < 0.5. \end{cases} \tag{40}$$

As shown in Figs. 14 and 15, the performance of the present FMRENO schemes is much better than that of the corresponding W/TENO schemes in terms of capturing the interfacial instabilities. It is worth noting that the solution of FMRENO8 is free from the numerical noise generated by TENO8.

Efficiency comparisons between various schemes have been given in Table 16. Overall speaking, the efficiency improvement from the present schemes increases remarkably as the reconstruction order increases.
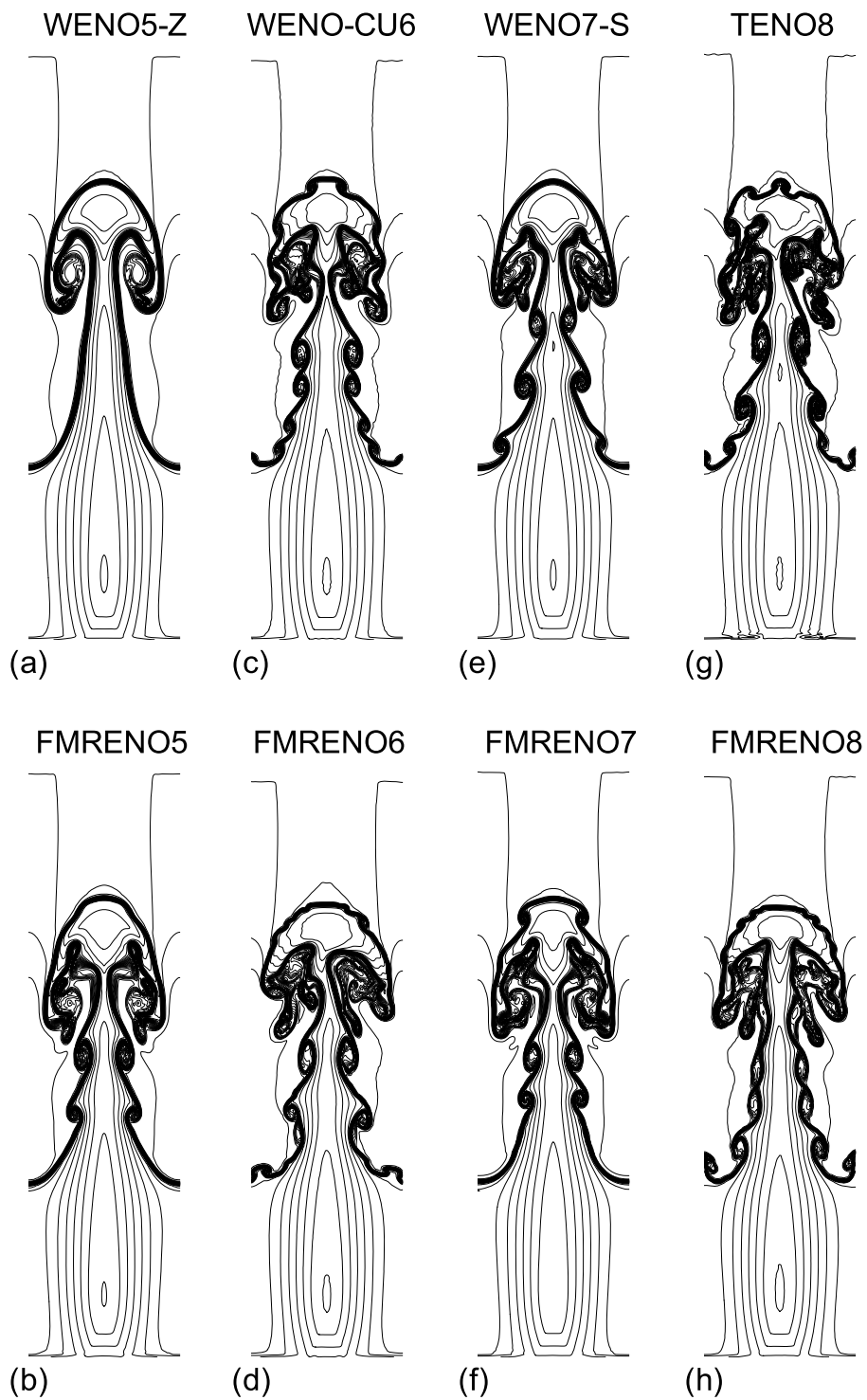
Fig. 11 Rayleigh–Taylor instability problem: solutions from the WENO5-Z, WENO-CU6, WENO7-S, TENO8, and FMRENO schemes. Resolution is 120×480, and the final simulation time is $t = 1.95$

Table 13 Averaged computational time for various reconstruction schemes and the corresponding efficiency improvements

Cases	Schemes	Reconstruction time (s)	Total CPU computation time (s)	Efficiency improvement 1 (%)	Efficiency improvement 2 (%)
Interacting blast waves $N = 400$	WENO5-Z	2.123	6.557	–	–
	FMRENO5	1.966	6.430	**7.39**	**1.95**
	WENO-CU6	2.540	7.138	–	–
	FMRENO6	2.157	6.574	**15.06**	**7.90**
	WENO7-S	–	–	–	–
	FMRENO7	2.131	7.420	–	–
	TENO8	4.289	9.855	–	–
	FMRENO8	2.229	7.446	**48.03**	**24.45**

Table 14 Averaged computational time for various reconstruction schemes and the corresponding efficiency improvements

Cases	Schemes	Reconstruction time (s)	Total CPU computation time (s)	Efficiency improvement 1 (%)	Efficiency improvement 2 (%)
Rayleigh-Taylor instability 120×480	WENO5-Z	1593.90	3826.97	–	–
	FMRENO5	1398.24	3402.42	**12.28**	**11.09**
	WENO-CU6	2350.64	4343.55	–	–
	FMRENO6	1600.40	3591.29	**31.92**	**17.32**
	WENO7-S	2736.94	4859.31	–	–
	FMRENO7	1438.90	3527.78	**47.43**	**27.40**
	TENO8	3733.35	5975.54	–	–
	FMRENO8	1732.64	3882.27	**53.59**	**35.03**

5.8 Double Mach Reflection of a Strong Shock

This 2D case is taken from Woodward and Colella [51] with the initial condition as

$$(\rho, u, v, p) = \begin{cases} (1.4, 0, 0, 1), & \text{if } y < 1.732(x - 0.1667), \\ (8, 7.145, -4.125, 116.8333), & \text{otherwise.} \end{cases} \quad (41)$$
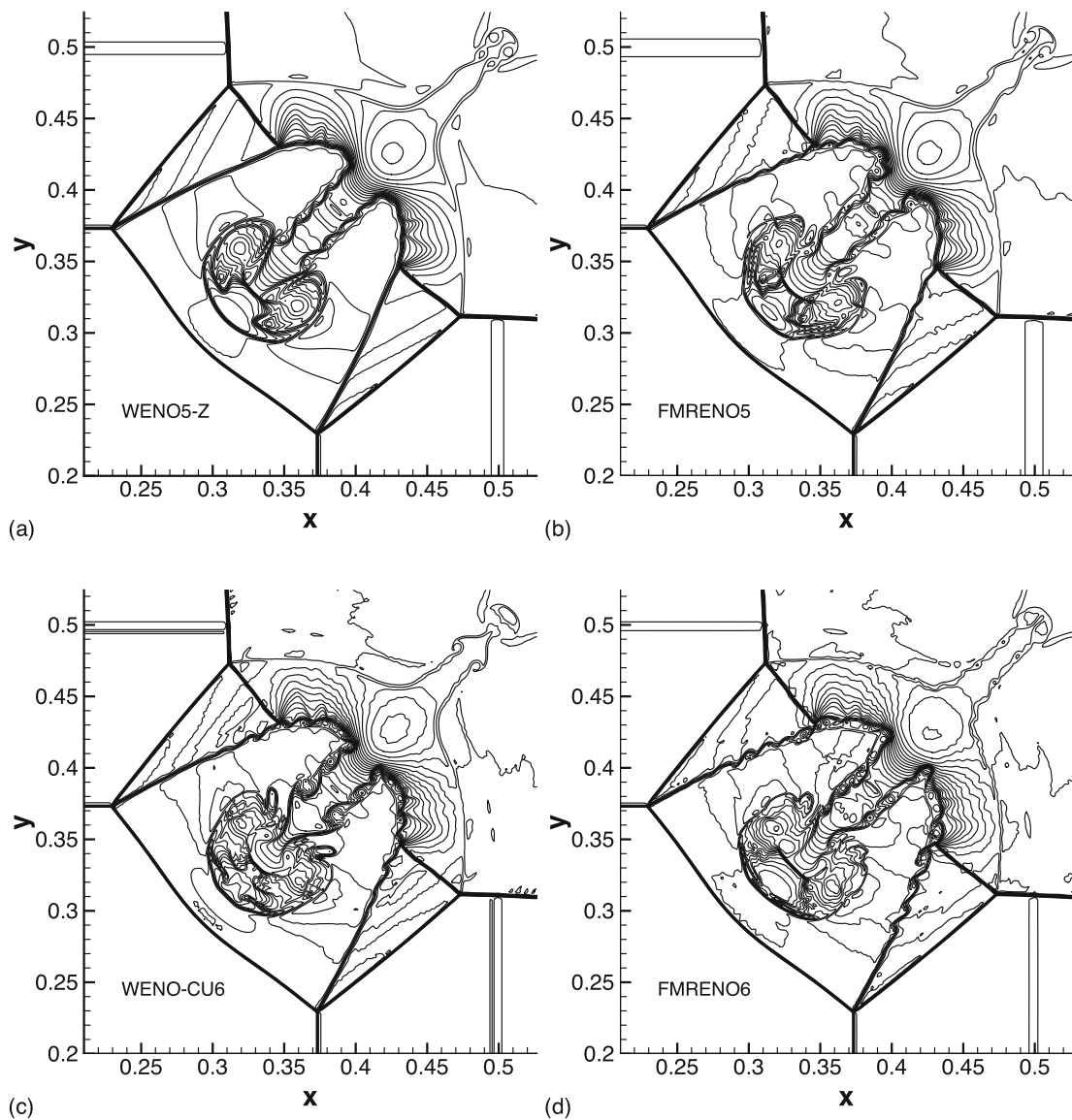
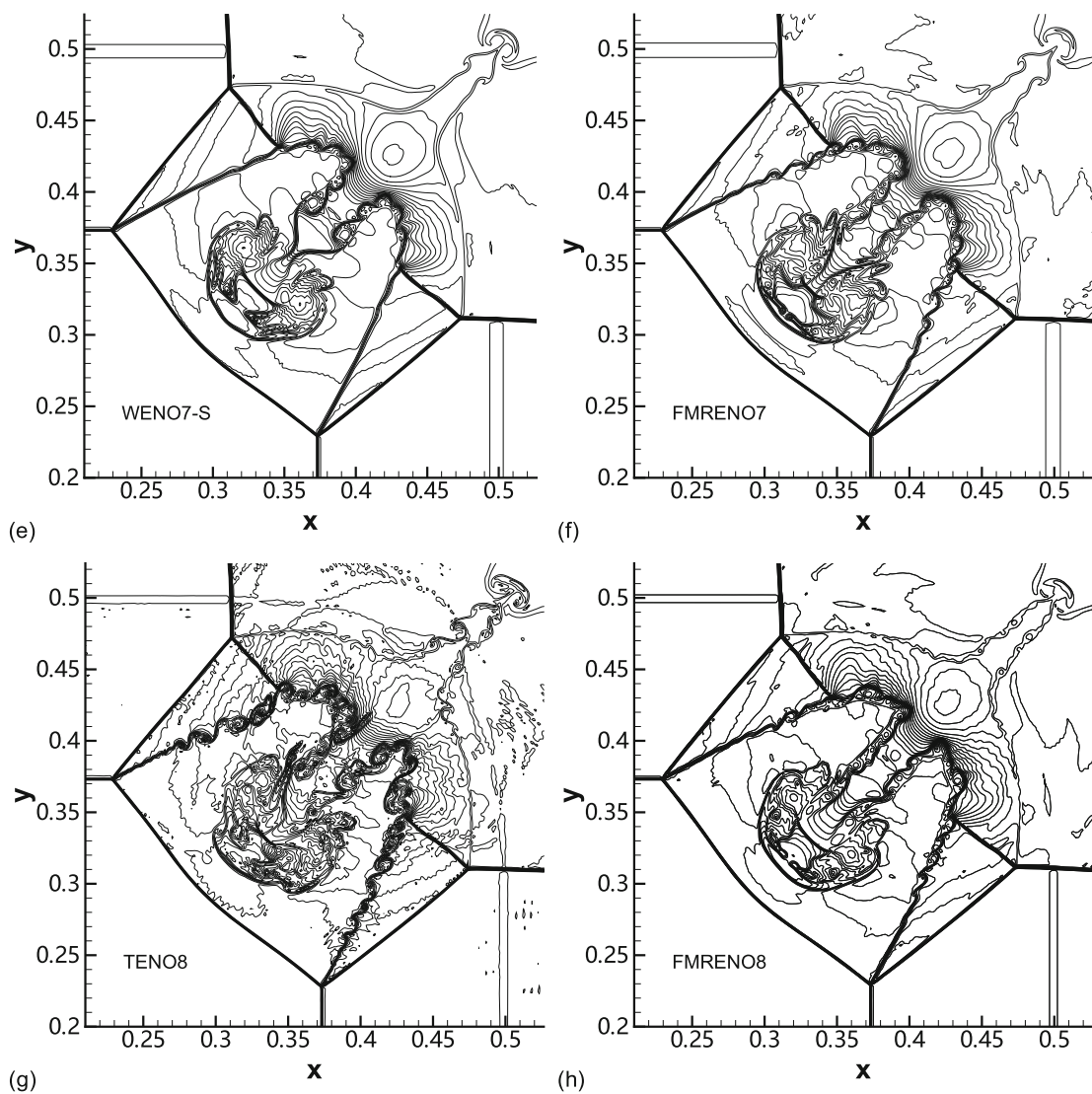**Fig. 12** 2D Riemann problem of configuration 3: solutions from the WENO5-Z, WENO-CU6, FMRENO5, and FMRENO6 schemes. The simulation time is $t = 0.3$ and the grid resolution is 1200×1200. This figure is drawn with 30 density contours between 0.2 and 1.8

The computational domain is $[0, 4] \times [0, 1]$ and the final simulation time is $t = 0.2$. Initially, a right-moving Mach 10 shock wave is placed at $x = 0.1667$ with an incident angle of $60°$ to the x-axis. The post-shock condition is imposed from $x = 0$ to $x = 0.1667$ whereas a reflecting wall condition is enforced from $x = 0.1667$ to $x = 4$ at the bottom. For the top boundary condition, the fluid variables are defined to exactly describe the evolution of the Mach 10 shock wave. The inflow and outflow conditions are imposed for the left and right sides of the computational domain. The computed density contours are shown in Figs. 16 and 17. For the five-, six- and eight-point reconstructions, the present FMRENO schemes perform similarly to or slightly better than the corresponding W/TENO schemes. On the other hand, the seven-point FMRENO7 scheme performs significantly better than WENO7-S in resolving the small-scale vortical structures in the blow-up regions.
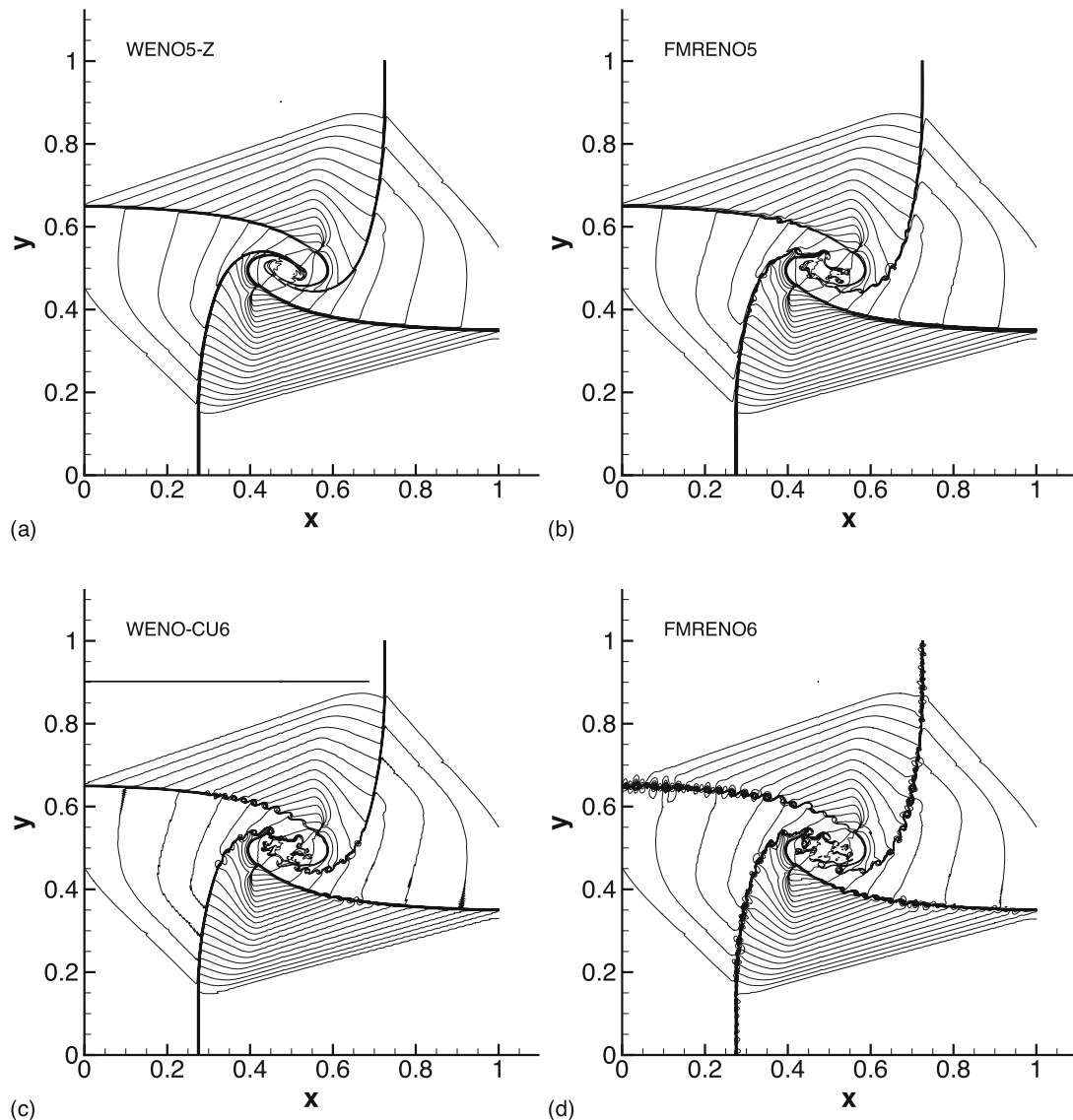
Fig. 13 2D Riemann problem of configuration 3 (continued): solutions from the WENO7-S, TENO8, FMRENO7, and FMRENO8 schemes. The simulation time is $t = 0.3$ and the grid resolution is 1200×1200. This figure is drawn with 30 density contours between 0.2 and 1.8

Moreover, it is worth noting that the effect of the MP limiter can be adjusted by tuning the curvature measurement $d_{i+1/2}^{\text{M4}}$ and the parameters α, β. In the following, we test the dissipation property of FMRENO8 with a more restrictive curvature measurement $d_{i+1/2}^{\text{4M}}$ at the cell interface $i + 1/2$ which is defined as

$$d_{i+1/2}^{\text{M4}} = \text{minmod}(4d_i - d_{i+1}, 4d_{i+1} - d_i, d_i, d_{i+1}). \tag{42}$$

As shown in Figs. 17h and 18c, a more restrictive curvature measurement will tighten the MP-based regularity criterion, which results in a more dissipative FMRENO8 scheme. In Fig. 18a, d, the dissipation property changes with the parameter β, which determines the amount of freedom allowing for large curvature. And Fig. 18b, d show that, a larger α results in a less dissipative FMRENO8 scheme.

Efficiency comparisons between various schemes are given in Table 17. The efficiency improvements from the present schemes of the same accuracy order are remarkable.

Table 15 Averaged computational time for various reconstruction schemes and the corresponding efficiency improvements (the simulation resolution is 400×400)

Cases	Schemes	Reconstruction time (s)	Total CPU computation time (s)	Efficiency improvement 1 (%)	Efficiency improvement 2 (%)
Riemann problem 3 400×400	WENO5-Z	504.94	1308.76	–	–
	FMRENO5	621.39	1425.99	**−23.06**	**−8.86**
	WENO-CU6	973.74	1786.28	–	–
	FMRENO6	653.82	1472.10	**32.85**	**17.59**
	WENO7-S	821.50	1682.07	–	–
	FMRENO7	657.02	1550.46	**20.02**	**7.82**
	TENO8	1580.06	2501.81	–	–
	FMRENO8	695.15	1585.24	**56.01**	**36.64**

Table 16 Averaged computational time for various reconstruction schemes and the corresponding efficiency improvements (the simulation resolution is 400×400)

Cases	Schemes	Reconstruction time (s)	Total CPU computation time (s)	Efficiency improvement 1 (%)	Efficiency improvement 2 (%)
Riemann problem 6 400×400	WENO5-Z	413.06	1058.35	–	–
	FMRENO5	493.69	1137.27	**−19.51**	**−7.46**
	WENO-CU6	778.65	1440.18	–	–
	FMRENO6	531.74	1192.61	**31.71**	**17.19**
	WENO7-S	668.77	1379.46	–	–
	FMRENO7	515.18	1217.01	**22.97**	**11.78**
	TENO8	1248.04	1979.51	–	–
	FMRENO8	576.29	1302.32	**53.82**	**34.21**

5.9 Single-Material Triple Point Problem

A modified triple point problem with a single material rather than multiple materials is presented [54]. The computational domain is $[0, 7] \times [0, 3]$ and the initial condition is shown in Fig. 19. An outflow condition is applied to the right boundary while a slip-wall condition for all other boundaries. A uniform mesh with the resolution of 1120×480 is employed for all computations.
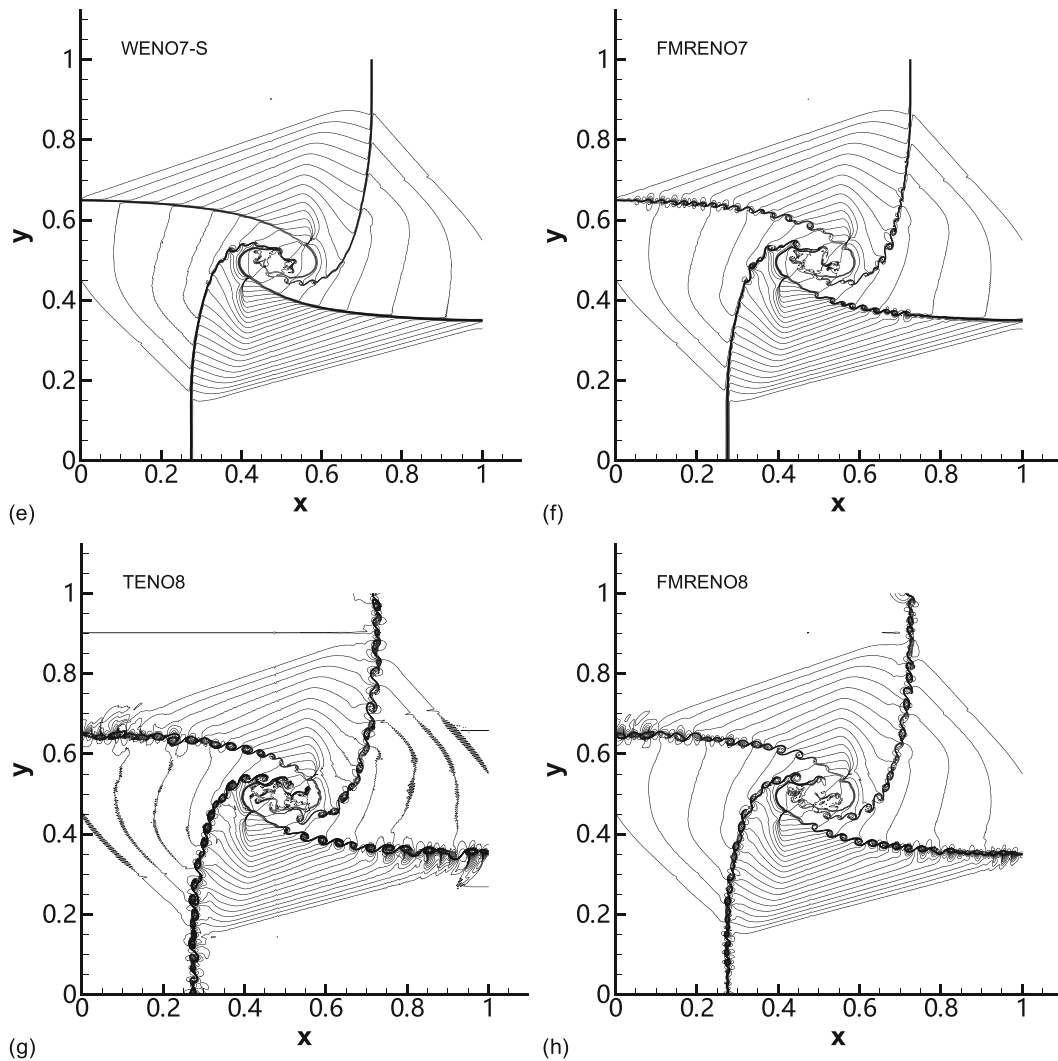
Fig. 14 2D Riemann problem of configuration 6: solutions from the WENO5-Z, WENO-CU6, FMRENO5, and FMRENO6 schemes. The simulation time is $t = 0.3$ and the grid resolution is 1200×1200. This figure is drawn with 30 density contours between 0.24 and 3.3

As shown in Fig. 20, the present FMRENO schemes generate finer small-scale structures in the roll-up regions and along the contact discontinuities than the corresponding WENO5-Z, WENO-CU6, and WENO7-S schemes, respectively. Also as shown by Fig. 21, FMRENO8 further improves the performance of the lower-order FMRENO schemes while the standard TENO8 scheme fails this case in the high-resolution simulation with 1120×480 because of the positivity-preserving issue.

Efficiency comparisons between various schemes have been given in Table 18. For very-high-order reconstructions, the efficiency improvements from the present schemes of the same accuracy order are remarkable for both criteria.

Fig. 15 2D Riemann problem of configuration 6 (continued): solutions from the WENO7-S, TENO8, FMRENO7, and FMRENO8 schemes. The simulation time is $t = 0.3$ and the grid resolution is 1200×1200. This figure is drawn with 30 density contours between 0.24 and 3.3

5.10 Regular Shock Reflection

The regular shock reflection is a typical two-dimensional steady flow [55]. The computational domain is $[0, 4] \times [0, 1]$. Initially, an impinging shock with impinging angle θ of 29° and upstream flow of Mach number 2.9 is imposed by the Rankine–Hugoniot relationship [56]. The evolution histories of the averaged residue for the various schemes are analyzed. Here, the averaged residue is defined as

$$Res_A = \sum_{i=1}^{N} \frac{|R_i|}{N}, \tag{43}$$

where R_i is the local residue defined as

$$R_i = \frac{\rho_i^{n+1} - \rho_i^n}{\delta t}, \tag{44}$$

and N is the total number of grid points, and n denotes the time step.
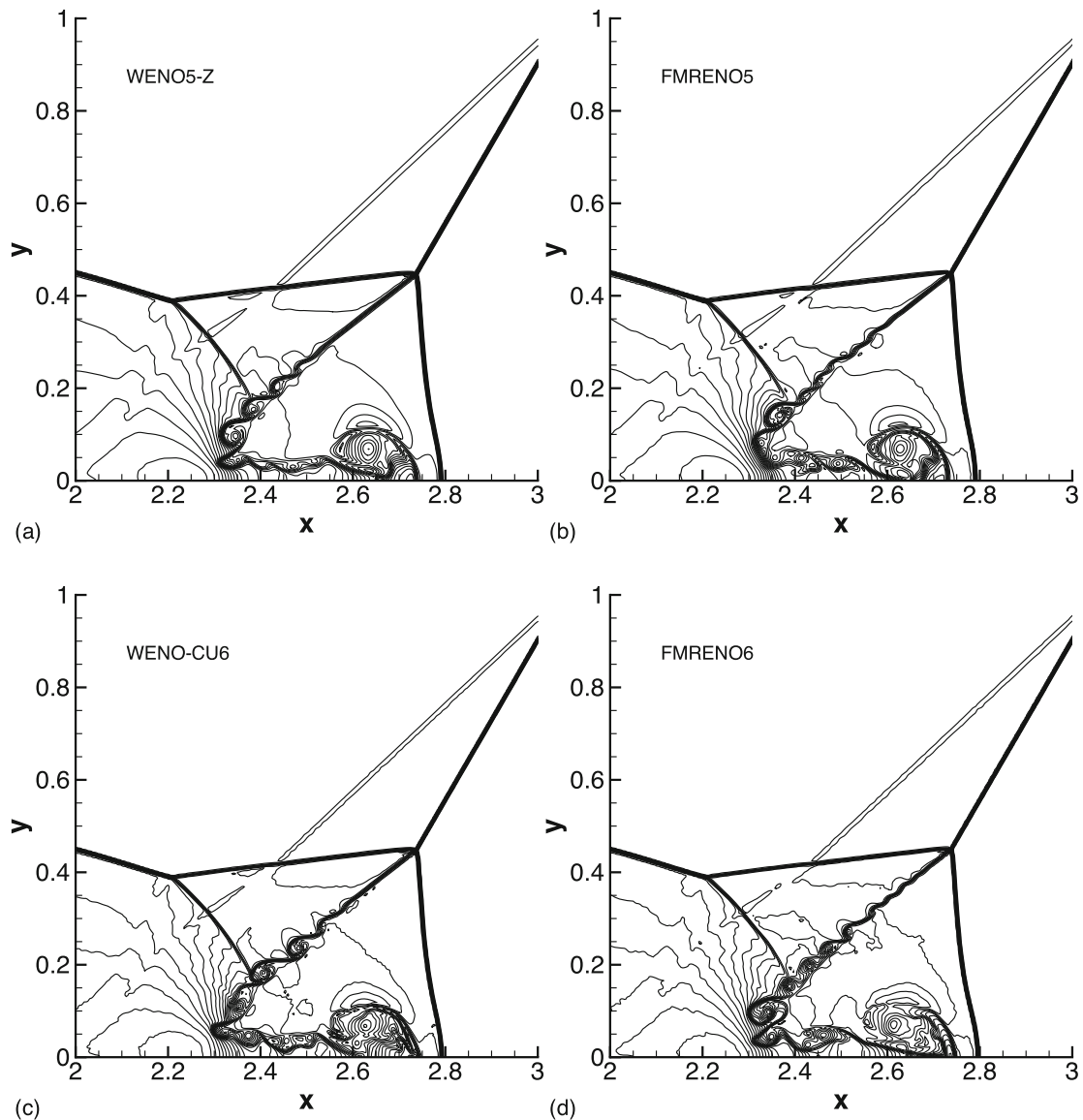
Fig. 16 Double Mach reflection of a strong shock: zoomed-in views of density contours from the WENO5-Z, WENO-CU6, FMRENO5, and FMRENO6 schemes at the simulation time $t = 0.2$. The grid resolution is 1280×320. This figure is drawn with 42 density contours between 1.887 and 20.9

The computed density distributions are shown with 20 contours between 0.98 and 2.7 in Fig. 22. The results show that the numerical oscillations of WENO-CU6 and TENO8 are more severe than those of WENO5-Z. This can be seen more clearly in Fig. 23. The averaged residue of WENO5-Z settles down to the smallest value around $10^{-2.8}$, followed by that of WENO7-S which settles down to a value around $10^{-2.0}$. The averaged residues of WENO-CU6 and TENO8 decrease to a relatively larger value, which is around $10^{-1.7}$ and $10^{-0.9}$, respectively. For the newly proposed five-, six-, seven-, and eight-point FMRENO schemes, the averaged residue settles down to a value around $10^{-2.8}$, $10^{-2.2}$, $10^{-2.6}$ and $10^{-2.4}$, respectively. These results clearly show that the FMRENO5 scheme has a comparable convergence behavior with WENO5-Z. When comparing with the low-dissipation WENO-CU6, WENO7-S, and TENO8 schemes, the present FMRENO6, FMRENO7, and FMRENO8 schemes show better convergence behavior.
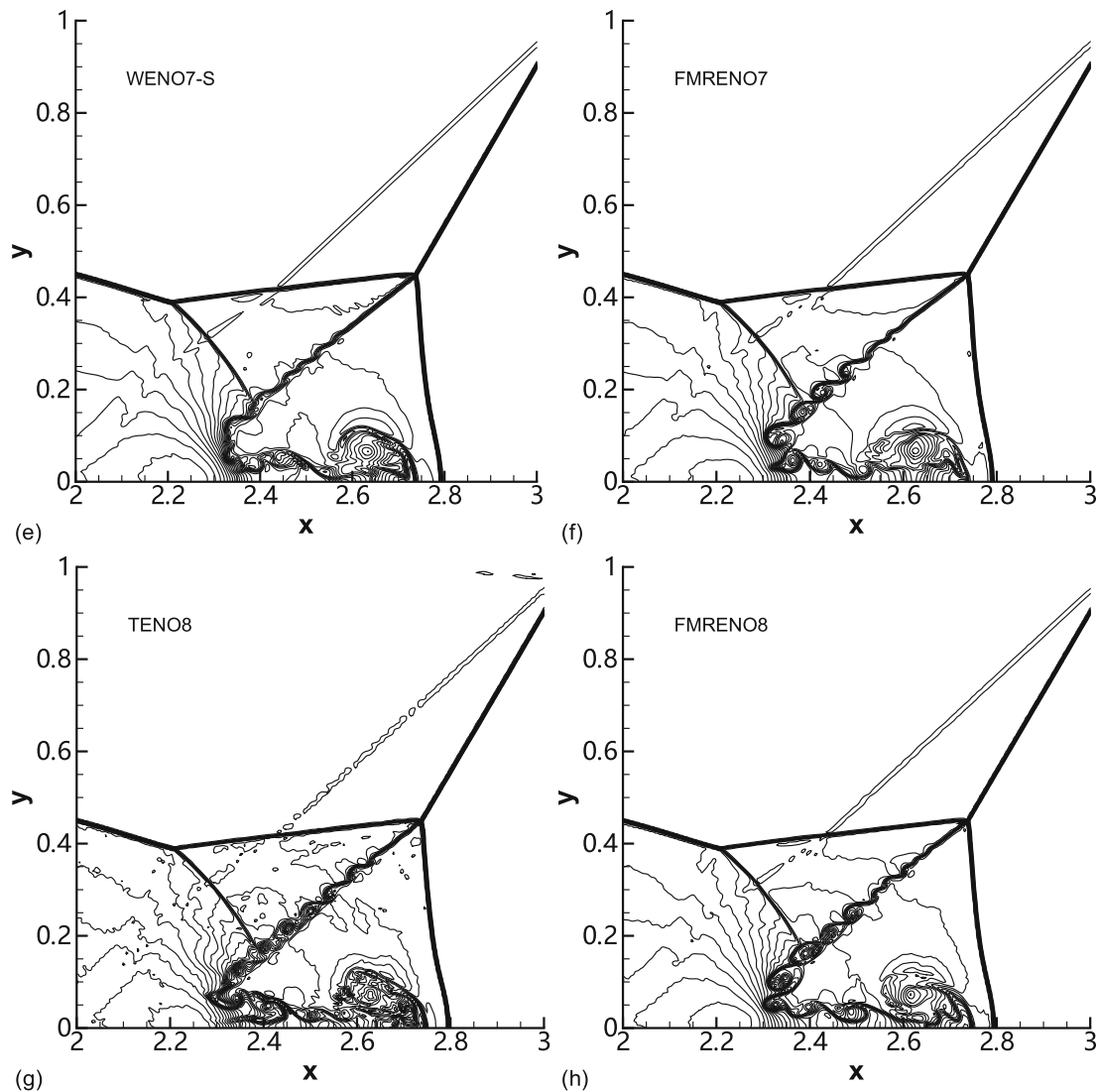
Fig. 17 Double Mach reflection of a strong shock (continued): zoomed-in views of density contours from the WENO7-S, TENO8, FMRENO7, and FMRENO8 schemes at the simulation time $t = 0.2$. The grid resolution is 1280×320. This figure is drawn with 42 density contours between 1.887 and 20.9

6 Conclusions

In this work, a new family of high-order shock-capturing FMRENO schemes has been proposed. The major contributions are summarized as follows:

- Based on the MP concept, the construction of the new FMRENO schemes consists of three main phases, i.e., (1) preparing polynomial-based candidate stencils from high- to low-orders in a hierarchical manner; (2) providing a local regularity criterion by calculating the MP upper and lower bounds. A candidate stencil is judged to be smooth only when the reconstructed cell interface flux locates within the MP bounds; (3) formulating the final cell interface reconstruction scheme by selecting the higher-order (or better spectra) candidate stencil, which is judged to be smooth. If all candidate stencils are judged to be nonsmooth by the MP criterion, the smoothest stencil, with which the reconstructed cell interface flux

Fig. 18 Double Mach reflection of a strong shock: zoomed-in views of density contours from FMRENO8 schemes with d_{M4} curvature measurement and various parameters at the simulation time $t = 0.2$. **a** $\alpha = 0.5$ and $\beta = 4.0$; **b** $\alpha = 2.5$ and $\beta = 2.0$; **c** $\alpha = 2.5$ and $\beta = 4.0$; **d** $\alpha = 0.5$ and $\beta = 2.0$. The grid resolution is 1280×320. This figure is drawn with 42 density contours between 1.887 and 20.9
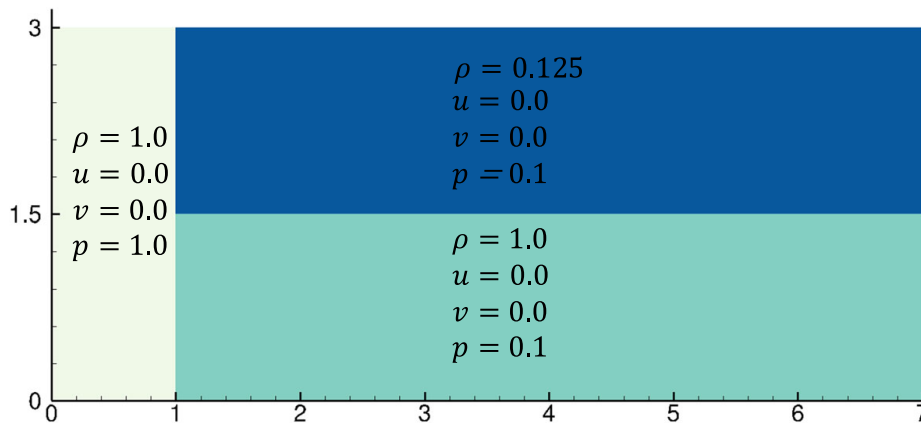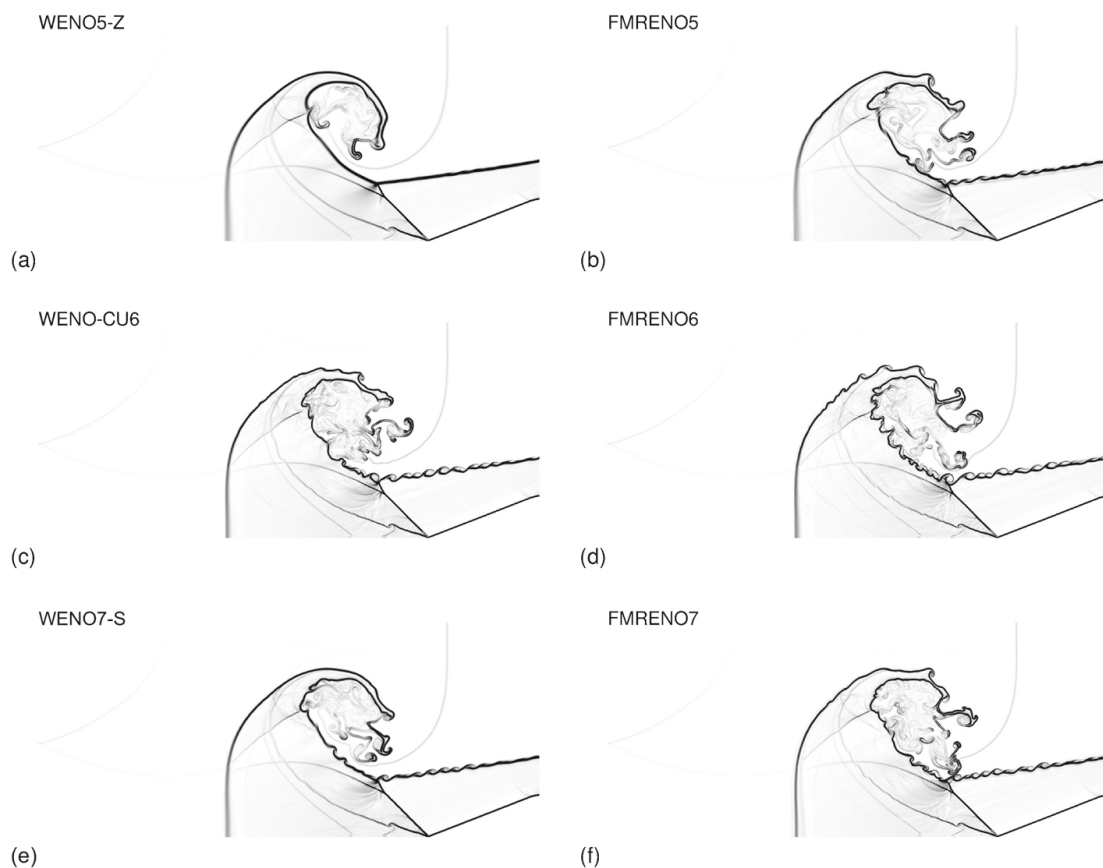

Fig. 19 The sketch of the computational domain and the initial condition for the triple point problem

Table 17 Averaged computational time for various reconstruction schemes and the corresponding efficiency improvements

Cases	Schemes	Reconstruction time (s)	Total CPU computation time (s)	Efficiency improvement 1 (%)	Efficiency improvement 2 (%)
Double Mach reflection 1280×320	WENO5-Z	4832.10	12181.80	–	–
	FMRENO5	4754.20	12052.50	**1.61**	**1.06**
	WENO-CU6	8357.38	15218.60	–	–
	FMRENO6	4938.72	11896.80	**40.91**	**21.83**
	WENO7-S	7515.97	15594.20	–	–
	FMRENO7	5171.17	13308.30	**31.20**	**14.66**
	TENO8	13184.40	20866.50	–	–
	FMRENO8	5328.61	12853.10	**59.59**	**38.40**

WENO5-Z (a)   FMRENO5 (b)

WENO-CU6 (c)   FMRENO6 (d)

WENO7-S (e)   FMRENO7 (f)

Fig. 20 Single-material triple point problem: normalized density gradient contours from the WENO5-Z, WENO-CU6, WENO7-S, and various FMRENO schemes at the simulation time $t = 5$. The grid resolution is 1120×480. This figure is drawn with 19 normalized density gradient contours between 0.05 and 1.95.

FMRENO8
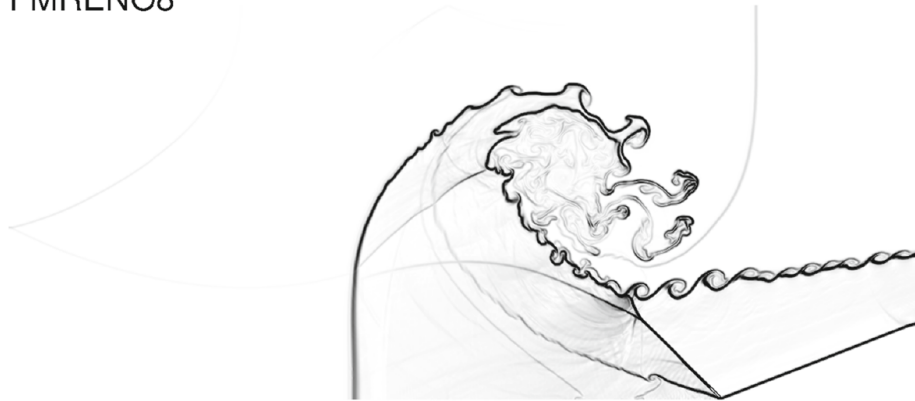
Fig. 21 Single-material triple point problem (continued): normalized density gradient contour from the FMRENO8 scheme. Note that the standard TENO8 scheme fails in this case

Table 18 Averaged computational time for various reconstruction schemes and the corresponding efficiency improvements

Cases	Schemes	Reconstruction time (s)	Total CPU computation time (s)	Efficiency improvement 1 (%)	Efficiency improvement 2 (%)
Single-material triple point 1120×480	WENO5-Z	10258.7	25363.6	–	–
	FMRENO5	10972.9	26337.6	**−6.96**	**−3.84**
	WENO-CU6	18709.2	34147.4	–	–
	FMRENO6	12414.3	27341.7	**33.65**	**19.93**
	WENO7-S	21341.8	38338.6	–	–
	FMRENO7	12271.1	29165.3	**42.50**	**23.93**
	TENO8	–	–	–	–
	FMRENO8	13365.7	29745.9	–	–

departs from the MP bounds the least, will be adopted as the final reconstruction scheme.

- The new framework achieves the multi-resolution property by adaptively selecting the targeted reconstruction scheme from the candidate stencils of different orders according to the local flow regularities. Specifically, in smooth regions, the candidate stencil with the largest stencil width will be adopted for restoring the desired high-order accuracy. In the vicinity of discontinuities, the good non-oscillatory property will be achieved by selecting the candidate reconstruction satisfying the MP criterion. For the wave-like structures, the low-dissipation property can be approached by choosing the smooth candidate stencils with higher accuracy order or better spectral properties.

- The present framework can be straightforwardly extended to arbitrarily very-high-order reconstructions with a tiny complexity increase. Compared to the standard
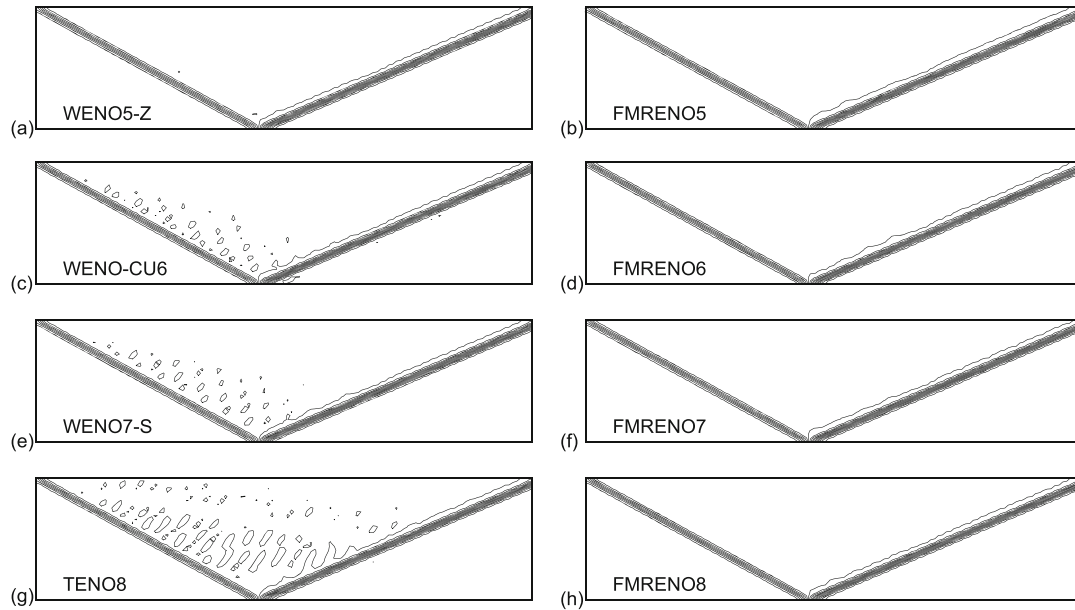
Fig. 22 Regular shock reflection: density contours from the WENO5-Z, WENO-CU6, WENO7-S, TENO8, FMRENO5, FMRENO6, FMRENO7, and FMRENO8 schemes at the simulation time $t = 50$. The grid resolution is 128×32. This figure is drawn with 20 density contours between 0.98 and 2.7
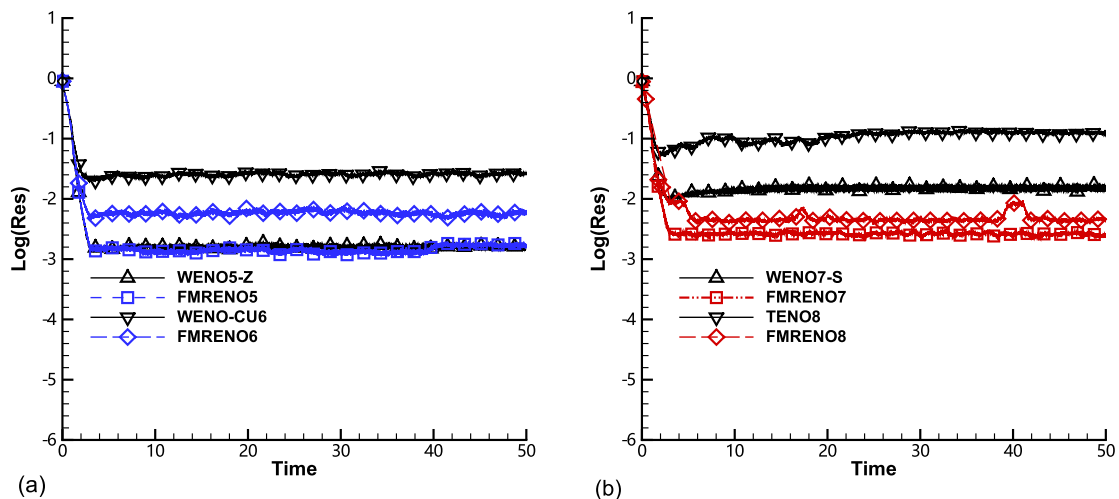

Fig. 23 Regular shock reflection: the evolution histories of the averaged residue with the WENO5-Z, WENO-CU6, WENO7-S, TENO8, FMRENO5, FMRENO6, FMRENO7, and FMRENO8 schemes

W/TENO schemes, the computational efficiency of FMRENO schemes is substantially higher by avoiding the expensive evaluations of the smoothness indicators. Moreover, the efficiency improvement is more impressive with higher-order reconstructions.

- A set of critical benchmark cases is simulated to validate the performance of the proposed FMRENO schemes. Numerical results demonstrate the capability of the new schemes in terms of recovering the targeted high-order accuracy in smooth regions, preserving the low numerical dissipation for resolving wave-like structures, and capturing the discontinuities sharply. In all the considered cases, the present FMRENO schemes show either a similar or an improved performance when compared to the corresponding W/TENO schemes.

Considering the high computational efficiency and the competitive performance of the present FMRENO schemes, future work will focus on the applications to complex geometries and multi-physics problems.

Data Availability The data that support the findings of this study are available on request from the corresponding author, LF.

Declarations

Competing interests The authors declare that they have no known competing financial interests or personal relationships that could have appeared to influence the work reported in this paper.

References

1. Pirozzoli, S.: Numerical methods for high-speed flows. Annu. Rev. Fluid Mech. **43**, 163–194 (2011)
2. Shu, C.-W.: High order weighted essentially nonoscillatory schemes for convection dominated problems. SIAM Rev. **51**, 82–126 (2009)
3. Fu, L., Karp, M., Bose, S.T., Moin, P., Urzay, J.: Shock-induced heating and transition to turbulence in a hypersonic boundary layer. J. Fluid Mech. **909**, A8 (2021)
4. Griffin, K.P., Fu, L., Moin, P.: Velocity transformation for compressible wall-bounded turbulent flows with and without heat transfer. Proc. Natl. Acad. Sci. **118**, e2111144118 (2021)
5. Von, N.J., Richtmyer, R.: A method for the numerical calculation of hydrodynamic shocks. J. Appl. Phys. **21**, 232 (1950)
6. Jameson, A.: Analysis and design of numerical schemes for gas dynamics, 1: artificial diffusion, upwind biasing, limiters and their effect on accuracy and multigrid convergence. Int. J. Comput. Fluid Dyn. **4**, 171–218 (1994)
7. Harten, A.: High resolution schemes for hyperbolic conservation laws. J. Comput. Phys. **49**, 357–393 (1983)
8. Liu, X.D., Osher, S., Chan, T.: Weighted essentially non-oscillatory schemes. J. Comput. Phys. **115**, 200–212 (1994)
9. Jiang, G.S., Shu, C.-W.: Efficient implementation of weighted ENO schemes. J. Comput. Phys. **126**, 202–228 (1996)
10. Fu, L., Hu, X.Y., Adams, N.A.: A family of high-order targeted ENO schemes for compressible-fluid simulations. J. Comput. Phys. **305**, 333–359 (2016)
11. Antoniadis, A.F., Drikakis, D., Farmakis, P.S., Fu, L., Kokkinakis, I., Nogueira, X., Silva, P.A., Skote, M., Titarev, V., Tsoutsanis, P.: UCNS3D: an open-source high-order finite-volume unstructured CFD solver. Comput. Phys. Commun. **279**, 108453 (2022)
12. Tsoutsanis, P., Nogueira, X., Fu, L.: A short note on a 3D spectral analysis for turbulent flows on unstructured meshes. J. Comput. Phys. 111804 (2022)
13. Henrick, A.K., Aslam, T., Powers, J.M.: Mapped weighted essentially non-oscillatory schemes: achieving optimal order near critical points. J. Comput. Phys. **207**, 542–567 (2005)
14. Borges, R., Carmona, M., Costa, B., Don, W.S.: An improved weighted essentially non-oscillatory scheme for hyperbolic conservation laws. J. Comput. Phys. **227**, 3191–3211 (2008)
15. Don, W.-S., Borges, R.: Accuracy of the weighted essentially non-oscillatory conservative finite difference schemes. J. Comput. Phys. **250**, 347–372 (2013)
16. Hill, D.J., Pullin, D.I.: Hybrid tuned center-difference-WENO method for large Eddy simulations in the presence of strong shocks. J. Comput. Phys. **194**, 435–450 (2004)
17. Hu, X., Wang, Q., Adams, N.A.: An adaptive central-upwind weighted essentially non-oscillatory scheme. J. Comput. Phys. **229**, 8952–8965 (2010)
18. Acker, F., Borges, R.D.R., Costa, B.: An improved WENO-Z scheme. J. Comput. Phys. **313**, 726–753 (2016)

19. Suresh, A., Huynh, H.: Accurate monotonicity preserving schemes with Runge–Kutta time stepping. J. Comput. Phys. **136**, 83–99 (1997)
20. Zhang, X., Shu, C.-W.: Positivity-preserving high order finite difference WENO schemes for compressible Euler equations. J. Comput. Phys. **231**, 2245–2258 (2012)
21. Gerolymos, G., Sénéchal, D., Vallet, I.: Very-high-order WENO schemes. J. Comput. Phys. **228**, 8481–8524 (2009)
22. Zhu, J., Shu, C.-W.: A new type of multi-resolution WENO schemes with increasingly higher order of accuracy. J. Comput. Phys. **375**, 659–683 (2018)
23. Levy, D., Puppo, G., Russo, G.: Central WENO schemes for hyperbolic systems of conservation laws. ESAIM Mathematical Modelling and Numerical Analysis-Modélisation Mathématique et Analyse Numérique **33**, 547–571 (1999)
24. Levy, D., Puppo, G., Russo, G.: Compact central WENO schemes for multidimensional conservation laws. SIAM J. Sci. Comput. **22**, 656–672 (2000)
25. Fu, L., Hu, X.Y., Adams, N.A.: Targeted ENO schemes with tailored resolution property for hyperbolic conservation laws. J. Comput. Phys. **349**, 97–121 (2017)
26. Fu, L., Hu, X.Y., Adams, N.A.: A new class of adaptive high-order targeted ENO schemes for hyperbolic conservation laws. J. Comput. Phys. **374**, 724–751 (2018)
27. Fu, L., Hu, X.Y., Adams, N.A.: A targeted ENO scheme as implicit model for turbulent and genuine subgrid scales. Commun. Comput. Phys. **26**, 311–345 (2019)
28. Fu, L., Hu, X.Y., Adams, N.A.: Improved five- and six-point targeted essentially nonoscillatory schemes with adaptive dissipation. AIAA J. **57**, 1143–1158 (2019)
29. Fu, L.: A very-high-order TENO scheme for all-speed gas dynamics and turbulence. Comput. Phys. Commun. **244**, 117–131 (2019)
30. Fu, L.: A hybrid method with TENO based discontinuity indicator for hyperbolic conservation laws. Commun. Comput. Phys. **26**, 973–1007 (2019)
31. Li, Y., Fu, L., Adams, N.A.: A low-dissipation shock-capturing framework with flexible nonlinear dissipation control. J. Comput. Phys. **428**, 109960 (2021)
32. Takagi, S., Fu, L., Wakimura, H., Xiao, F.: A novel high-order low-dissipation TENO-THINC scheme for hyperbolic conservation laws. J. Comput. Phys. **452**, 110899 (2022)
33. Liang, T., Xiao, F., Shyy, W., Fu, L.: A fifth-order low-dissipation discontinuity-resolving TENO scheme for compressible flow simulation. J. Comput. Phys. **467**, 111465 (2022)
34. Ji, Z., Liang, T., Fu, L.: A class of new high-order finite-volume TENO schemes for hyperbolic conservation laws with unstructured meshes. J. Sci. Comput. **92**, 61 (2022)
35. Fu, L., Liang, T.: A new adaptation strategy for multi-resolution method. J. Sci. Comput. **93**, 43 (2022)
36. Castro, M., Costa, B., Don, W.S.: High order weighted essentially non-oscillatory WENO-Z schemes for hyperbolic conservation laws. J. Comput. Phys. **230**, 1766–1792 (2011)
37. Wu, C., Wu, L., Zhang, S.: A smoothness indicator constant for sine functions. J. Comput. Phys. **419**, 109661 (2020)
38. He, Z., Zhang, Y., Gao, F., Li, X., Tian, B.: An improved accurate monotonicity-preserving scheme for the Euler equations. Comput. Fluids **140**, 1–10 (2016)
39. Fang, J., Li, Z., Lu, L.: An optimized low-dissipation monotonicity-preserving scheme for numerical simulations of high-speed turbulent flows. J. Sci. Comput. **56**, 67–95 (2013)
40. Balsara, D.S., Shu, C.-W.: Monotonicity preserving weighted essentially non-oscillatory schemes with increasingly high order of accuracy. J. Comput. Phys. **160**, 405–452 (2000)
41. Xiao, F., Ii, S., Chen, C.: Revisit to the THINC scheme: a simple algebraic VOF algorithm. J. Comput. Phys. **230**, 7086–7092 (2011)
42. Roe, P.L.: Approximate Riemann solvers, parameter vectors, and difference schemes. J. Comput. Phys. **43**, 357–372 (1981)
43. Rusanov, V.V.: Calculation of interaction of non-steady shock waves with obstacles. USSR J. Comput. Math. Phys. 267–279 (1961)
44. Gottlieb, S., Shu, C.-W., Tadmor, E.: Strong stability-preserving high-order time discretization methods. SIAM Rev. **43**, 89–112 (2001)
45. Hu, X.Y., Wang, Q., Adams, N.A.: An adaptive central-upwind weighted essentially non-oscillatory scheme. J. Comput. Phys. **229**, 8952–8965 (2010)
46. Yamaleev, N.K., Carpenter, M.H.: A systematic methodology for constructing high-order energy stable WENO schemes. J. Comput. Phys. **228**, 4248–4272 (2009)
47. Zhu, J., Zhong, X., Shu, C.-W., Qiu, J.: Runge–Kutta discontinuous Galerkin method using a new type of WENO limiters on unstructured meshes. J. Comput. Phys. **248**, 200–220 (2013)
48. Lax, P.D.: Weak solutions of nonlinear hyperbolic equations and their numerical computation. Commun. Pure Appl. Math. **7**, 159–193 (1954)

49. Sod, G.A.: A survey of several finite difference methods for systems of nonlinear hyperbolic conservation laws. J. Comput. Phys. **27**, 1–31 (1978)
50. Shu, C.W., Osher, S.: Efficient implementation of essentially non-oscillatory shock-capturing schemes, II. J. Comput. Phys. **83**, 32–78 (1989)
51. Woodward, P.: The numerical simulation of two-dimensional fluid flow with strong shocks. J. Comput. Phys. **54**, 115–173 (1984)
52. Xu, Z., Shu, C.W.: Anti-diffusive flux corrections for high order finite difference WENO schemes. J. Comput. Phys. **205**, 458–485 (2005)
53. Kurganov, A., Tadmor, E.: Solution of two-dimensional Riemann problems for gas dynamics without Riemann problem solvers. Numer. Methods Partial Differ. Equ. **18**, 584–608 (2002)
54. Zeng, X., Scovazzi, G.: A frame-invariant vector limiter for flux corrected nodal remap in arbitrary Lagrangian–Eulerian flow computations. J. Comput. Phys. **270**, 753–783 (2014)
55. Zhang, S., Shu, C.-W.: A new smoothness indicator for the WENO schemes and its effect on the convergence to steady state solutions. J. Sci. Comput. **31**, 273–305 (2007)
56. Saad, M.A.: Compressible Fluid Flow. Englewood Cliffs (1985)

A.3 Paper III

Yue Li, Lin Fu, Nikolaus A. Adams

A six-point shock-capturing scheme with neural network

In *Proceedings of International Conference of Numerical Analysis and Applied Mathematics ICNAAM 2021.*

Contribution: My contribution to this work was the development of the method and the corresponding computer code for its implementation. I performed simulations and analyzed the results, and wrote the manuscript for the publication.

A six-point shock-capturing scheme with neural network

Yue Li[1,a)], Lin Fu[2,3,4,b)] and Nikolaus A. Adams[1,c)]

[1]*Chair of Aerodynamics and Fluid Mechanics, Department of Mechanical Engineering, Technical University of Munich, 85748 Garching, Germany.*
[2]*Department of Mechanical and Aerospace Engineering, The Hong Kong University of Science and Technology, Clear Water Bay, Kowloon, Hong Kong.*
[3]*Department of Mathematics, The Hong Kong University of Science and Technology, Clear Water Bay, Kowloon, Hong Kong.*
[4]*Shenzhen Research Institute, The Hong Kong University of Science and Technology, Shenzhen, China.*

[a)]Corresponding author: yue06.li@tum.de
[b)]linfu@ust.hk
[c)]nikolaus.adams@tum.de

Abstract. A recent study of low-dissipation shock-capturing scheme [Fu et al., Journal of Computational Physics 305 (2016): 333-359] proposed a nonlinear sharp selection function to remove the contributions of candidate stencils containing discontinuities from the final reconstruction. In this paper, we train a neural network to replace this empirical level nonlinear selection function in the six-order TENO6-opt scheme. The performance and robustness of the neuron-based six-point scheme are demonstrated with the advection function and 1D Euler equations.

INTRODUCTION

High-order and high-resolution shock-capturing schemes are essential numerical methods to solve compressible fluid problems, which may involve discontinuities and broadband flow scales. Lack of solution regularity invokes the Gibbs phenomenon and may lead to nonlinear instability. Among the concepts proposed to deal with this issue, targeted ENO (TENO) schemes [1] deploy a candidate stencil with its optimal linear weight or discard it completely when crossed by a discontinuity. However, the selection strategy of candidate stencils in TENO schemes as well as the original ENO schemes relies on human intuition in the calculation of smoothness indicators and weighting functions.

The relationship between flow features and the selection of candidate stencils can be interpreted as an input-output function with neuron networks. We train a simple neuron network to explore this non-linear function and to replace the selection procedure in the six-point TENO6-opt scheme. The newly achieved scheme is tested and encouraging results from different governing equations have been obtained. This paper presents results for the achieved neuron-based six-point shock-capturing ENO (NENO6) scheme. We discuss the performance of the NENO6 scheme and check the robustness when it is applied to 1D advection function and 1D Euler equations.

NUMERICAL METHODOLOGY

Key concept of TENO6-opt scheme

The core idea of the TENO scheme is the binary selection of the candidate stencils based on the smoothness indicators with sufficient scale separation. The smoothness indicator for a six-point TENO6-opt scheme is

$$\gamma_k = \left(C + \frac{\tau_6}{\beta_{k,r} + \varepsilon}\right)^q, k = 0, \cdots, 3, \tag{1}$$

$$\tau_6 = \left| \beta_6 - \frac{1}{6}(\beta_{1,3} + \beta_{2,3} + 4\beta_{0,3}) \right| = O(\Delta x^6), \tag{2}$$

where $C = 1$, $\varepsilon = 10^{-40}$, $q = 6$ are adopted for strong scale separation and $\beta_{k,r}$ can be defined as [2]. And subsequently the binary selection is achieved by

$$\delta_k = \begin{cases} 0, & \text{if } \chi_k < C_T, \\ 1, & \text{otherwise}, \end{cases} \tag{3}$$

where χ_k is the normalized measured smoothness indicator

$$\chi_k = \frac{\gamma_k}{\sum_{k=0}^{K-3} \gamma_k}, \tag{4}$$

and the parameter $C_T = 10^{-6}$ in this work can be determined. Such a procedure can be interpreted as a nonlinear input-output mapping between the local flow field features and the binary selection of candidate stencils. By training an artificial neural network (ANN) with a properly constructed database, ANN can act as a black-box to mimic the TENO6-opt selection procedure.

The architecture and training Of the Neural Network

We train a deep neural network known as multilayer perceptron (MLP) to approximate a classifier of the form

$$F = \mathbb{R}^6 \to \mathbb{R}^4. \tag{5}$$

The element of input vector for the neural network is the normalized cell value given by

$$\bar{f}_k = \frac{f_k}{\max(|f_{i-2}|, |f_{i-1}|, |f_i|, |f_{i+1}|, |f_{i+2}|, |f_{i+3}|, 1)}, \ k = i-2, i-1, \cdots, i+3, \tag{6}$$

and the output indicates the probability vector which suggests the selection of each candidate stencil for the final reconstruction. The MLP neural network has four hidden layers, whose widths are 64, 32, 16 and 8 from the input layer to the output layer, respectively. Each hidden layer performs an affine transformation with the output from the previous layer and is activated component-wise by the rectified linear unit (RELU) activation function to form the input for the succeeding layer. For the training of a MLP with the ENO-like stencil selection property, 709000 input samples X^0 including smooth profiles, high-wavenumber profiles, and genuine discontinuities and their corresponding label $\hat{Y}$ (referred to as the ground truth) are generated. The labelled ground-truth datasets are generated from both the analytic and non-analytic functions with different mesh resolutions. The labels of analytic functions are given straightforwardly while the labels of non-analytic functions are analyzed by the optimal TENO6-opt weighting strategy and the ground-truth labeled data is obtained correspondingly.

The cost function deployed to train the model is given by the binary cross entropy function

$$\mathcal{L}_{BCE} = -\frac{1}{m} \sum_m \left[\frac{1}{S} \sum_{k=1}^{S} [\hat{Y}_k^1 \log(Y_k^1) + (1 - \hat{Y}_k^1) \log(1 - Y_k^1)] \right]_m, \tag{7}$$

where S denotes the number of neurons for the output layer, m denotes the size of mini-batch and Y_k^1, $\hat{Y}_k^1$ are the predicted and ground-truth non-smooth stencil probability distribution for a given sample respectively. The training is performed 1000 epochs using Adam [3] training optimizer. Learning rate is initialized as $L_r = 0.0001$, which will reduce successively by a factor of 50% at the epoch $[40, 90, 160, 300, 700]$.

FIGURE 1. reports the convergence history of the loss function $\mathcal{L}_{BCE}$ throughout the optimization procedure with the samples belonging to both the training and validation datasets. It is observed that, with the number of epochs increasing, the loss function $\mathcal{L}_{BCE}$ decreases monotonically until convergence. Good convergence is also obtained for the validation dataset and no overfitting is observed. Based on the binary outputs from the well-trained MLP, the neuron-based reconstruction is formed by the convex combination of the candidate stencils following Eq. (27) and Eq. (28) in [1].
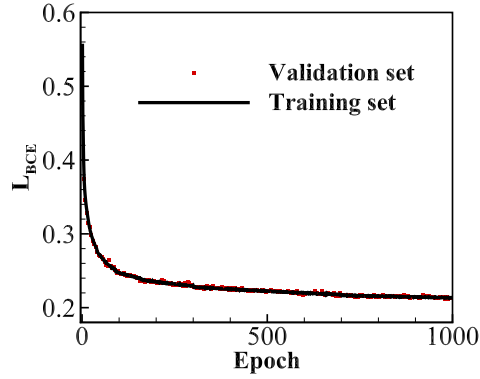
FIGURE 1. Convergence history of the loss function $\mathcal{L}_{BCE}$ for the training and validation datasets.

ANALYSIS OF RESULTS

The NENO6 scheme is deployed to two different types of hyperbolic conservation laws to demonstrate its performance, including the linear advection equation and the 1D Euler equation.

Linear advection

In this section, we first consider the linear advection equation

$$\frac{\partial u}{\partial t} + \frac{\partial u}{\partial x} = 0, \tag{8}$$

with the initial condition of multi-waves [2], which consists of a Gaussian pulse, a square wave, a sharply peaked triangle and a half-ellipse arranged from left to right in the computational domain $x \in [0, 2]$. The computation is performed with TENO6-opt and NENO6 on $N = 150$ uniformly distributed mesh cells and the final simulation time is $t = 6$.
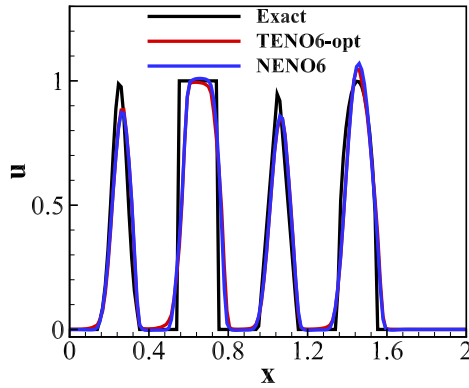

FIGURE 2. Numerical results of advection of multi-wave with TENO6-opt and NENO6 schemes. Discretization is on 150 uniformly-distributed grid points.

As shown in FIGURE 2. that both schemes generate slight overshoots for the advection of the half-ellipse wave. Concerning the advection of the square wave, NENO6 resolves the discontinuities sharper than TENO6-opt.

Lax's problem

In this section, the NENO6 is deployed to 1D Euler equations. The characteristic decomposition method based on the Roe average [4] is employed and the Rusanov scheme [5] is adopted for flux splitting. Afterwards, fluxes are treated as inputs of the MLP and the selections of sub-stencils used to compute interface flux are provided by the output of the MLP. The third-order strong-stability-preserving (SSP) Runge-Kutta method [6] with a typical CFL number of 0.4 is adopted for the time advancement.

The Lax's problem [7] is considered. The computation is performed with TENO6-opt and NENO6 on $N = 150$ uniformly distributed mesh cells and the final simulation time is $t = 0.14$. FIGURE 3. shows that both the contact and the shock waves are well captured with the NENO6 scheme, which demonstrates the generality of the NENO6 scheme when it is applied to other governing equations without any parameter tuning.
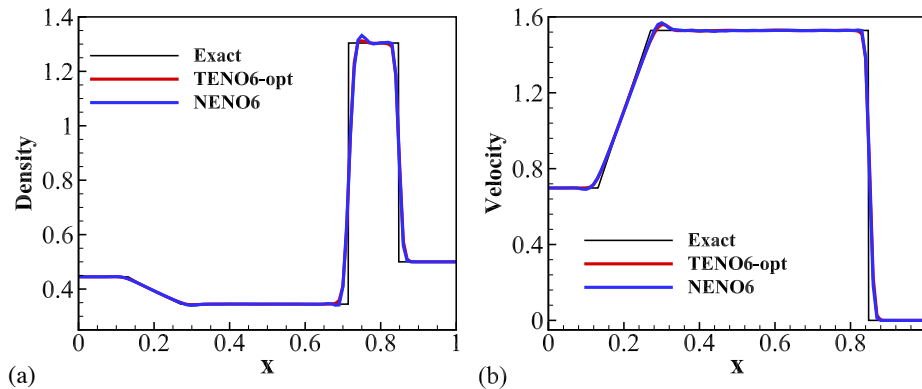

FIGURE 3. Numerical results of the Lax's problem with TENO6-opt and NENO6 schemes: (a) density profile, (b) velocity profile. Discretization is on 150 uniformly-distributed grid points.

CONCLUSION

In this paper, a six-point data-driven high-order shock-capturing NENO6 scheme is proposed and its good capability in terms of sharp capturing of discontinuities, low numerical dissipation, and improved model generality are demonstrated. This work reveals that a classical stencil selection procedure can be replaced by a properly trained neural network, which suggests the potential of exploiting neural network to design more advanced high-order numerical method for hyperbolic conservation laws.

ACKNOWLEDGMENTS

REFERENCES

[1]   L. Fu, X. Y. Hu, and N. A. Adams, Journal of Computational Physics **305**, 333–359 (2016).
[2]   G. S. Jiang and C.-W. Shu, Journal of Computational Physics **126**, 202–228 (1996).
[3]   D. P. Kingma and J. Ba, arXiv preprint arXiv:1412.6980 (2014).
[4]   P. L. Roe, Journal of Computational Physics **43**, 357–372 (1981).
[5]   V. V. Rusanov, USSR J. Comp. Math. Phys. 267 – 279 (1961).
[6]   S. Gottlieb, C.-W. Shu, and E. Tadmor, SIAM review **43**, 89–112 (2001).
[7]   P. D. Lax, Communications on Pure and Applied Mathematics **7**, 159–193 (1954).